Internal Dynamics of Galaxy Clusters in the Red-Sequence Cluster Survey

by

Kris Blindert

A thesis submitted in conformity with the requirements
for the degree of Doctor of Philosophy
Graduate Department of Astronomy and Astrophysics
University of Toronto

Abstract

Internal Dynamics of Galaxy Clusters in the Red-Sequence Cluster Survey

Kris Blindert
Doctor of Philosophy
Graduate Department of Astronomy and Astrophysics
University of Toronto
2006

We present a spectroscopic survey of clusters of galaxies, designed to explore the distribution of matter, and its relation to light, in these massive systems. Our sample is drawn from the Red-sequence Cluster Survey (RCS), and is composed of 33 clusters with a wide range of optical richness and a moderate range of redshift. We obtained spectra of 56 to 529 objects per cluster, which yielded over 3500 redshifts of which 1014 are cluster members. To account for survey incompleteness due to sparse sampling, we constructed several empirical corrections so that our redshift catalogue is suitable for use in dynamical analysis.

We compute the global dynamical properties of the clusters in our survey, such as velocity dispersion and mass, and use them to explore the properties of RCS clusters as functions of total cluster mass. In particular, we first examine the optical richness as an inexpensive proxy for mass. The calibration of this relation is an important ingredient in the construction of the cluster mass function, which is used to constrain cosmological parameters. Our relation and scatter are consistent with self-calibrated cosmological parameter results. We also study the cluster mass-to-light ratios, and how they scale with mass. We compare our results to other observations and to structure formation models. Although the scatter in this relation is large, we find agreement among remarkably different types of galaxy clusters and groups; however, current structure formation models do not accurately reproduce the variation of M/L with mass.

To boost statistics and allow us to perform a more detailed dynamical analysis of clusters, we stack our data into "ensemble" clusters. Cosmological simulations predict a roughly universal density profile for dark matter haloes over many scales, and a relation between halo

mass and the concentration of the profile. We analyse the ensembles using the Jeans equations, and recover density profiles for several ensemble clusters of different masses. Although the sampling of our data at small radii is insufficient to constrain some quantities of interest such as the inner core slope of the density profile, we can constrain the concentrations and orbital anisotropies for the ensemble clusters. We find they agree with predictions and previous observations: namely, that galaxies in clusters follow roughly isotropic orbits, and the concentrations of cluster density profiles are consistent with the prediction one would obtain from their masses. We also estimate the variation of concentration with redshift, finding a slightly stronger evolution than expected.

Acknowledgements

First I must thank my own personal astronomy guru, my supervisor Howard Yee, for imparting his knowledge and experience of galaxy clusters, astronomy, and science in general, and for generously providing so much of his time to his students.

I thank Bob Abraham and Ray Carlberg for their support throughout the Ph. D. program. Thanks also to Matt Bershady, Dick Bond, and Yanqin Wu, for their insightful questions and comments. I am very grateful to my collaborators Erica Ellingson, Mike Gladders, David Gilbank, Roeland van der Marel, and Adam Muzzin. This thesis is due in no small part to their help and support.

I have benefitted greatly from my contact with many graduate students at the department, especially Hy Trac, Mark Brodwin, Allen Attard, Preethi Nair, Carrie Bridge, Brian Lee, Kevin Blagrave, Lawrence Mudryk, and Silvia Bonoli. I thank them for many useful discussions, occasional sparring matches, and many enjoyable decompression sessions.

Finally I want to express my appreciation to some of the non-astronomers in my life. First among these is Ed Tracy: brunch buddy, lover of dogs, player of cards, and the best room-mate ever. I'm also happy to thank Ariel Goldblatt; one of my best friends for over a decade, she has seen me from clueless first-year student to clueless Ph. D. student and will hopefully see me through many more clueless years to come. Lastly I owe a debt of gratitude to my family, for their unwavering love and support. Ich hätte es ohne euch nicht geschafft!

This work was funded by the Natural Sciences and Engineering Research Council of Canada, the Government of Ontario, the Walter C. Sumner Foundation, and the University of Toronto.

Contents

List of Tables

List of Figures

Chapter 1

Introduction

One of the most fundamental physical quantities one might wish to know about an object is its mass. In astronomy this is never a trivial measurement: one cannot simply weigh a star. This difficulty is compounded in the case of large structures, such as galaxies and clusters of galaxies, by the presence of dark matter. The existence of dark matter was suggested as early as the 1930s. Fritz Zwicky (1933; 1937) measured the dispersion of the line-of-sight velocities of "nebulae" in the Coma cluster; applying the virial theorem he estimated the cluster mass-to-light ratio at ~ 500 times solar, more than two orders of magnitude greater than the value for nearby stars. A similar result was found for the Virgo cluster by Smith (1936)[1]. At the time, these results were surprising, but the results of Zwicky and Smith have been essentially confirmed. Nowadays there are many lines of evidence for the existence of dark matter: the high masses of clusters of galaxies, as measured using galaxy velocities, X-ray temperatures, or gravitational lensing effects; the flat rotation curves of galaxies; fluctuations of the cosmic background radiation. The evidence is overwhelming, and dark matter is now accepted as the dominant component of mass in the universe.

1.1 The Mass-to-Light Ratios of Galaxy Clusters

The presence of dark matter naturally impacts the use of galaxy clusters as probes of cosmology. A classical method for estimating the mass density of the universe is done via Oort's method: the mass-to-light ratio (M/L) of clusters is multiplied by the luminosity density of field galaxies to obtain the mass density Ω_M. This procedure results in values of $\Omega_M \simeq 0.2$ (Carlberg et al. 1996, and references therein), roughly in agreement with latter-day measurements from the cosmic background radiation fluctuations (e.g., Bennett et al. 2003). However,

[1] In fact the landmark paper of Hubble & Humason (1931), on the velocity–distance relation of "nebulae", also gave rough estimates of velocity dispersion for the Virgo, Pegasus, and Pisces clusters based on a few velocity measurements each. The dispersions were high (500–1200km/s), in the same range as the more secure estimates of Zwicky (1933, 1937) and Smith (1936) a few years later.

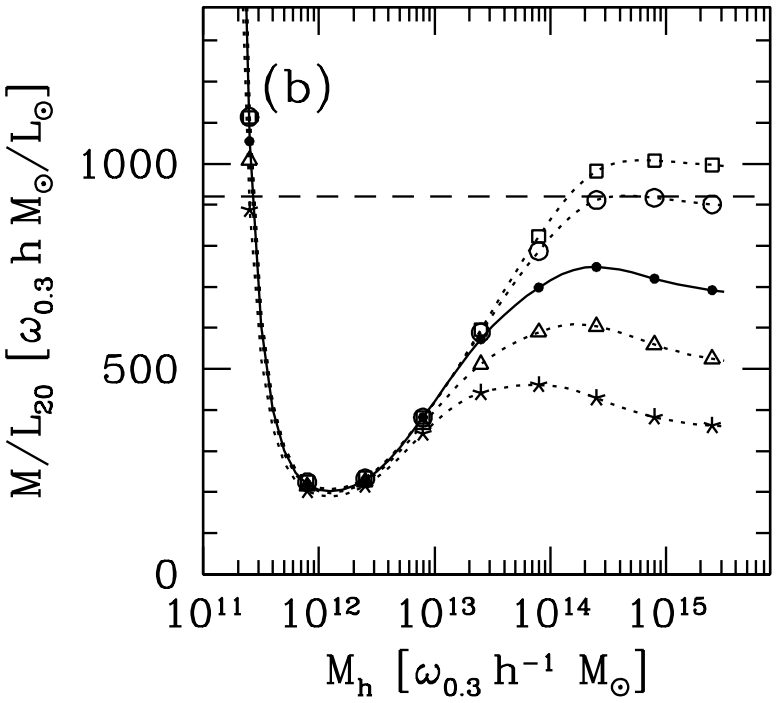

Figure 1.1 M/L ratio versus halo mass, from the HOD models (Tinker et al. 2005). Luminosities are calculated in the Sloan r–band, above a limiting absolute magnitude of $M_r = -20$. Different curves correspond to different values of σ_8: from top to bottom curve, σ_8 decreases from 0.95 to 0.6.

this method relies on the critical assumption that the M/L ratios of clusters are representative of a universal value. Hydrodynamical cosmological simulations by Bahcall et al. (2000) actually predict an "antibias": high density regions of the universe such as clusters of galaxies have higher than average ratios of mass to light. Bahcall et al. (2000) suggested that this antibias is due to the passive stellar populations prevalent in clusters; they estimated cluster luminosities in a blue filter, which tracks recent star formation. At very high masses, comparable to rich clusters and superclusters, they find a plateau in M/L — in other words, they predict a saturation of M/L at high M.

More recently, the formalism of halo occupation distribution (HOD) has been used to characterize how dark matter haloes (such as the massive haloes hosting galaxy clusters) are populated with galaxies. The HOD describes bias by specifying $P(N|M)$, the probability that a halo of virial mass M contains N galaxies of a certain class, where the "class" could for instance be given by a threshold in galaxy luminosity. Thus, the HOD provides a description of how haloes are populated with galaxies. Tinker et al. (2005, hereafter T05) have combined HOD formalism with the correlation functions of galaxies in the Sloan Digital Sky Survey (SDSS). In contrast with the simulations of Bahcall et al. (2000), T05 predicted M/L in the Sloan r–

band, which tracks overall stellar mass rather than star formation. T05 also found a rising mass-to-light ratio as a function of halo mass, although they found that the plateau value of M/L depends strongly on the normalization of the power spectrum σ_8. This dependence is illustrated in Figure 1.1 (reproduced from Figure 6b of T05): increasing the amplitude of the power spectrum fluctuations increases the M/L at large masses.

The variation of M/L with mass reflects the efficiency with which gas can be cooled to form stars in haloes of different masses (with blue light tracing recent star formation and red or near-infrared light better reflecting the integrated star formation history). Star formation is suppressed in massive haloes because of long cooling times, while in small haloes the gas is reheated by feedback processes. Semi-analytical models of star formation generally predict a scale of $\sim 10^{12} M_{\odot}$ at which star formation is most efficient (e.g., White & Frenk 1991). This prediction is also illustrated for the T05 models in Figure 1.1.

There has been a flurry of observational work in this field of late, thanks primarily to the large samples of groups and clusters now available. Measurements of M/L for the 14 X-ray selected clusters of galaxies in the Canadian Network for Observational Cosmology cluster survey (CNOC1 Carlberg et al. 1996) and subsequent measurements for about 200 groups of galaxies in the CNOC2 field survey (Carlberg et al. 2001; Parker et al. 2005) have been followed by measurements using very large samples: $\sim$ 29000 groups in the Two-Degree Field (2dF) Galaxy Redshift Survey (Eke et al. 2005) and $\sim$ 11000 groups and clusters in the SDSS (Díaz & Muriel 2005). Recent results also include near-infrared mass-to-light ratios of the 2dF groups (Eke et al. 2005) and of 9 Abell clusters (Rines et al. 2004). A consensus seems to be forming among the results, at least qualitatively — observations of groups and clusters confirm the simulation/model prediction of a rising mass-to-light ratio with halo mass. However, the details are as yet unclear, partly because the uncertainties and intrinsic scatter in mass and luminosity calculations are large. Also, the predicted plateau at high mass has not been unambiguously seen (although the CNOC1 clusters show no obvious trend with mass, they occupy only a small mass range). Finally, the observed slope of the M/L versus M relation is on average steeper than predicted (see Figure 3.10 of this work). In short, although there is broad agreement between observations, current theoretical work does not accurately predict the observed trend of M/L versus mass.

1.2 The Mass Distribution in Clusters of Galaxies

The internal structures of clusters of galaxies are also useful probes of our understanding of structure formation. In the current paradigm, small matter fluctuations in the early universe grow and merge over time due to gravitational interactions to form the massive dark matter haloes which house clusters. This process of hierarchical formation is the most obvious feature

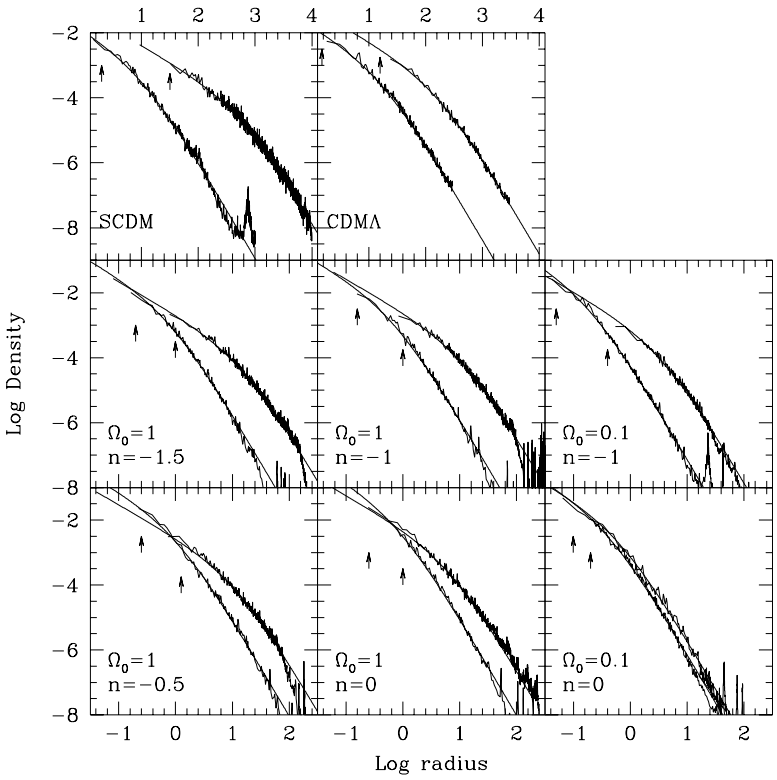

Figure 1.2 Density profiles of simulated dark matter haloes (Navarro et al. 1997). Panels corresponds to simulations for different cosmologies. Each panel shows the least and most massive haloes in each simulation (least massive to the left). Solid lines represent the fits of the simulated density profiles to a universal functional form (see text for details).

of cosmological simulations of cold dark matter, and appears to lead naturally to a particular form for the internal structure of all haloes. This universality of structure was found by Navarro et al. (1996, 1997, hereafter NFW) to hold for dark matter haloes from a wide range of simulated cosmologies over several decades in both halo mass and radius. They proposed a fitting function of the following form:

$$\rho(r) = \frac{\rho_0}{\left(\frac{r}{a}\right)\left(1+\frac{r}{a}\right)^2}\,, \tag{1.1}$$

where ρ_0 is the normalization and a is the scale radius. Figure 1.2 shows the density profiles of simulated dark matter haloes along with fits of the form given in Equation 1.1. A convenient parameter to describe this function is the concentration $c \equiv r_{200}/a$, where r_{200} is the virial radius, within which the mean density is 200 times the critical density (n.b., r_{200} is directly related to the mass of the halo[2]. NFW showed that the fit parameters ρ_0 and a are both functions of the concentration parameter c, which decreases as a function of increasing mass — i.e., dark

[2]The relation is simply $M_{200} = 200\rho_{crit}(4\pi/3){r_{200}}^3$

matter haloes have a universal profile in which halo mass is the only parameter required to describe the distribution of mass with the halo. Lu et al. (2006) attempted to explain the shape of the NFW density profile, using simple one-dimensional simulations. They found that the inner profile $\rho \propto r^{-1}$ arises naturally from the rapid accretion characteristic of the early phases of structure growth, and the outer $\rho \propto r^{-3}$ is a result of slow-accretion at later times. Simulations with high resolution show some scatter in the inner slope of the density profile; for instance Diemand et al. (2005) find a logarithmic slope of 1.16 ± 0.14, a little steeper than the NFW prediction. Simulations by Bullock et al. (2001, hereafter B01) confirmed the NFW prediction for the relation between M and c. However, they also found a dependence on redshift: at a given mass scale, the concentration declines with redshift, by the relation $c \propto 1/(1+z)$.

Testing these predictions for the distribution of mass in a real cluster of galaxies is not trivial, due to the dominance of dark matter. There are three main approaches to estimating the mass and its distribution: using the gravitational lensing of background objects, using the temperature profile of the X-ray emitting intracluster gas, and using the member galaxies as tracers of the potential. Gravitational lensing is the most direct probe of the dark matter, with strong lensing probing the cluster cores and weak lensing the outer region. Note that gravitational lensing measures projected mass in a column, which can include material not bound to the cluster. X-ray observations are restricted to small radii, because the X-ray brightness is proportional to the square of the density of the intracluster gas and the density declines rapidly with radius. X-ray observations also require an assumption of dynamical equilibrium to recover mass from temperature. The use of cluster galaxies as dynamical tracers has the longest history of these techniques. Usually, galaxies are assumed to be in equilibrium so that the Jeans equation can be applied. Because only the line-of-sight component of the galaxy velocities are known, the mass profile is dependent on the shapes of the galaxy orbits (this degeneracy will be explored in more detail in §4.3.5). Recently a new technique has been developed for using member galaxies (Diaferio & Geller 1997; Diaferio 1999), in which the mass is estimated from the trumpet-like shape formed by the cluster in a diagram of velocity versus radius. This caustic method is much less dependent of the galaxy orbital shapes (especially at large radii), and does not require the assumption of equilibrium, making it an extremely useful technique for probing the infall regions of clusters. The three main types of observations one can use to estimate the distribution of mass in a cluster are complementary, each with strengths and difficulties; all methods should be used to properly understand the systematic uncertainties involved. In this thesis we will present the results of a redshift survey of galaxy clusters; therefore we shall restrict the remainder of our discussion to the use of galaxy dynamics.

The Coma cluster is likely the most well-studied cluster in the universe. As described above, its total mass was estimated by Zwicky (1933, 1937); a detailed study of Coma was

made with ~ 200 member galaxies by Kent & Gunn (1982). Merritt & Saha (1993) found a cuspy inner density profile ($\rho \sim r^{-2}$) and steep outer profile ($\rho \sim r^{-4}$). Łokas & Mamon (2003) have found the NFW profile to be consistent with the mass distribution in Coma. Łokas & Mamon (2003) also used the kurtosis profile to constrain the orbits of the early-type galaxies, finding them to be roughly isotropic.

Coma might not be expected *a priori* to be representative of most clusters, as it simply happens to be the most massive cluster nearby and hence is convenient for study. However, dynamical analyses have by now been performed on many clusters with a wide variety of selection techniques, masses, and redshifts, and their profiles and orbital shapes are quite similar to Coma. Studies of the CNOC1 clusters by Carlberg et al. (1997) and van der Marel et al. (2000) show that the profiles of rich X-ray clusters are also consistent with NFW, and that their galaxies are on nearly isotropic orbits. A study of nearby Abell clusters (Katgert et al. 2004) is also consistent with the NFW+isotropic result for Coma, as are the nearby 2dF clusters examined by Biviano & Girardi (2003) using a joint analysis of Jeans and caustic methods and the caustic analysis of rich nearby Abell clusters by Rines et al. (2003).

Studies of galaxy groups are less abundant, and results do not agree as well. Groups are much more difficult to identify than clusters (especially at high redshifts), simply because they do not contrast greatly with the field. Low-redshift groups in the Deep Optical Catalog (Mahdavi et al. 1999) have density profiles consistent with NFW (although an outer slope $\rho \sim r^{-4}$ also fits the data), with some evidence for radial orbits. RASSCALS groups (also at low redshifts) were fit by Mahdavi & Geller (2004) to a density profile with a single power law of $\rho \sim r^{-1.9}$, also with somewhat radial orbits. Finally, Carlberg et al. (2001) constructed the CNOC2 sample of groups at moderate redshifts ($z \simeq 0.1$–0.5); in contrast to other results, they found an increasing velocity dispersion with radius, leading to a cored mass density profile with a shallow slope. A weak lensing re-analysis (Parker et al. 2005) however shows that the rising M/L ratio found by Carlberg et al. (2001) for the CNOC2 groups is not appropriate; in this light it may be desirable to re-evaluate the density profile as well. Upcoming results from the DEEP2 Galaxy Redshift survey (Gerke et al. 2005) should help to clarify the characteristics of moderate and high redshift groups.

Two new studies have attempted to constrain the mass-concentration relation predicted by simulations using a single consistent cluster sample over a range of masses. Łokas et al. (2006) and Rines & Diaferio (2006) have used Abell and SDSS clusters respectively. They find a large scatter in observed cluster concentrations, somewhat larger than the scatter in concentrations of the simulated dark matter haloes by B01. The uncertainty in the relation is large, but their results are consistent with the B01 relation. Note also that both of these studies use low redshift clusters; to date there has been no attempt to constrain the evolution of the concentration parameter.

The use of cluster galaxies as dynamical tracers of the gravitational potential has come a long way since the efforts of Zwicky (1933, 1937). There is a growing wealth of cluster samples with large numbers of member galaxies, appropriate for detailed dynamical analysis using the Jeans equations along with velocity profile shapes or application of the promising new caustic method. Observed clusters seem to have a density profiles consistent with the prediction of simulations, while results for lower mass systems are less clear. Recently first attempts have been made to constrain the relation between the mass of a cluster and the concentration of its density profile; while results are consistent with the B01 prediction from simulations, the scatter is large. Also, studies of both groups and clusters have been performed using low redshift samples, excepting CNOC1 and CNOC2, and the B01 prediction of evolution of the concentration is as yet untested. Clearly, although a general picture is emerging, much work remains to be done to constrain the mass distribution in clusters.

1.3 Using Clusters to Constrain w

One of the most important issues in physics today is the nature of dark energy. With a contribution to the energy density of the universe higher than that of matter (cf., $\Omega_M = 0.27$, $\Omega_\Lambda = 0.73$; Bennett et al. 2003), an understanding of this mysterious energy is crucial to a complete cosmological picture. The equation of state of the dark energy $w = P/\rho$ can be constrained using supernovae as standard candles or using the evolution of the abundance of galaxy clusters, $N(M, z)$. A measurement of the evolution of the cluster mass function essentially estimates the growth of structure over time, which is dependent on several cosmological parameters of importance, e.g., σ_8 and Ω_M, as well as Ω_Λ and w. Many future surveys plan to exploit this dependence, often using observations of the Sunyaev-Zeldovich effect which will require extensive follow-up work to determine the nature of SZ clusters. More timely is the ongoing second-generation Red-sequence Cluster Survey (RCS-2; `http://www.rcs2.org`), for which observations should be complete in the next year. RCS-2 identifies clusters using the signature of early-type galaxies in a colour magnitude diagram; imaging of only two filters is needed to provide estimates of cluster redshift and richness[3]. If one can also determine cluster mass, then the abundance of clusters can be measured as a function of redshift. However, RCS-2 is projected to find $\sim 10^4$ clusters out to redshift one, in order to measure $N(M, z)$ with sufficient accuracy. With a sample this large, it is simply not possible to individually estimate the masses of all clusters: observationally cheap proxies must be translated into masses via a calibration. Optical richness is a natural choice as mass estimate: it is available using the survey data alone, and correlates well with cluster mass (Yee & Ellingson 2003). Gladders

[3]The RCS-2 survey does, however, utilize three filters, in order to straddle the 4000Å break over a wide redshift range.

et al. (2006) have already shown, from ~ 1000 clusters, that cosmological parameters such as σ_8 and Ω_M can be constrained using optical richnesses as proxies for cluster masses. They also pointed out that the main uncertainty in the recovery of cosmological parameters is due to the relation between richness and mass, and that the scatter in the relation need not be small so long as it is well understood. Clearly, this calibration is a vital component of the use of galaxy clusters to understand dark energy.

1.4 Outline of Thesis

Motivated by the issues raised above, we present a dynamical study of galaxy clusters over a moderate range of redshift ($0.2 \lesssim z \lesssim 0.6$) and a wide range in mass, spanning the regime from rich groups to clusters. The primary scientific goals of this survey are:

- to measure the masses and luminosities of clusters over a large dynamic range, and examine the variation of the mass-to-light ratio with mass. Although most results to date are in broad agreement, as discussed in §1.1 current models do not match observations. It is therefore desirable to employ many different types of clusters, selected through complementary means, to strengthen the observational constraints on the M/L dependence on mass.

- to estimate the relation between cluster mass and optical richness. This calibration is necessary for the use of large samples of clusters to measure cosmological parameters such as the dark energy equation of state.

- to determine the mass distribution in clusters of galaxies over a range of masses. Cosmological simulations predict a relation between the mass of a dark matter halo and the concentration of its density profile, and an evolution of this relation over time. Recent analyses of low-redshift clusters are consistent with the predicted *M*-*c* relation. We wish to confirm this result for higher redshift clusters, and to estimate its possible evolution with redshift.

This thesis represents the first extensive survey of spectroscopic observations of galaxy clusters in the Red-sequence Cluster Survey (RCS Gladders & Yee 2005). The sample is composed of 33 clusters, with redshifts of $\sim$10–100 member galaxies per cluster. In chapter 2 we introduce the clusters targeted in our survey, and describe the observations and data reduction. We present redshift catalogues for the clusters, including empirical selection functions to account for incompleteness in the survey sample. Following the presentation of the spectroscopic survey, in chapter 3 we compute the global properties of the clusters: velocity dispersions, virial radii, masses, optical richnesses, and luminosities. We discuss the reliability of the

dynamical properties, addressing issues such as the rejection of field galaxies and the choice of cluster centroid. With global properties in hand, we examine the structure of galaxy clusters in chapter 4, in which we stack our clusters into scaled ensembles to boost statistics. We present an analysis combining the Jeans equation with the shape of the cluster velocity distribution to constrain the galaxy orbits as well as the mass density. The data are also divided into ensembles of different masses and redshifts, to compare observed concentrations of density profiles with predictions from simulations.

1.5 Adopted Cosmological Model

In this work, whenever necessary for our calculations, we adopt the following cosmological parameters based on the WMAP preliminary results (Bennett et al. 2003): a flat universe with matter density $\Omega_M = 0.27$, dark energy density $\Omega_\Lambda = 0.73$. In addition we set the Hubble constant $H_0 = 70\mathrm{km/s/Mpc}$.

Chapter 2

A Spectroscopic Survey of Galaxy Clusters

2.1 Introduction

In this chapter we present a spectroscopic survey of galaxy clusters, drawn from the Red-sequence Cluster Survey (RCS) of Gladders & Yee (2005). We have performed the first large program of spectroscopic observations of RCS clusters, with sufficient statistics to derive global properties of the individual clusters such as velocity dispersion and mass and to estimate the average mass distribution of clusters. We present the targeted clusters in §2.2. They span a moderate range in redshift, representing a compromise between observational efficiency and leverage on possible evolution of cluster properties. They also occupy a large mass range. Although it is relatively easy to observe massive clusters, probing deeper into the cluster mass function allows one to bridge the gap between the extreme environments of the most massive clusters and the much more common galaxy groups, allowing for more stringent tests of models of structure formation.

In §2.3 we describe the observational strategy employed by our survey, including the details of mask design for multi-object spectrograph instruments, and the observations themselves. The data reduction and estimation of the galaxy redshifts is described in §2.4, and the redshift accuracy of the survey is assessed. In §2.5 we present our redshift catalogue. The catalogue includes several important empirical selection functions, due to the sparse sampling strategy of our survey. We also estimate our success at measuring redshifts as a function of magnitude and colour, and estimate the depth of the survey. Finally, in §2.6 we discuss the recovery of our targeted RCS clusters from the redshift survey, including serendipitous clusters found in the fore- and back-grounds of some of our targets, and we estimate the amount of contamination present in the RCS survey due to projection effects.

2.2 The Clusters

2.2.1 The Red-Sequence Cluster Survey

Optical searches for galaxy clusters have traditionally been plagued by high contamination rates. Galaxies which are distant and dynamically unrelated can lie along the same line of sight, appearing clustered on the sky and polluting cluster samples. This contamination can be greatly alleviated if one uses galaxy colours: red galaxies in clusters form a tight relation in a colour-magnitude diagram (see Figure 2.1), whose colour is determined by the redshift of the cluster. If one searches for galaxy overdensities in both angular and colour space, then,

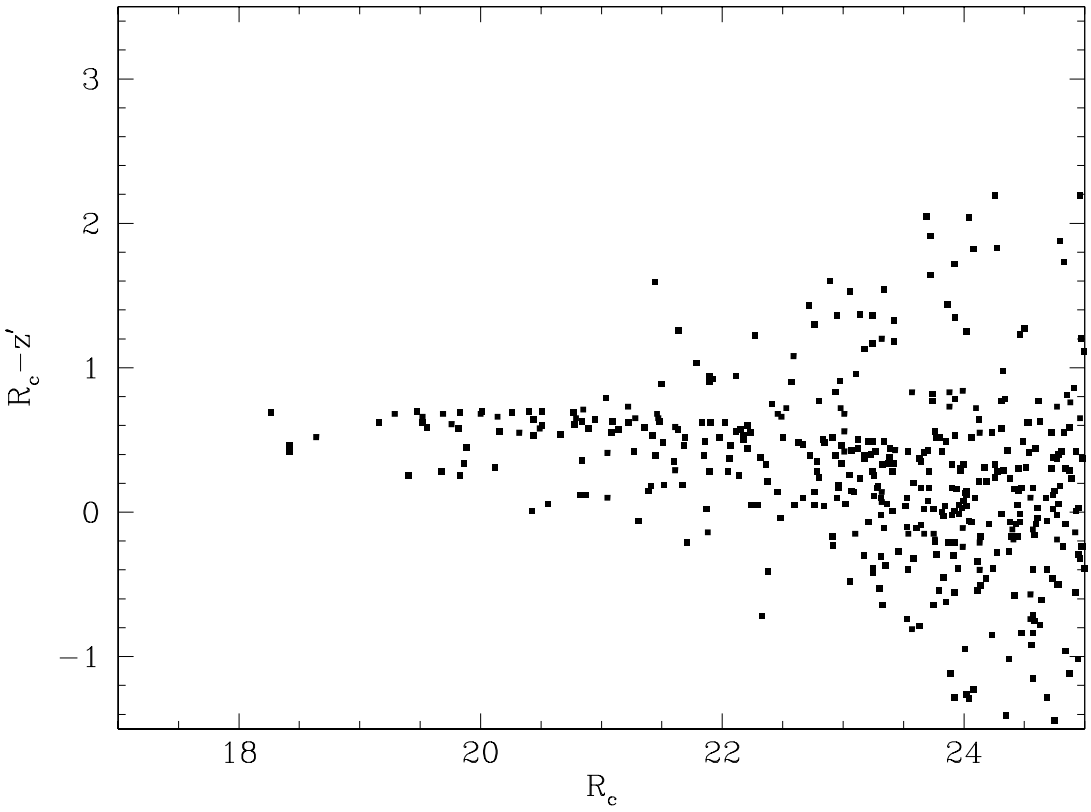

Figure 2.1 Colour-magnitude diagram for a cluster at redshift $z = 0.39$. All galaxies within 2 arcminutes of the cluster centre are plotted. The cluster red-sequence appears as a clear overdensity of bright galaxies with $R_c - z' \sim 0.6$. Data are taken from Gladders & Yee (2005).

one may greatly reduce contamination by foreground and background objects. Also, because the position of the red sequence on the colour-magnitude diagram is determined by redshift, one automatically obtains a photometric redshift estimate for each cluster. This red-sequence technique for cluster finding is described in detail in Gladders & Yee (2000) and in the thesis

of Gladders (2002).

The RCS is a $\sim$ 100 square degree imaging survey in filters R_c and z' (Gladders & Yee 2005, hereafter GY05). It was designed primarily to find galaxy clusters from moderately low redshifts ($z \sim 0.2$) out to high redshifts ($z > 1$). Clusters were identified, and cluster redshifts were estimated, using the technique sketched above. Cluster richnesses were estimated using the B_{gc} parameter (see §2.2.2 below), which can be measured directly from the RCS survey data. Thus, the RCS provides cluster detections as well as redshift and richness estimates.

2.2.2 The B_{gc} Optical Richness Parameter

We will use the B_{gc} parameter (Yee & López-Cruz 1999) to estimate the richness of a galaxy cluster. B_{gc} is the amplitude of the correlation function between galaxies and the cluster centre; essentially it measures the number of galaxies within a small aperture, background-corrected and scaled by the luminosity function (and with dependence on the spatial distribution of galaxies). It has units $(h_{50}\,\mathrm{Mpc})^{-1.77}$. Yee & Ellingson (2003) have shown that B_{gc} correlates well with observationally more expensive cluster properties such as velocity dispersion or X-ray temperature, and thus provides an estimate of cluster mass that can be computed from optical imaging data alone. The B_{gc} parameter was used in the design and observation phases of this work.

Recently, GY05 have introduced B_{gcR}, a new version of the richness parameter which uses only the galaxies within a slice on a colour-magnitude diagram. This parameter exploits the colour signature of early-type cluster galaxies to minimize projection effects, just as it was exploited by the cluster-finding algorithm. It should thus provide more stable estimates of richness than the original B_{gc}. We therefore use B_{gcR} for all analysis of RCS clusters in this work.

2.2.3 Our Cluster Targets

The main goal of this thesis is to examine cluster properties such as mass profile and mass-to-light ratio, and how they relate to total cluster mass. To this end we launched a large program of follow-up spectroscopy on clusters selected from the RCS. We selected clusters using richness as a proxy for cluster mass, aiming to populate three bins of richness: $B_{gc} \leq 500$, $500 < B_{gc} < 800$, and $B_{gc} \geq 800$ (equivalent to Abell richness classes < 0, 0, and ≥ 1; see Yee & López-Cruz 1999 for the relation between B_{gc} and Abell richness class). Also, we restricted our sample selection to clusters with red-sequence photometric redshifts below 0.6 to allow for efficient spectroscopy with available optical multi-object spectrographs.

In order to robustly compute mass profiles from a dataset of radii and velocities, $\sim 10^2$–10^3 galaxies are necessary (Merritt & Saha 1993). This level of detail is only available for the

Table 2.1. Distribution of planned clusters, selected from the RCS survey

	$0.15 \leq z \leq 0.3$	$0.3 < z < 0.45$	$0.45 \leq z << 0.6$
$B_{gc} \leq 500$	8	8	8
$500 < B_{gc} < 800$	4 (+2 CNOC1[a])	4 (+2 CNOC1[a])	6
$B_{gc} \geq 800$	3 (+6 CNOC1[a])	5 (+4 CNOC1[a])	7 (+2 CNOC1[a])

[a]Data are available from Yee et al. (1996a); Ellingson et al. (1997); Yee et al. (1998); Abraham et al. (1998); Ellingson et al. (1998)

richest galaxy clusters, and requires a large commitment of observing resources. It is common to stack clusters into ensemble datasets in order to reach the large numbers required for a detailed dynamical analysis (e.g., Carlberg et al. 1997; Biviano & Girardi 2003; Mahdavi & Geller 2004). We adopted this practice, so that the total number of clusters required would be larger but that $\sim$ 10–100 member galaxies per cluster would be sufficient for our purposes. We determined that roughly 14 poor clusters and 9 rich clusters in each of three redshift bins would yield enough member galaxies (although we note that these bins were used in practice only for sample selection: the creation of ensemble clusters for final analysis is based on the actual numbers of cluster members, described further in chapter 4).

Because of observing time constraints, it was necessary to add clusters from the CNOC1 survey (Yee et al. 1996b). Unlike RCS clusters, the CNOC1 clusters were X-ray selected. Thus the selection criteria for these two samples are quite different: X-ray clusters are discovered by the presence of gas heated by the cluster potential well, while RCS clusters are found by an overdensity of red galaxies. It is likely that the resulting cluster properties will be different, in particular that the RCS clusters may be less relaxed and possibly poorer in gas content. Possible differences in cluster properties of these samples and their impact on our results will be discussed in later chapters. Table 2.1 presents the distribution of target RCS clusters with richness and red-sequence photometric redshift. Also shown are clusters from the CNOC1 survey (Yee et al. 1996b), which are used to increase the number of rich clusters in our sample.

Targets were chosen from preliminary versions of the RCS cluster catalogues. For each observing run, we selected RCS clusters of appropriate Right Ascension and Declination, with richness and redshift chosen to fill out the desired distribution and to observe efficiently (higher redshift clusters were typically observed using the larger telescope, and richer clusters using the instrument with larger field-of-view). Clusters were also visually checked before

addition to the target list, to verify these preliminary candidates, and to avoid clusters near large chip defects in the photometric catalogue or near bright stars. Due to refinements in the cluster-finding algorithm and richness estimation, as well as in photometric calibration (which affects both richness and redshift estimates), the character of our cluster targets has changed since the time our survey was designed. However, although individual cluster characteristics may be substantially different, the overall nature of our sample remains the same.

2.3 Strategy and Observations

2.3.1 Pointings and Mask Design

Our survey was designed to cover clusters out past 2 cluster virial radii r_{vir}, in order to probe into the outskirts of clusters, where galaxies may be falling into the cluster for the first time. Rough estimates of virial radii were obtained by applying the r_{200}–B_{gc} scaling relation for CNOC1 clusters (Yee & Ellingson 2003), and were used to determine how many pointings to use for each cluster.

Multi-object spectroscopy masks were designed using algorithms created for the CNOC2 field galaxy survey (Yee et al. 2000). Each pointing was allotted a bright and faint mask[1], in order to increase the number of cluster members while improving spatial sampling and observational efficiency (since integration times could be adjusted according to the magnitudes of the targeted galaxies). Mask A was designed for bright objects, from the brightest cluster galaxy down to roughly $M^* + 1$. Galaxies were given priority ranking by R_c magnitude and proximity to the cluster centre. Fainter objects were then added to fill all available space in the mask. See Figure 2.2 for an example mask design. The second mask (B) placed high priority on fainter objects, down to $M^* + 2$, which had not been selected in mask A. After these slits were chosen, redundant slits for objects from mask A were added when possible, with higher priority for faint objects which might benefit most from added exposure time. These redundant observations also provide a sample of objects with independent redshifts from different masks, allowing us to estimate our redshift uncertainties. Masks were designed with slit widths of $\sim 1.3''$ (adjusted slightly for seeing). Slit lengths were set to a minimum of $8.5''$, and expanded to fill available space with priority higher for faint objects.

2.3.2 Instruments

Spectroscopic observations were performed using two instruments. In the north, we used the Multi-Object Spectrograph (Le Fevre et al. 1994) operating on the 3.6 metre Canada-France-

[1]Some flanking fields were given only a single mask, when the cluster richness was not high enough to justify two masks of the flanking fields.

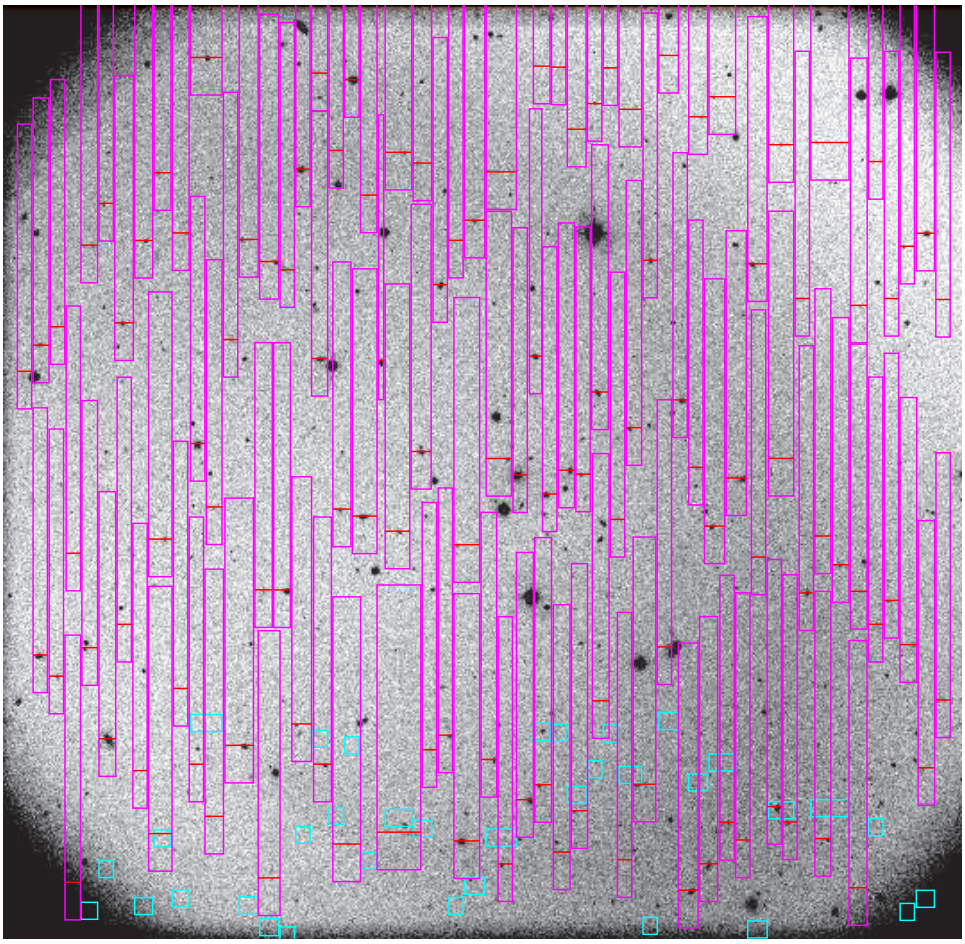

Figure 2.2 Example mask design: the bright mask of 2317-0102, one of the fields observed with CFH-MOS. The slits are shown in red, the expected locations of the spectra on the CCD are magenta boxes, and the cyan boxes show the 0^{th} order contamination. Note that a $\sim$ 2000Åband-limiting filter is available for the CFH-MOS instrument, allowing us to multi-tier the spectra.

Hawaii telescope; hereafter this instrumental set-up is referred to as the CFH-MOS. It provides a 9×8 arcminute field of view for spectroscopy, and we choose a grism with moderate dispersion which yielded spectral resolution of 13.8Å. We also employed a band-limiting filter to allow for multi-tiering of spectra on the detector, which greatly improves spatial sampling as well as the total number of objects that can be observed in one mask. Our redshift range is approximately the same as that of the CNOC2 field galaxy redshift survey (Yee et al. 2000) which was performed on the same instrument; we therefore use the CNOC2 band-limiting filter. See Figure 2 of Yee et al. (2000) for a transmission curve of this filter. This filter shortens spectra to only 2000Å, allowing us to place over 100 slits on each multi-object spectroscopy mask, a

Table 2.2. Summary of observational set-up for the two components of the survey

Telescope	Instrument	Detector	Grism	F.O.V.	Pixel Scale	Å/pix	Resolution	λ-range	Avg.# slits/mask
CFHT	MOS	EEV1	B300	$9' \times 8'$	$0.283''$/pix	3.2	13.8Å	4300–6300Å	119
Magellan	LDSS2	SITe1	Med_Blue Med_Red	$6' \times 4'$	$0.378''$/pix	5.3	15.4Å	4000–8600Å	33

factor ~ 3 improvement over observing without the band-limiting filter.

In the south, we used the Low Dispersion Survey Spectrograph 2 (Allington-Smith et al. 1994) on the 6.5 metre Magellan telescopes (hereafter referred to as Mgl-LDSS2). This instrument has a spectroscopy field of view of 6 arcminutes, and grisms at slightly lower dispersion than CFH-MOS for a spectral resolution of 15.4Å. Two medium-dispersion grisms were available for this instrument, one with more red sensitivity than the other; we used the blue grism for clusters at redshifts $z < 0.4$, and switched to this redder grism for higher redshift clusters. Unfortunately no band-limiting filter was available for Mgl-LDSS2, so we were limited to an average of 33 slits per mask. Details of our observational set-up are summarized in Table 2.2.

2.3.3 Observations

The observations were carried out over several runs. Two CFH-MOS runs were devoted to this program. Mgl-LDSS2 data were acquired during observing runs earmarked for high redshift targets: our relatively low redshift clusters were observed during lower quality observing conditions (e.g., during grey time or poor seeing). In addition one Mgl-LDSS2 run was devoted entirely to our cluster targets. A journal of observations is provided in Table 2.3.

In all, we obtained spectra for 36 cluster targets, having lost several nights due to weather and instrument problems. We present a log of the observations for these targets in Table 2.4. This dataset is substantially smaller than the 53 targets originally planned. Our dynamical analysis will however proceed, albeit with a more modest number of redshift and richness bins.

Table 2.3. Journal of observations

Run Date	# Nights	# Masks	Comments
Northern sample (CFH-MOS)			
October 2002	4	23	$\sim$ 1.5 nights lost due to technical problems and bad weather
May 2003	4	30	several hours lost due to bad weather
Southern sample (Mgl-LDSS2)			
October 2001	3	8	$\sim$ 1 night lost due to technical problems and bad weather; partial nights
December 2001	2	4	partial nights
January 2002	3	1	partial nights
February 2002	2	8	$\sim$ 0.5 night lost due to technical problems; partial nights
May 2002	2	0	both nights lost due to bad weather
November 2002	4	38	

2.4 Data reduction and Redshift Estimation

2.4.1 Extraction and Calibration of Spectra

Our spectroscopic reduction process is semi-automatic, using standard IRAF reduction procedures, and very closely follows the procedures of CNOC2 (see §4 of Yee et al. 2000). Spectra are automatically cleaned of cosmic-ray detections (see Yee et al. 1996b) and corrected for pincushion distortion using a polynomial fit, and multiple exposures are summed. The mask design files, which list for the positions of all slits and their target objects (along both the sky and dispersion directions), are modified to include any serendipitous object whose light falls through one of our slits, and also to calculate appropriate regions for background sky subtraction (by comparing the positions of the slit and objects). These modified mask design files are used to create an IRAF aperture database of object positions, object widths, and sky background ranges. Objects are extracted automatically using this database, and problem cases (such as serendipitous faint objects which share a slit with a bright object) are re-extracted interactively. The arc exposures are extracted from the same extraction apertures as the objects, and wavelength calibration solutions are found semi-automatically: for one arc spectrum, several prominent lines are identified interactively, the remainder are automatically identified from a line list, and the solution is fit to the data. This solution is then applied to all other objects in the mask, and corrections are made interactively where necessary (for instance, adjustments are often necessary near the edge of a mask).

The spectra are extracted, wavelength-calibrated, and linearized. The Mgl-LDSS2 data are

Table 2.4. Summary of spectroscopic observations

RA (J2000)	Dec (J2000)	z_{phot}	B_{gc}	# pointings	# masks	# slits	Comments
Northern Sample ($9' \times 8'$ pointings, $\sim$ 120 slits per mask)							
02 : 22 : 40.89	+01 : 44 : 42.4	0.20	335	1	2	229	
02 : 23 : 31.20	+01 : 18 : 29.2	0.36	375	1	2	212	
02 : 25 : 16.39	+00 : 11 : 22.1	0.28	453	1	2	246	
03 : 51 : 39.53	−09 : 56 : 31.2	0.24	775	2	3	331	
09 : 28 : 21.20	+36 : 46 : 28.0	0.39	1207	2	4	468	
09 : 30 : 10.85	+38 : 41 : 29.0	0.47	379	1	2	220	
11 : 20 : 37.64	+25 : 22 : 18.1	0.31	443	2	3	334	
11 : 23 : 21.59	+25 : 25 : 58.6	0.32	461	1	2	233	
13 : 25 : 23.65	+29 : 19 : 10.7	0.43	400	1	2	241	
14 : 46 : 31.81	+08 : 59 : 33.6	0.24	343	1	2	224	
14 : 47 : 07.50	+09 : 49 : 16.7	0.23	1581	3	5	529	
14 : 52 : 59.87	+08 : 59 : 22.3	0.47	454	1	2	231	observing conditions v. poor
16 : 15 : 46.76	+30 : 57 : 25.4	0.42	1563	2	4	451	
16 : 20 : 04.24	+30 : 44 : 55.4	0.30	383	1	2	221	
13 : 31 : 59.06	+28 : 45 : 34.5	0.44	313	1	2	224	
21 : 53 : 14.59	−05 : 44 : 19.3	0.35	425	1	2	215	
21 : 57 : 00.57	−04 : 42 : 03.0	0.27	620	2	4	465	
23 : 15 : 44.99	+00 : 53 : 12.9	0.33	1201	1[a]	2	218	
23 : 16 : 53.95	−00 : 11 : 16.0	0.49	755	1[a]	2	222	cluster centre not obtained, offset field only
23 : 17 : 36.36	−01 : 02 : 57.6	0.21	369	1	2	226	
23 : 18 : 30.39	−00 : 24 : 40.9	0.38	638	1	2	211	
Southern Sample ($6' \times 4'$ pointings, $\sim$ 30 slits per mask)							
02 : 24 : 02.66	−02 : 27 : 27.3	0.33	470	1	2	62	
03 : 34 : 13 : 18	−28 : 25 : 20.0	0.60	1148	3	6	190	
03 : 36 : 32.68	−28 : 47 : 29.5	0.47	642	3	6	180	
04 : 36 : 44.00	−28 : 12 : 13.1	0.40	411	1	2	58	
04 : 42 : 07.27	−28 : 12 : 54.6	0.41	1192	3	4	59	
05 : 11 : 20.01	−42 : 41 : 45.6	0.36	653	3	4	128	
05 : 15 : 36.91	−43 : 25 : 39.7	0.36	976	1	2	56	
05 : 19 : 20.50	−42 : 47 : 38.8	0.50	924	3	4	128	
11 : 03 : 41.29	−04 : 57 : 36.0	0.37	690	1	2	67	
11 : 07 : 53.24	−05 : 16 : 37.7	0.52	569	1	2	71	
21 : 15 : 15.60	−63 : 09 : 53.1	0.23	571	1	2	60	
21 : 20 : 06.35	−62 : 05 : 57.7	0.45	866	3	6	192	
21 : 21 : 53.45	−63 : 35 : 29.1	0.40	1622	3	4	178	
23 : 43 : 57.43	−35 : 17 : 28.0	0.49	717	3	6	185	
23 : 47 : 48.18	−35 : 35 : 02.6	0.30	229	3	4	121	

[a] extra pointings aborted for this target, due to bad weather

extracted from 4000 to 8600Å and linearized at 5.2Å/pix, and the CFH-MOS data are extracted from 4300 to 6400Å, linearized at 3.2Å/pix (for spectral resolutions of 15.4 and 13.8Å, respectively). At this point we visually inspect the spectra and interpolate over any defects such as poorly subtracted bright sky lines and 0^{th} order contamination. Two bright sky lines are often interpolated over: OI5577Å and OI6300Å. Also, for the Magellan data, the oxygen absorption feature at 7617Å must be removed.

Sky lines are used to test the quality of the wavelength calibrations; we find their positions to be good to within an RMS of 0.4Å, equivalent to 21km/s. Spectra are also flux calibrated to F_λ using observations of standard stars through one of the masks' central slits. However, we

only have flux calibration at a single location on the chip and there may be small differences in the "true" calibration over the field of view (for instance because focus may be slightly different, and slits will be cut to very slightly different widths). Therefore, as was the case for the CNOC1 and CNOC2 surveys, flux calibrations have roughly 20% accuracy.

2.4.2 Computation of Redshifts

We use the CNOC1 cross-correlation technique to determine redshifts (see Yee et al. 1996b, for details)[2]. Object spectra are cross-calibrated against three templates: the elliptical, Sbc, and Scd galaxy spectra from Kennicutt (1992). We visually inspect the spectrum and cross-correlation functions for each object, in order to accept or reject the redshifts calculated by the cross-correlator. Usually, the chosen redshift corresponds to the template with the highest correlation coefficient R_{cor} (Tonry & Davis 1979), but sometimes a different template is chosen if it visually is deemed to better match the spectral type of that galaxy. Note that this limits the strength of any galaxy populations analysis one can do on this dataset: the spectral types are merely rough estimates of the true spectral types for the galaxies, and a thorough examination of galaxy populations in our cluster sample would require more sophisticated measures such as equivalent widths or principal component analysis (e.g., Ellingson et al. 2001). However, our assigned spectral types should be sufficient at least to separate galaxies into "early" and "late" types. In Figures 2.3 and 2.4 we show example spectra of cluster members of different brightnesses and spectral types.

In addition to the visual confirmation of all redshifts after the initial cross-correlation, we also compare the galaxy redshifts to their colours and perform an additional inspection on redshift-colour outliers. Figure 2.5 compares colours for all galaxies with measured redshifts in our survey against model colours from Bruzual & Charlot (2003): although the scatter is large and our spectral types are crude, our measured colour-redshift relations agree with predictions. We also tested our spectroscopic redshifts against the photometric redshifts available from Hsieh et al. (2005) in 12 of our cluster fields and found good agreement, as shown in Figure 2.6. We find a scatter on this relation of 0.062 (68% confidence limit) for the 1201 objects with measured z_{spec} and z_{phot} (which reduces to 0.056 for the 984 galaxies between $0.2 \leq z_{spec} \leq 0.6$). This is similar to the scatter of 0.06 found by Hsieh et al. from over 4000 objects in their spectroscopic training set.

Due to our mask design procedure, we obtained multiple independent redshifts for 130 galaxies. We used these redundant redshifts to estimate our velocity accuracy. A histogram of the velocity differences is shown in Figure 2.7, and the 68% confidence interval of the differences is 119km/s. Dividing by $\sqrt{2}$ yields an average measurement error of $\pm$84km/s. In

[2]Fortran code for the cross-correlation kindly provided by Erica Ellingson

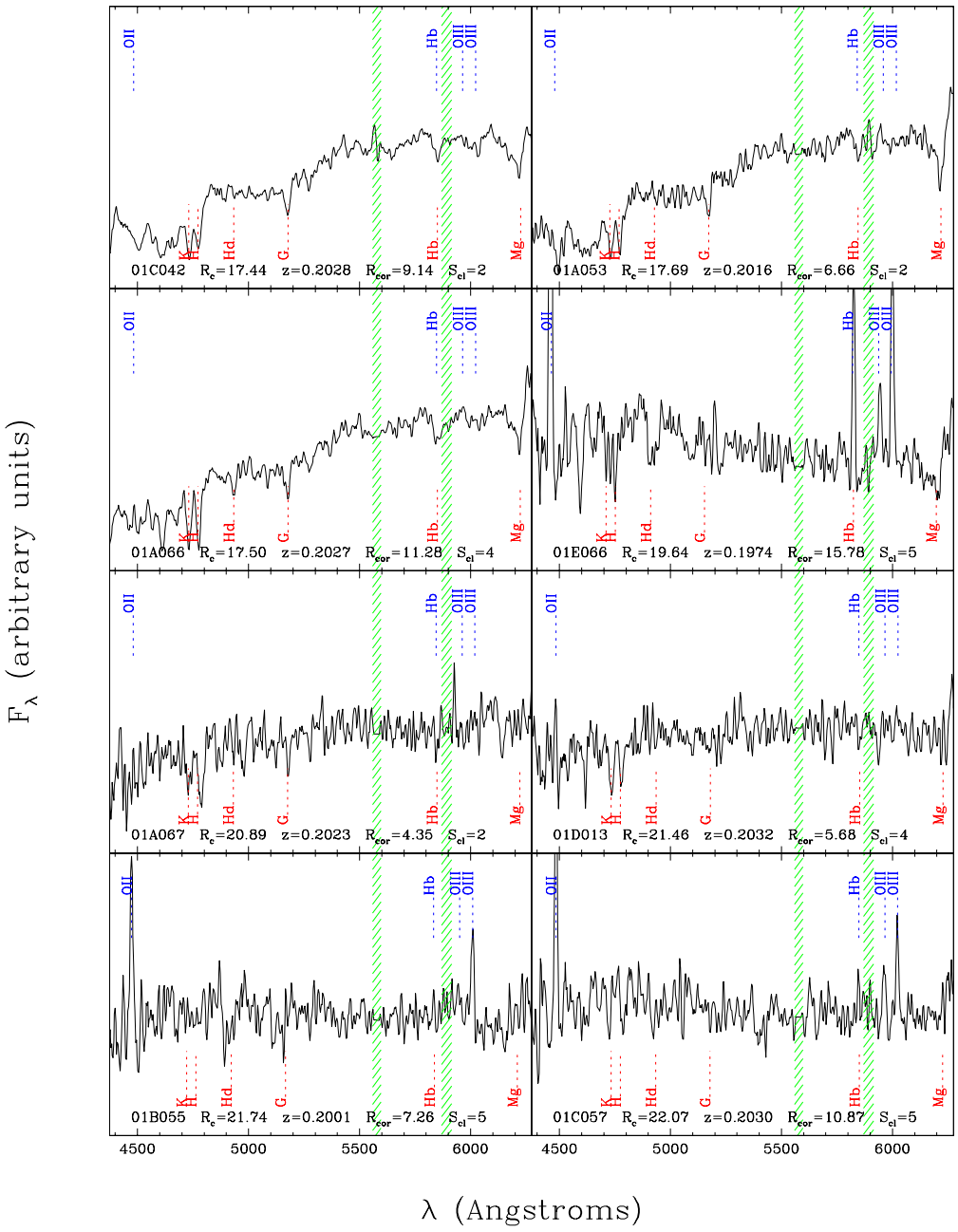

Figure 2.3 Example spectra of cluster members, for cluster RCS J144708+0949.0 at $z_{spec} = 0.20$. This cluster was observed with the CFH-MOS using a band-limiting filter, and is one of our lowest redshift clusters. Each spectrum is labelled with the object's ID, magnitude, and spectral class ($S_{cl} = 1$ or 2 for an elliptical; 3 for E+A, 4 for Sbc, or 5 for Scd or Irr). Bright sky lines were often interpolated over and are shown as hashed regions. Prominent spectral features at this redshift are also marked.

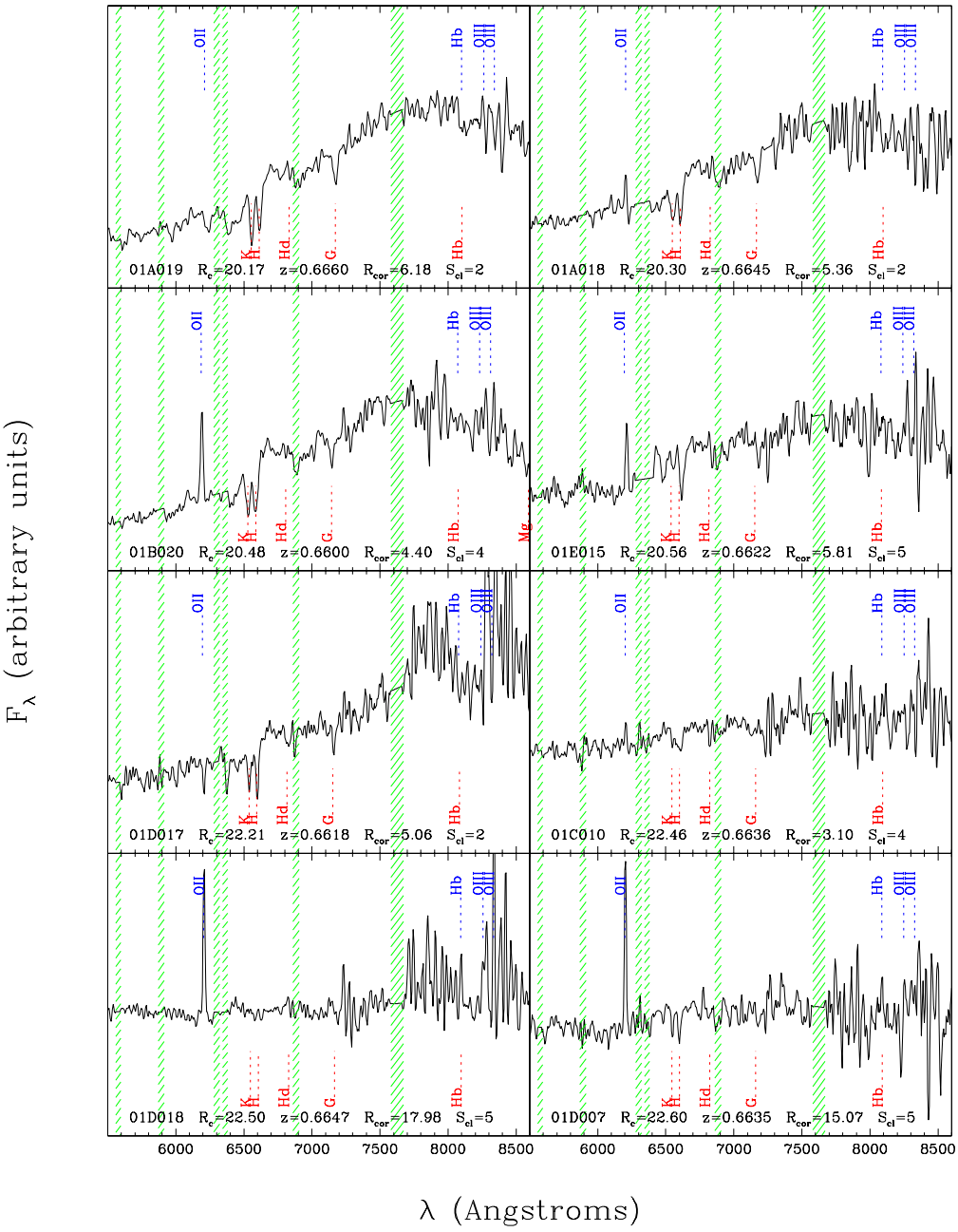

Figure 2.4 Same as Figure 2.3 for cluster RCS J033414-2824.6 at $z_{spec} = 0.66$. This is the highest redshift cluster in our sample, and was observed with the Mgl-LDSS2.

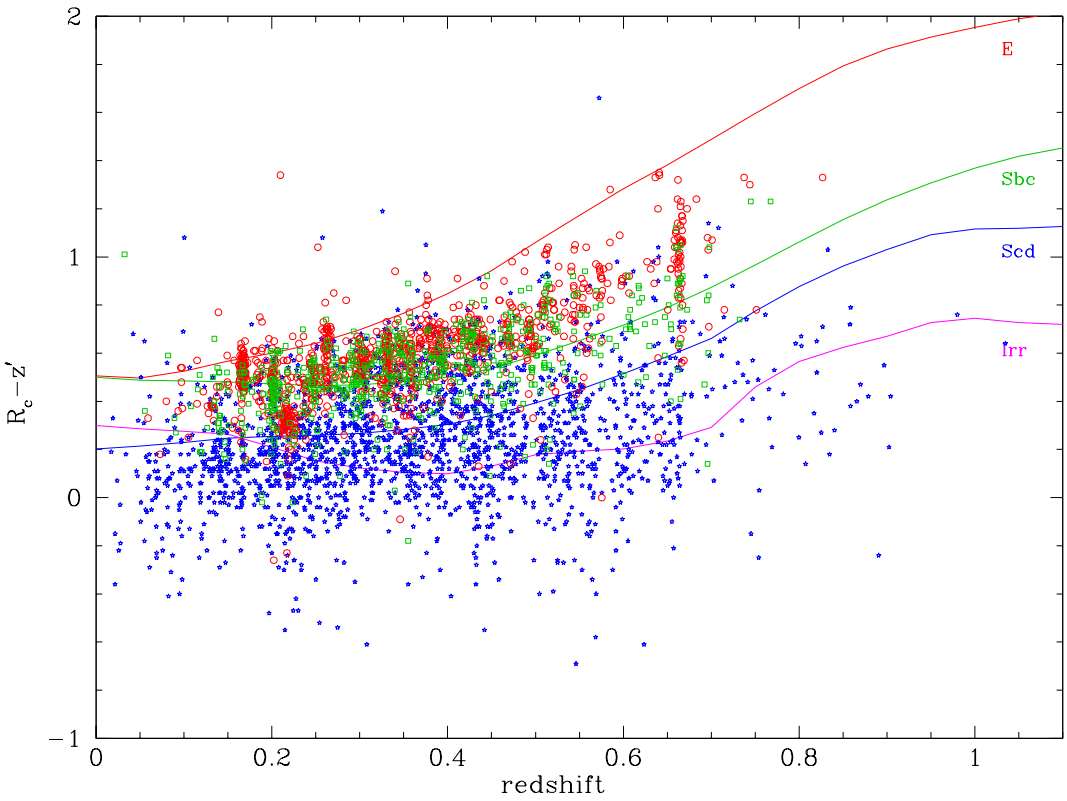

Figure 2.5 Colour distribution with redshift. Red circles are galaxies with early spectral type $S_{cl} = 1$ or 2, green squares are E+A or Sab galaxies with $S_{cl} = 3$ or 4, and blue stars are of late spectral type with $S_{cl} = 5$. Model colours are taken from Bruzual & Charlot (2003). A small population of galaxies has colour more than 0.4mag above that expected for ellipticals; these have large photometric errors, for various reasons (e.g., some are very faint, one is saturated, one is very close to a bright star).

summary, through comparison of our spectroscopic redshifts with photometric redshifts as well as the distribution of velocity differences for redundant observations, we judge that our redshifts are secure, with an average error of $\pm$84km/s.

2.5 Redshift catalogue and completeness

Our redshift data are combined with astrometry and photometry from the RCS catalogues. Of course, we do not obtain redshifts for every galaxy in a given field: our sampling is quite sparse since we can only place $\sim$ 1.4–1.67 slits per square arcminute, and do not successfully measure a redshift for every slit. Moreover, the sampling is non-uniform. Although multiple

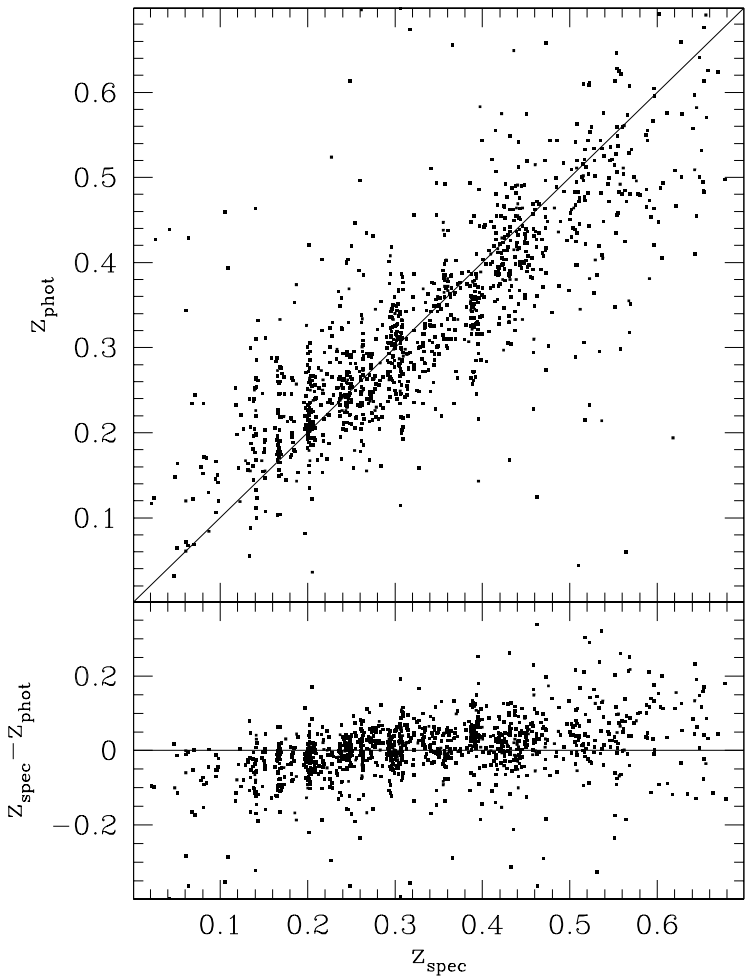

Figure 2.6 Spectroscopic redshifts compared with photometric redshift estimates by Hsieh et al. (2005).

masks significantly smooth out the geometric sampling, it is still an important effect, especially in the crowded central regions of a galaxy cluster. We must therefore compute selection functions in order to compensate for the incompleteness of our redshift catalogs. We do this using the technique of CNOC1 and CNOC2. For each galaxy a selection function $S = S_m S_{xy} S_c$ is computed, composed of magnitude (m), geometric (xy), and colour (c) components. Each galaxy can then be assigned a weight $W = 1/S$. These selection functions are computed directly from the catalogues, for both the R_c and z' filters. The primary selection function is S_m, which is assigned a number between 0 and 1, and the other selection functions are modifiers to S and are normalized to a mean value of 1 over the sample. S_m is computed by finding the fraction of objects with redshifts as a function of magnitude, in magnitude bins of width 0.25mag. In Figure 2.8 we demonstrate the application of S_m to the fraction of galaxies with redshifts;

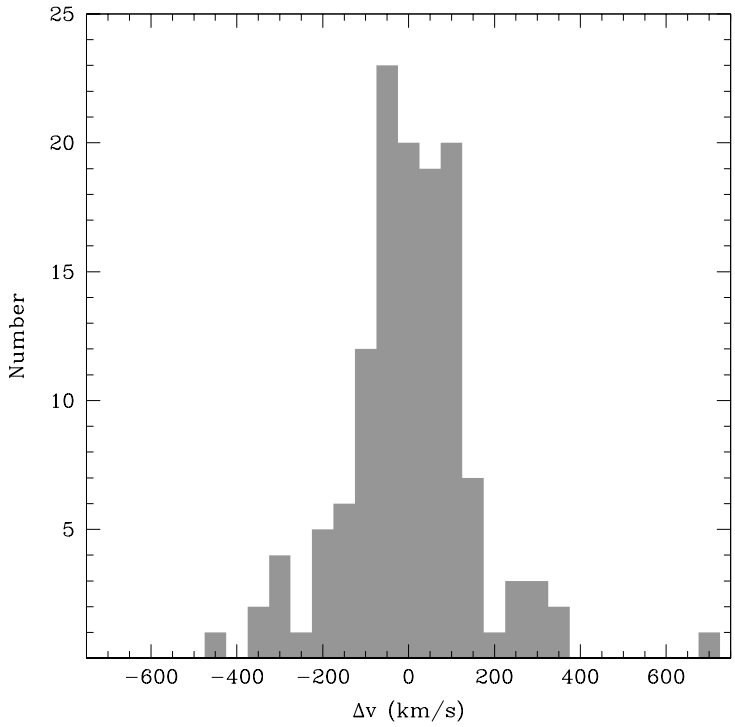

Figure 2.7 Distribution of velocity differences for galaxies with multiple independent redshift estimates.

the effect is minimal at bright magnitudes but significantly boosts the completeness fraction for fainter objects, thus flattening the trend out to $R_c \geq 22$. The geometric selection function S_{xy} is computed by counting galaxies within the magnitude range ± 0.5mag and within $2'$ of the object, while we determine S_c by counting galaxies within a range of colours ± 0.25mag.

In Table 2.5 we present a sample catalogue, showing one example object from each target field. Columns are defined as follows:

1. Object ID. We use two identifiers: first we identify which cluster target this object is associated with, using the Right Ascension (format: hhmm). We then append a string which identifies the slit within this target area, composed of: the field number ("01" for the central field, "02" and "03" for flanking fields, if any), the mask name ("A" for bright, "B" for faint), and the slit number. Slits were numbered by right ascension but usually also sorted into three bins of declination for the multi-tiered (CFH-MOS) masks.

2. Right Ascension, J2000 coordinate.

3. Declination, J2000 coordinate.

4. R_c apparent magnitude.

Table 2.5. Sample redshift catalogue entries, showing the tenth entry for each field

Object ID	RA (J2000)	Dec (J2000)	R_c	$R_c - z'$	redshift	$\pm$	R_{cor}	S_{cl}	W_m	W_c	W_{xy}
0222_01A113	02 : 22 : 56.06	+01 : 47 : 10.1	18.10	0.58	0.31344	022	8.88	2	1.857	1.077	0.538
0223_01A105	02 : 23 : 46.85	+01 : 19 : 30.4	18.87	0.48	0.30876	028	4.46	5	1.625	1.026	1.231
0224_01A015	02 : 24 : 01.79	−02 : 28 : 21.1	18.98	0.69	0.33084	026	5.88	2	3.000	0.500	0.333
0225_01A095	02 : 25 : 22.94	+00 : 07 : 11.9	18.93	0.27	0.26756	022	10.02	5	1.273	0.786	0.786
0334_02A009	03 : 34 : 05.87	−28 : 19 : 22.4	19.23	0.22	0.25465	023	8.82	5	3.667	0.636	0.273
0336_03A020	03 : 36 : 37.14	−28 : 51 : 50.9	19.02	0.50	0.22193	023	7.73	2	1.300	1.058	1.538
0351_02A100	03 : 51 : 52.68	−10 : 01 : 21.6	17.62	0.56	0.18425	022	8.92	2	1.167	0.929	0.857
0436_01A022	04 : 36 : 47.24	−28 : 12 : 09.1	20.20	0.54	0.31823	024	6.31	5	1.500	1.000	1.167
0442_01A014	04 : 42 : 03.80	−28 : 14 : 39.8	19.04	0.55	0.40753	028	5.01	4	1.167	1.013	0.857
0511_01B019	05 : 11 : 19.37	−43 : 40 : 35.1	18.87	0.74	0.36983	024	7.66	2	1.167	0.857	1.029
0515_01A027	05 : 15 : 49.11	−43 : 25 : 47.8	19.63	0.13	0.24274	022	11.55	5	1.250	1.067	1.067
0519_01A023	05 : 19 : 26.17	−42 : 46 : 45.1	18.41	0.21	0.13365	022	8.70	5	15.00	0.733	0.133
0928_01A038	09 : 27 : 53.39	+36 : 49 : 01.9	18.58	0.63	0.24828	026	5.52	2	1.462	0.842	0.684
0930_01A009	09 : 29 : 51.47	+38 : 43 : 46.4	18.80	0.25	0.10536	026	4.76	5	1.500	0.933	1.000
1103_01A014	11 : 03 : 38.13	−04 : 57 : 35.3	20.62	0.84	0.37690	028	4.96	2	1.250	1.120	0.933
1107_01A004	11 : 07 : 41.88	−05 : 15 : 43.7	20.78	0.50	0.37603	028	4.71	5	1.300	1.077	1.795
1120_01A068	11 : 20 : 41.07	+25 : 24 : 03.1	18.42	0.49	0.18273	022	10.22	2	1.778	0.920	0.562
1123_01A011	11 : 23 : 04.78	+25 : 24 : 19.8	19.28	0.58	0.24289	032	3.46	2	1.417	1.098	0.941
1325_01B060	13 : 25 : 19.99	+29 : 19 : 10.1	18.94	0.49	0.28946	023	8.63	2	1.083	1.007	0.923
1332_01A081	13 : 32 : 06.14	+28 : 45 : 45.0	19.10	0.65	0.35101	029	4.64	4	1.500	1.000	0.833
1446_01A110	14 : 46 : 49.03	+09 : 01 : 59.3	18.71	0.47	0.23919	028	4.50	4	1.200	0.917	1.250
1447_01A053	14 : 47 : 07.54	+09 : 49 : 17.2	17.69	0.46	0.20165	024	6.66	2	1.231	0.937	0.948
1452_01B069	14 : 53 : 03.78	+08 : 59 : 05.1	20.15	0.18	0.15563	024	5.85	5	1.650	1.061	1.212
1615_01B064	16 : 15 : 47.37	+30 : 52 : 39.2	18.62	0.24	0.15133	024	6.51	5	1.364	1.027	0.733
1620_01A043	16 : 20 : 24.33	+30 : 42 : 37.7	18.81	0.23	0.14677	026	4.71	4	1.200	1.458	0.833
2115_01B023	21 : 15 : 08.47	−63 : 08 : 20.2	18.54	0.31	0.22591	022	8.07	2	1.222	1.000	0.955
2120_02B020	21 : 20 : 10.70	−62 : 01 : 11.3	18.55	0.26	0.16694	026	4.72	4	1.400	1.000	0.952
2121_02A005	21 : 21 : 33.57	−63 : 37 : 13.7	17.20	-0.02	0.11880	021	12.35	5	1.500	1.111	1.333
2153_01A109	21 : 53 : 28.93	−05 : 46 : 37.5	18.70	0.40	0.21747	030	5.00	4	1.500	1.143	1.667
2157_02A042	21 : 56 : 54.88	−04 : 39 : 31.7	17.68	0.56	0.16953	021	11.59	2	1.667	0.800	0.600
2315_01A070	23 : 15 : 44.95	+00 : 53 : 23.8	18.55	0.63	0.33027	023	7.58	2	2.429	1.029	0.659
2316_01A084	23 : 16 : 59.61	−00 : 06 : 50.9	20.04	0.34	0.26733	034	3.40	4	1.667	0.969	0.750
2317_01A023	23 : 17 : 23.73	−01 : 02 : 36.8	18.56	0.52	0.19092	032	3.45	4	1.300	0.923	0.769
2318_01A093	23 : 18 : 42.92	−00 : 26 : 55.4	18.52	0.67	0.38015	023	8.73	2	1.750	1.000	0.714
2343_01A018	23 : 43 : 57.88	−35 : 17 : 24.3	19.14	0.74	0.49257	030	4.77	2	5.000	0.267	0.333
2347_01B028	23 : 48 : 00.35	−35 : 35 : 05.1	18.23	0.85	0.27051	027	5.12	2	1.154	0.953	1.156

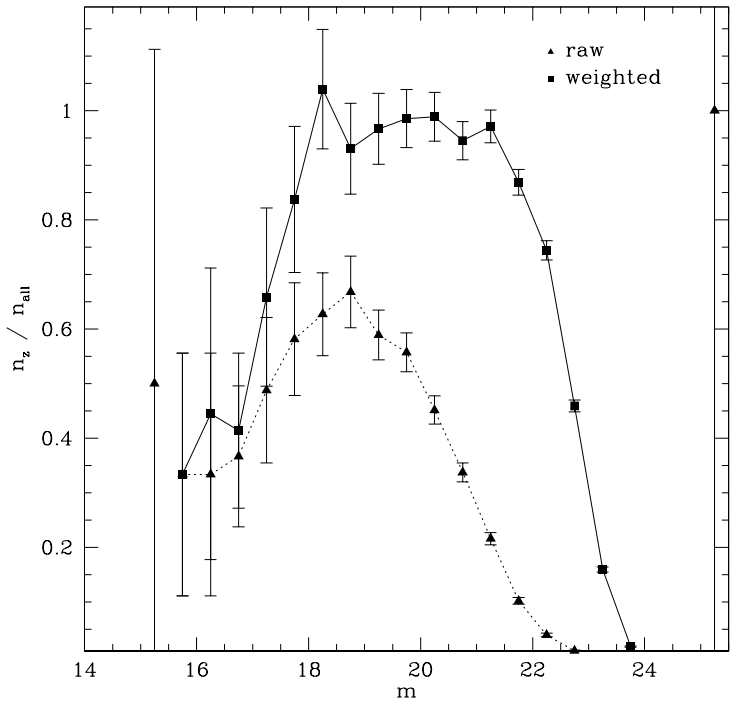

Figure 2.8 Completeness as a function of apparent R_c magnitude, expressed as n_z/n_{all}: the fraction of galaxies in the photometric catalog for which redshifts were measured (solid triangles). Multiplying each galaxy by its empirical magnitude weight to create an up-weighted n_z yields a flatter relation (solid squares).

5. $R_c - z'$ colour.

6. redshift.

7. redshift error, in units of 10^5.

8. Cross-correlation coefficent R_{cor}. This value serves as a rough estimate of the redshift quality, though we stress that all redshifts were visually checked, so that a low R_{cor}-value should not automatically be taken to mean that the redshift is insecure.

9. Spectral classification. Early spectral types have $S_{cl} = 1$ or 2, E+A or Sab galaxies have $S_{cl} = 3$ or 4, and late types have $S_{cl} = 5$. As stated earlier, our spectral classifications are rough; a given galaxy's true spectral type may be off by ± 1 from our estimate. Also, a few AGN were found in the survey, and are designated $S_{cl} = 7$.

10. Magnitude weight W_m.

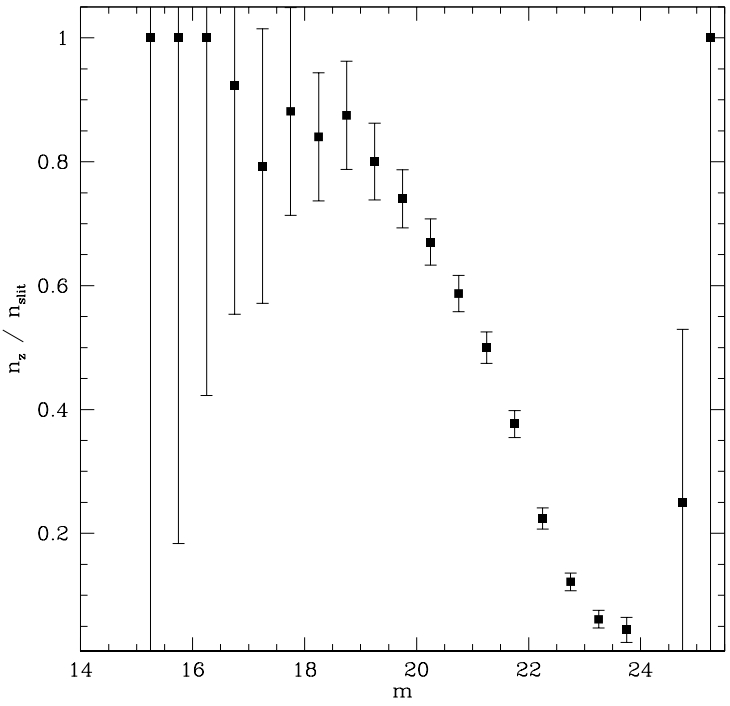

Figure 2.9 Redshift success rate, as a function of galaxy apparent R_c magnitude. Note that the actual success rate for any individual field varies due to exposure time, observing conditions, and so on. Also, all available spaces in any mask were filled with galaxies regardless of magnitude, so the true success rate for any magnitude may not be reflected by the value of n_z/n_{slit} given here.

11. Colour weight W_c.

12. Geometric weight W_{xy}.

We measured a total of 3628 redshifts of 7613 galaxies with spectra, for an overall success rate of 48%. Our success rate is naturally dependent on apparent magnitude, as shown by Figure 2.9 which plots the number of galaxies with measured redshifts divided by the number of galaxies with spectra (i.e., the ratio of successful redshifts to attempted redshifts). We reach 50% success rate at an apparent R_c magnitude of 21.25, (average over all fields). Note that integration times varied for different masks and fields, and all available spaces in our masks were filled with available galaxies regardless of magnitude, so this value does not represent the true success rate for any given magnitude bin.

Our spectroscopic completeness varies for different clusters, due to differences in exposure time, observing conditions, etc. Therefore it is necessary to compute a correction for each

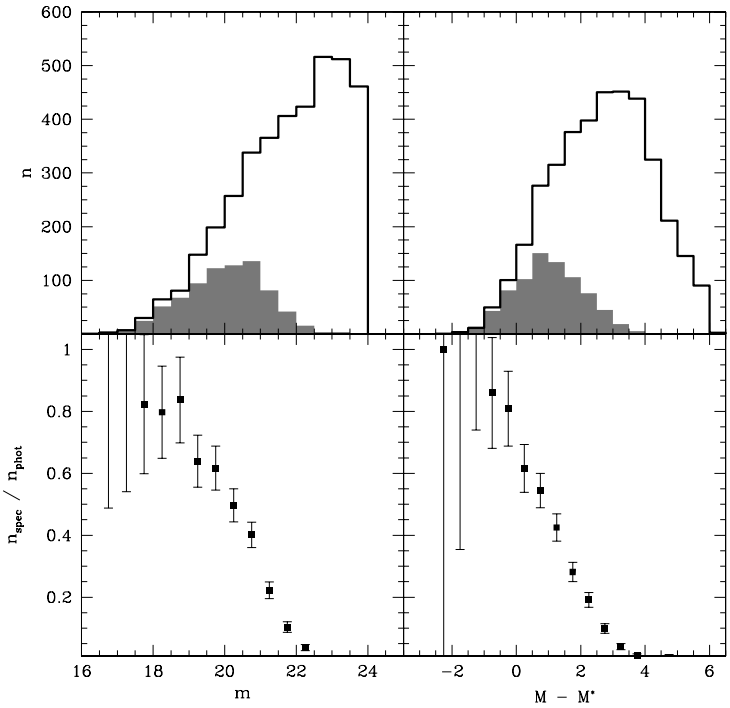

Figure 2.10 Top panels: histograms of the number of galaxies with redshifts, as functions of galaxy apparent R_c magnitude (left) or absolute R_c magnitude relative to M^* (right). The solid-line histogram is n_{zphot}, the weighted number of galaxies in the Hsieh et al. (2005) photometric redshift catalogue. The shaded grey histogram is n_{zspec}, the (unweighted) number of galaxies with spectroscopic redshifts. Bottom panels show the completeness fraction, estimated by dividing these histograms.

cluster. We estimate the completeness using the ratio of the number of galaxies with redshifts (n_z) to the number for which spectra were obtained (n_{spec}). This defines a redshift success rate n_z/n_{slit} in each field: the limit for the field is defined as the magnitude at which n_z/n_{slit} drops below 50%.

Unfortunately, the n_z/n_{slit} success rate can only measure our success at measuring redshifts for the galaxies with spectra, and does not address the many galaxies which did not receive slits at all. The true quantity of interest is: as a function of absolute magnitude, what fraction of cluster galaxies received redshifts relative to the total number of galaxies *in the cluster*? This is not a trivial computation, because of course we do not *a priori* know the number of cluster members. However, we can estimate this fraction for a subset of our clusters by again making use of the Hsieh et al. (2005) photometric redshifts. For each of the 12 clusters covered by the photometric redshift catalogue, we compute n_{spec} and n_{phot} as a function of magnitude.

n_{spec} is simply the number of galaxies in our cluster field whose redshift lies within a given boundary. n_{phot} is similar, but requires an adjustment for the comparatively large errors δz_{phot}: rather than simply count the number of galaxies with z_{phot} within the boundary, we weight each galaxy by W_{phot}, which is the area of overlap between our redshift boundary and the Gaussian curve defined by δz_{phot}, scaled so that an object with error limits entirely within the boundary receives $W_{phot} = 1$. n_{phot} is then simply the sum of all W_{phot} values. We choose $\delta z = 0.06$ for our redshift boundary, which is the average photometric redshift error. The boundary corresponds to an average velocity width of over 13000km/s, an order of magnitude or more larger than the velocity dispersion of a cluster; it will therefore include fore- and background galaxies. Using the number of field and cluster galaxies found in our composite cluster in §4.3, we estimate that approximately 87.5% of the galaxies within this boundary are actually associated with the cluster. We therefore multiply our n_{phot} and n_{spec} values by this fraction. In Figure 2.10 we present the ratio n_{spec}/n_{phot} as a function of apparent magnitude as well as absolute magnitude relative to M^* at the cluster redshift[3]. We reach 25% completeness at approximately $M^* + 2$. We will use this limit in cases for which it is necessary to apply the same objective magnitude limit to all clusters, for instance in computing cluster luminosities. Note that our analysis does not rely solely on this limit to deal with the incompleteness in the survey; weights from our empirical selection functions, including S_m, are always applied to individual galaxies.

Our success in measuring redshifts also depends on apparent galaxy colour, as shown in the top panel of Figure 2.11. Of course, the large redshift range of the clusters means that the expected apparent colours of the cluster galaxies will also have a large range. We bring the colours into a common framework by subtracting the colour of the red-sequence of the parent cluster for each galaxy. For galaxies brighter than $R_c = 21$ our success rate remains above 50% for colors from $\sim$ 1.4mag bluer to $\sim$ 0.4mag redder than the red-sequence. Galaxies redder than the red-sequence lie at higher redshifts than the targeted cluster, so the drop in success rate at the red end is not significant. The success rate is, of course, lower for faint galaxies, but it follows the same trend with colour. Overall, Figure 2.11 shows that we successfully measured redshifts for representative numbers of star-forming and red-sequence galaxies.

2.6 Recovery of RCS Clusters from the Spectroscopic Survey

With redshift catalogs in hand, we can now recover the targeted RCS clusters from our spectroscopic dataset. Pie diagrams for the various cluster fields are given in Figure 2.12; each field is labeled by its sky coordinates (format: hhmm±ddmm). In most cases the cluster is

[3] $M^*(z)$ is estimated using the formula of Yee & López-Cruz (1999), determined from low redshift Abell clusters: $M^* = -22.2 - 1.4z$; the redshift evolution in this relation was adopted from Lin et al. (1999).

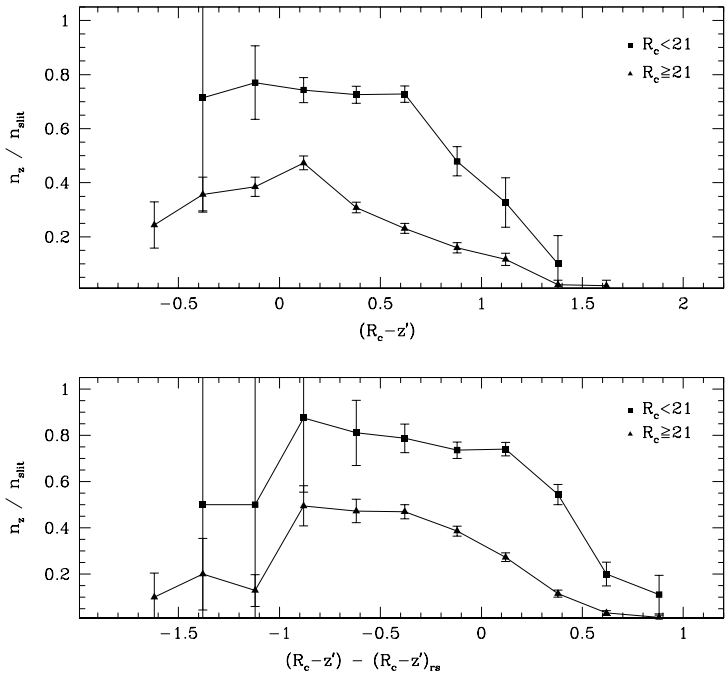

Figure 2.11 Redshift success rate as a function of galaxy colour, split into bright and faint galaxies. Top panel plots success rate as a function of $R_c - z'$ color, while the bottom panel plots success against colours relative to the red-sequence colour at that redshift.

obvious, often appearing as the only major overdensity of galaxies in the field (e.g., 0224-0227, 2317-0102). Sometimes the cluster is easily recovered, but less obvious because the targeted system is poor and/or because there is a substantial amount of foreground structure in the field (e.g., 0930+3841). Unfortunately we also have several cases in which the targeted cluster is not useful for our purposes:

0336-2847 was selected from a preliminary version of the RCS cluster catalogs. It is not included in the final RCS catalog because its peak in the cluster-finding process is of too low significance (approximately 2.6σ, M.D. Gladders, private communication). This cluster is at fairly high redshift and quite poor ($z_{spec} = 0.4665$, $B_{gcR} = 280$); although we found 14 galaxies within a rough cut of 4000km/s, after removal of interloper galaxies only 6 members remained, which is insufficient for reliable dynamical analysis (see §3.3).

0436-2812 is the field centred on RCS J043644-2812.1 ($z_{phot} = 0.29$, $B_{gcR} = 200$). We found 10 galaxies within 4000km/s, but after interloper removal only 9 members remained for

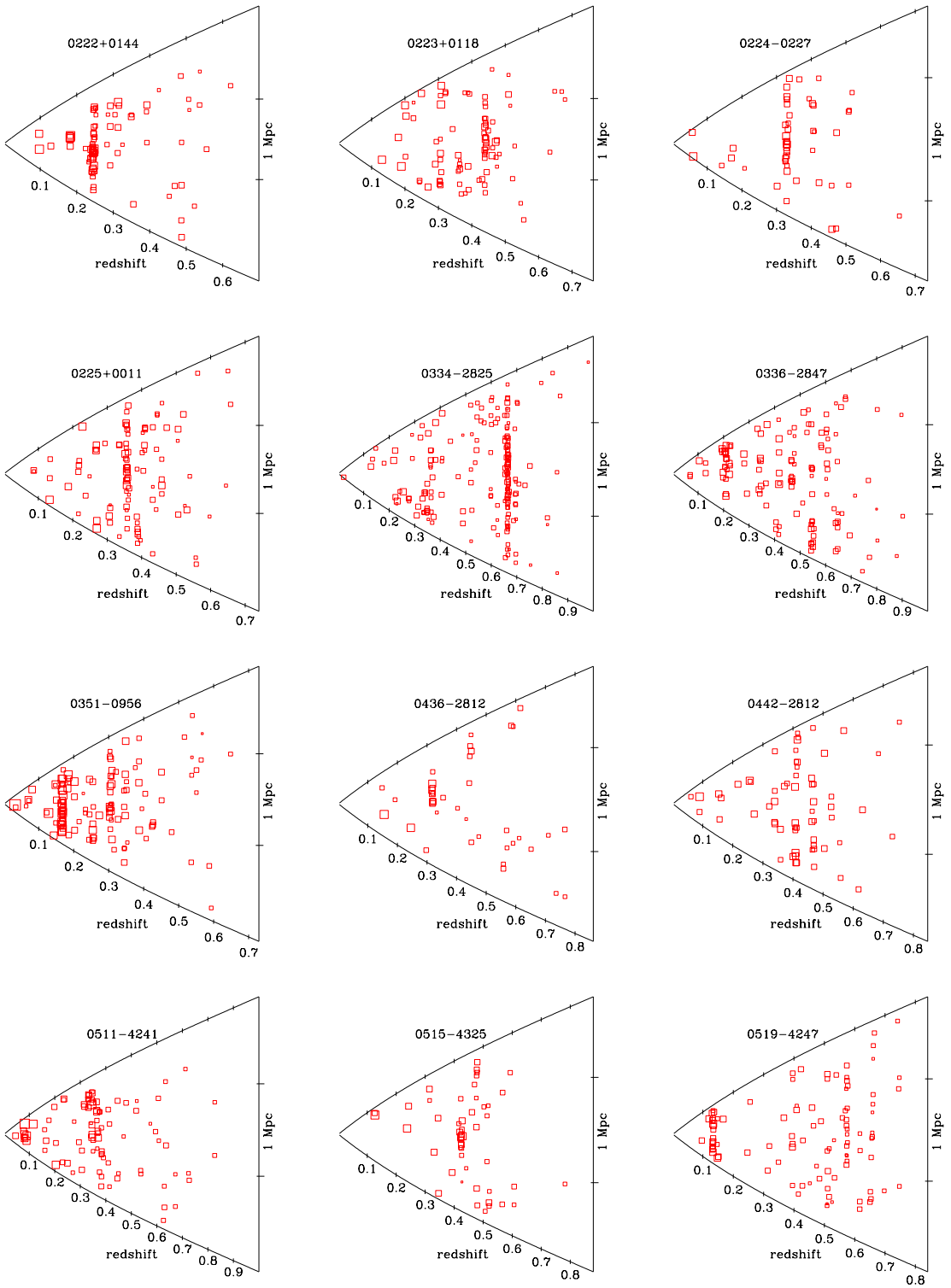

Figure 2.12 "Pie" diagrams, of Right Ascension versus redshift for the cluster fields. Redshift increases from the vertex of the cone outward, and the sky axis is converted to physical units relative to the field centre (a tick-mark of 1Mpc is shown at right).

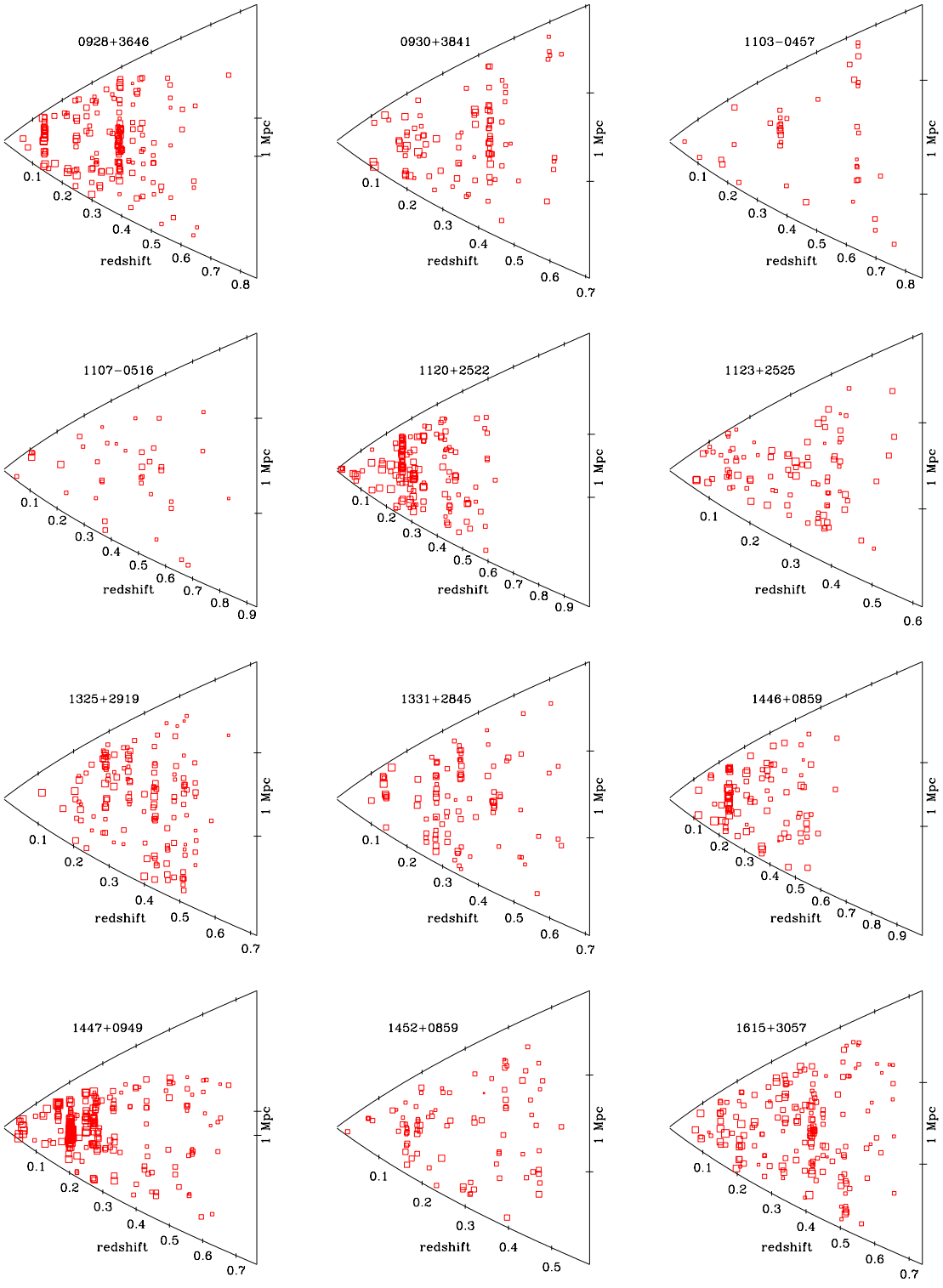

Figure 2.12, continued.

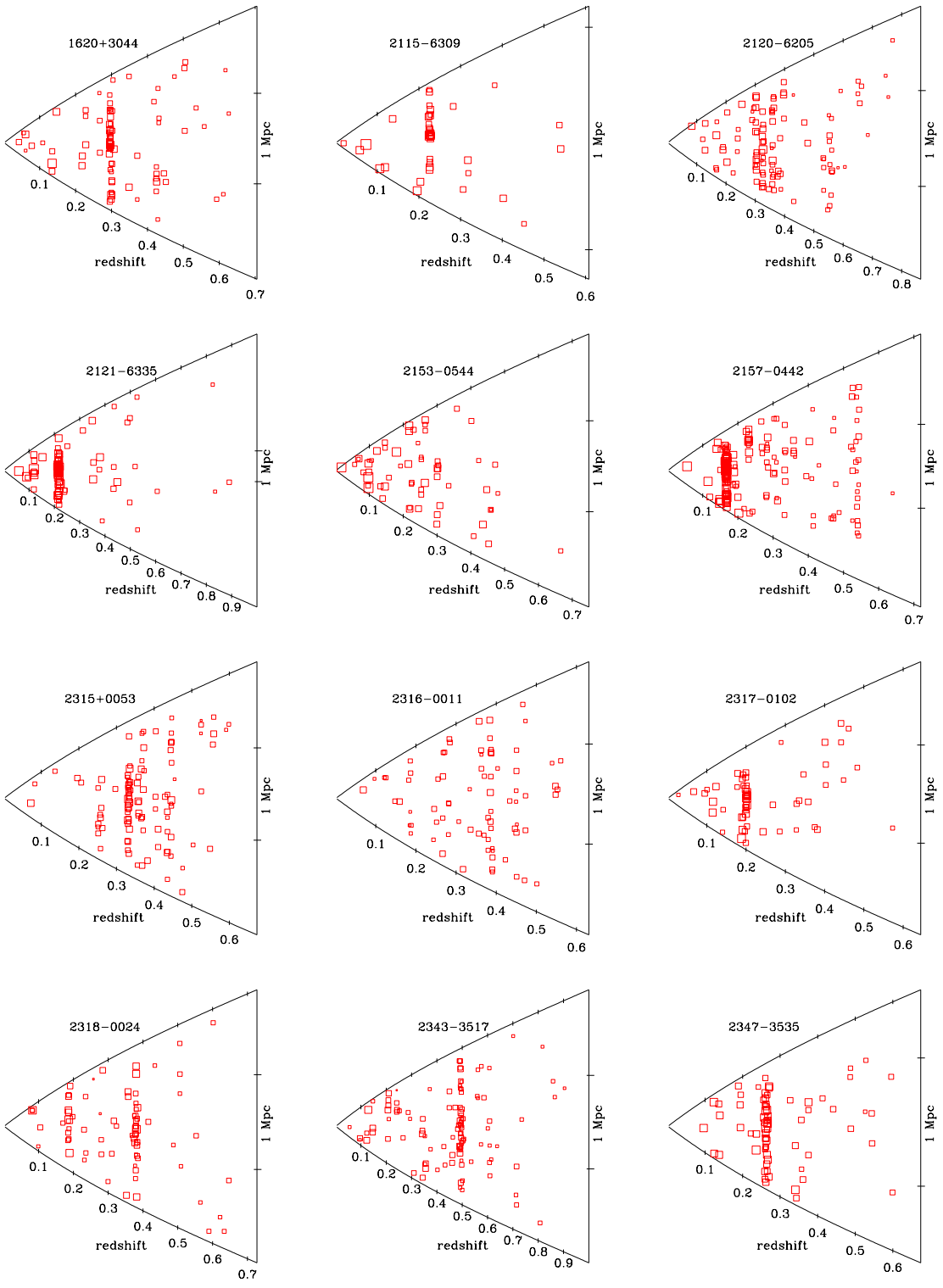

Figure 2.12, continued.

this poor cluster.

0511-4241 is the field centred on RCS J051121-4342.4 ($z_{phot} = 0.35$, $B_{gcR} = 377$). As can easily be seen from the pie diagram, this is not a cluster *per se* but rather a looser association of galaxies whose broad redshift distribution indicates that it is a projection of small groups (which might be undergoing collapse to eventually form a cluster). The RCS survey is expected to select some such systems, because it requires only that the galaxies compose an overdensity in position and colour and has no preference for relaxed systems.

1103-0457 is a target at relatively high redshift (RCS J110340-0458.1 $z_{phot} = 0.48$, $B_{gcR} = 610$) in which the small angular size of the cluster at this redshift conspired with the geometric constraints of slit placement to limit the number of spectroscopic members to 9. Note also that this target was observed with only one Mgl-LDSS pointing, so that only 40 redshifts were obtained for the whole field.

1107-0516 is similarly problematic. Although the system is fairly rich (RCS J110752-0516.5 $z_{phot} = 0.53$, $B_{gcR} = 801$), its high redshift makes it compact on the sky and makes slit placement difficult. Again, this cluster received only one Mgl-LDSS pointing, yielding a total of 40 redshifts for the field. Only 5 spectroscopic members were recovered for the cluster.

1123+2525 is centred on target RCS J112323+2526.6 ($z_{phot} = 0.46$, $B_{gcR} = 474$). A few galaxy systems were found in this region: one with $z_{spec} = 0.3874$ and one with $z_{spec} = 0.4369$. The galaxy distributions of the two systems are not very concentrated on the sky, nor do they appear collapsed in velocity space. Therefore it is possible that the RCS cluster-finder has again identified an unrelaxed system or a projection of several smaller systems. However, this field is quite crowded, especially in the central region where most members should be located, which made slit placement problematic. Therefore it is possible that a true cluster exists in this field and that redshifts were simply not obtained in its core.

1452+0859 was strongly affected by bad weather. We could only measure a few redshifts for this poor high-redshift system (RCS J145258+0858.9 $z_{phot} = 0.59$, $B_{gcR} = 241$), of relatively bright field galaxies, and no redshifts at all could be measured in the central $2'$ of the target.

2153-0544 is a poor system (RCS J215314-0544.0 $z_{phot} = 0.40$, $B_{gcR} = 274$); only 8 spectroscopic members were found.

2316-0011 was affected by observing conditions: this cluster (RCS J231654-0011.1 $z_{phot} = 0.56$, $B_{gcR} = 688$) was meant to be observed using two pointings, each offset by several ar-

cminutes from the cluster centre. Unluckily, due to poor weather only one of these pointings was observed, so that the target cluster sits very close to the edge of our spectroscopic field. Therefore, although we did obtain spectroscopic members, our coverage of the cluster centre is too poor to include the system in our dynamical analysis.

Thus in total we must discard 9 of our 36 fields. We stress that most of this loss is due not to a failure of the red-sequence method or the RCS survey but simply to constraints in slit placement and to weather conditions, often for quite poor systems, making it difficult to obtain redshifts for more than a few member galaxies (although we do always find some galaxies near the cluster photometric redshift). The only unambiguous exception is 0511-4241 which is a system of several smaller groups of galaxies. We find the rate of "false" cluster detections in the RCS survey to be 1 or 2 clusters out of 36 targets, or $3-6\%$ (depending upon whether the ambiguous case of 1123+2525 is included). Note however that some of the remaining RCS systems are actually blends of dynamically separate clusters; these are discussed below in §2.6.2.

2.6.1 Serendipitous Clusters

Fortunately, to compensate for the discarded systems mentioned above, our spectroscopic survey also includes a number of systems observed by chance. A few obvious examples can be seen in the pie diagrams of Figure 2.12: for instance 0351-0956 includes a foreground cluster at $z_{spec} = 0.1676$ and 1120+2522 includes a serendipitous cluster at $z_{spec} = 0.2620$. However, not all of these serendipitous systems should be included in our analysis. In some cases the system is too close to, or even past, the edge of the spectroscopic field (e.g., the 0930+3841 field contains members in the outskirts of RCS J093030+3834.5). Many of the serendipitous clusters are foreground systems, and because they were observed in masks which were designed to find more distant galaxy clusters the cluster members we recover in these systems are intrinsically faint. For instance, the brightest member of the foreground cluster at $z_{spec} = 0.1372$ in the 1331+2845 field has magnitude $R_c = M^* + 1.85$, and the average member has $R_c \approx M^* + 4$. In such cases we are not probing a representative sample of cluster members, and the bright end of the cluster luminosity function is not covered at all making it impossible to accurately measure the luminosity of the cluster.

In order to cull the truly useful clusters from these systems, we employ several criteria. First, we require that the cluster has at least 10 members so that dynamical parameters can be derived. Second, the cluster must be sufficiently distant from the edge of the spectroscopic field so that the central region is well covered (usually at least $2'$). Finally, the luminosity function of the cluster must be well sampled down to our overall survey completeness of $M^* + 2$ (as found in §2.5). Because of the small number of members we obtain in these systems

it is not possible to precisely measure their luminosity functions directly; instead we require that the number of members brighter than $M^* + 2$ be at least as large as the number of members a cluster should have if it has a Schechter luminosity function $\phi(M)$ with a faint-end slope $\alpha = -1$. To estimate this number we first compute the expected fraction of galaxies above $M^* + 2$:

$$f_2 = \frac{\int_{-\infty}^{M^*+2} \phi(M) dM}{\int_{-\infty}^{M^*+6} \phi(M) dM}, \tag{2.1}$$

where the faint limit in the denominator is chosen to be the limit in our survey at which we have essentially no members for any cluster (see Figure 2.10). For $\alpha = -1$ we obtain $f_2 = 0.286$. We then multiply this fraction by 10, which as mentioned above is the minimum number of members (regardless of magnitude) for any of our systems. Thus we find the minimum acceptable number of members above $M^* + 2$ must be $N_{bright} \geq f_2 \times N_{min} = 0.286 \times 10$, or approximately $N_{bright} \geq 3$, and we discard any serendipitous systems with fewer than 3 members above $M^* + 2$. Although this criterion is sensitive to our choice for the faint-end slope of the luminosity function, note that it is used only to exclude extreme cases — most clusters have more than 10 members, so that they should be well above this limit.

After applying these criteria we retain 6 serendipitous systems, which along with our targets yield a total of 33 clusters for use in our analysis.

2.6.2 Special Cases: blends and low-significance clusters

As we will show in further sections of this chapter, the data provided in the RCS cluster catalog give a good basic sketch of most of our clusters. However, a handful of clusters require some additional attention:

RCS J035139-0956.3 This RCS "cluster" ($z_{phot} = 0.36$, $B_{gcR} = 792$) is in fact a blend of two clusters at $z_{spec} = 0.1676$ and $z_{spec} = 0.3057$, which we denote by suffixes "A" and "B". The clusters are separated by over 3×10^4km/s, and so are dynamically separate and non-interacting. They do have significant overlap on the sky (their centres are separated by $1.7'$). Blends occur because the colour slices used by the cluster-finding algorithm are wide compared with the redshift boundaries of real clusters (see GY05 for discussion). In this case, the low-redshift cluster is below the targeted redshift range for RCS clusters: the RCS survey was not designed to separate these systems.

RCS J044207-2815.0 This system ($z_{phot} = 0.47$, $B_{gcR} = 722$) is also a blend of two clusters ($z_{spec} = 0.4108$ and $z_{spec} = 0.4659$) that the RCS cluster-finder identifies as a single peak. The cluster centres are separated by only $0.8'$. We estimate their individual richnesses using the cluster centres computed from the spectroscopic members (see §3.2) and colour slices computed using the spectroscopic redshifts, and find that they contribute

almost equally to the overall richness of the system: $B_{gcR} = 538$ and 720 for the low- and high-redshift cluster respectively. As above, these clusters are separated by more than 10^4km/s, so they are not interacting.

RCS J092830+3646.0† This cluster was observed serendipitously in the field of RCS J092821+3646.5. It has quite a low redshift ($z_{spec} = 0.1404$) and appears as a 2.5σ peak in the first colour slice of the cluster-finding process (private communication with M.D. Gladders). We use the † symbol to differentiate this low-significance cluster.

RCS J132523+2919.4B This cluster ($z_{spec} = 0.2899$) was also serendipitously observed. It has no entry in the RCS catalogue, but rather forms a small secondary peak to RCS J132523+2919.4 ($z_{spec} = 0.4291$) in the cluster-finding process.

RCS J133212+2847.5 The low richness value for this cluster ($z_{phot} = 0.35$, $B_{gcR} = 34$) reflects the fact that it is a low-concentration peak in the cluster-finding process. This can also be seen in Figure 3.2; the system does not appear very concentrated, so there is some difficulty in defining the cluster centre which is an important ingredient in computing B_{gc}. In addition to the $z_{spec} = 0.2817$ cluster we recovered at the centre of the field, we also found two more clusters towards the edges of our spectroscopic field, which contribute to the cluster-finding signal.

Richness and redshift estimates as given in the RCS cluster catalogue are somewhat unreliable for the blended clusters described above. Also, we note that the uncertainties on the B_{gcR} estimates for the blended clusters are of the same order as the uncertainties for other clusters ($\delta B_{gcR} = 100$–200), so it appears that a limit on richness errors cannot be expected to eliminate blended systems. We exclude all blends from the redshift and richness relations of the next chapter; both components of the blends are excluded (except for RCS J132523+2919.4A, because the "B" cluster forms only a weak secondary peak at substantially lower redshift, so that the z_{phot} and B_{gcR} of the main peak should be unaffected). We also exclude the low-significance clusters not included in the RCS cluster catalogue. N.B., these clusters are included in all other analysis, we merely exclude them from relations involving z_{phot} or B_{gcR}.

Blends such as those described above will likely also contaminate larger richness-selected samples for which spectroscopy is unavailable. These contaminants may affect studies in which optical richness is used as a proxy for mass (for instance in estimating the cluster abundance as a function of mass), contributing to the scatter of the richness-mass calibration. Of our 33 clusters, 4 are blends — i.e., we estimate the RCS survey to have 12% contamination from blends. However note that this contamination rate is a function of richness: for $B_{gcR} \geq 500$ the fraction drops to 8% contamination.

Chapter 3

Cluster Properties

3.1 Introduction

In this chapter we present the global properties of clusters observed in the spectroscopic survey described in chapter 2. These clusters span a large range in optical richness and a moderate redshift range. In §3.2 we report basic global properties for each cluster such as position and redshift.

As mentioned in §2.2.1, the RCS cluster-finding technique utilizes the signature of red galaxies in a colour-magnitude diagram. Because these red galaxies are passively evolving, the position of this red sequence is a simple function of redshift, and can thus be used to estimate cluster redshift. By comparing to the spectroscopic redshifts in our sample, we examine the accuracy of the photometric redshifts given in the RCS survey data. This calibration is an important ingredient in analyses of larger cluster samples, for which spectroscopic observations may not be practical.

In §3.3 we make dynamical estimates of quantities such as velocity dispersion and mass. First, we discuss the removal of contaminating field galaxies, introducing a variant on the usual recipes for cluster membership assignment. We then compute the global velocity dispersions for our clusters using a robust estimator. In addition to estimating the velocity dispersions, it is desirable to estimate the virial radii: we discuss the reliability of estimates of virial radius for our targeted survey. Using these ingredients of velocity and physical scale, we compute the cluster virial masses and luminosities. We also discuss the effect of shifting the cluster centroid on these properties.

In §3.4 we present the scaling relation between mass and richness for the clusters in our survey. The calibration of the cheaply observable richness estimate B_{gcR} (which was computed directly from the RCS survey data), to the more expensive cluster mass estimated from our spectroscopic data, is very important for analyses requiring very large cluster samples. Also crucial are estimates of the scatter in this relation, and possible redshift evolution. Finally,

we present the relation between cluster mass and luminosity, which connects the large dark matter haloes that host clusters to the galaxy populations they contain. This relation should therefore be useful in confronting models of structure and star formation.

3.2 Cluster Positions and Redshifts

Cluster redshifts are computed in a two-step process. An initial estimate is made using a friends-of-friends algorithm to define an initial group and computing the median redshift of the group. We then make a rough cut of 4000km/s around the initial redshift estimate, and compute an iterative biweight centroid estimate (equation 5 of Beers et al. 1990)

$$z_{clust} = M + \frac{\sum_{|u_i|<1}(z_i - M)(1-u_i^2)^2}{\sum_{|u_i|<1}(1-u_i^2)^2}\,, \tag{3.1}$$

where $u_i = \frac{(z_i - M)}{6MAD}$, MAD is the median absolute deviation and M is the z_{clust} estimate from the previous iteration (or the median for the first iteration). The resulting z_{clust} value is insensitive to the initial friends-of-friends group chosen.

We use four estimates of the cluster central position. The first estimate, which we will refer to as $(\mathrm{RA,Dec})_{spec}$ is made from the spectroscopic members only: as with the cluster redshift, we make a biweight estimate of the centre from all galaxies within 4000km/s of the cluster peak. Two centroid estimates are made from galaxies along the red sequence. We define a red sequence envelope in the same way as is done by GY05 in making B_{gcR} estimates for the clusters: the red and blue edges are defined to be 0.2mag redder than the red sequence and 0.25mag bluer than an Sbc galaxy at that redshift[1], respectively. We include as "red sequence members" any galaxies lying within this colour slice, and in the magnitude range $M^* - 3$ to $M^* + 2$. The two centroid estimates are as follows: $(\mathrm{RA,Dec})_{BCG}$ is the location of the brightest red sequence member, and $(\mathrm{RA,Dec})_{RS}$ is the weighted-mean centroid of the red-sequence members (we use Gaussian weights, computing the overlap of the colour error for each galaxy with the red sequence colour slice). Finally we also use $(\mathrm{RA,Dec})_{GY05}$, the centre positions as given in the RCS cluster catalogs, which were computed from the smoothed galaxy distribution used for cluster identification (see GY05 for details). Note that this last estimate is not used for the blends and low-significance clusters described above in §2.6.2. We provide the various centre locations in Table 3.1. Overlays of the (RA,Dec) distributions of cluster members, along with centroid positions, over the R_c band images of the cluster fields, are shown in Figure 3.2. The results presented in §3.3 are computed for the $(\mathrm{RA,Dec})_{spec}$ centroid estimate; in §3.3.6 we will show that the choice of centroid makes little difference to the dynamical properties of the clusters.

[1] using model colours from Bruzual & Charlot (2003)

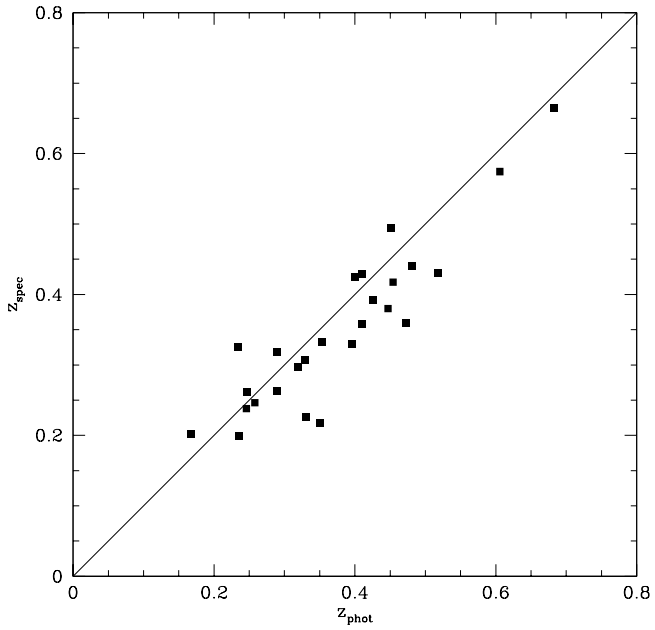

Figure 3.1 Spectroscopic versus red-sequence photometric redshift estimates of the clusters. A 1:1 ratio is shown as a solid line.

Redshift estimates for the clusters are given in columns 2 and 4 of Table 3.2. The spectroscopic redshifts agree well with the red-sequence photometric redshift estimates provided by the RCS cluster-finding algorithm. In Figure 3.1 we compare the z_{spec} and z_{phot} values: we obtain an rms scatter of 0.04. However, note that the photometric redshifts given in GY05 include empirical corrections, some of which were made from the very clusters we examine in this work. Also, a bisector fit yields the following relation: $z_{spec} = -0.006 + 0.948 z_{phot}$ — i.e., the z_{phot} values slightly overestimate the true redshifts. Nevertheless, the photometric estimates in the GY05 catalogues do provide redshift estimates accurate to ~ 0.04.

Table 3.1. Cluster centres

Cluster Name	$(RA,Dec)_{spec}$	$(RA,Dec)_{BCG}$	$(RA,Dec)_{RS}$	$(RA,Dec)_{GY05}$
RCS J022240 + 0144.5	02 : 22 : 41.67 +01 : 45 : 09.9	02 : 22 : 40.88 +01 : 44 : 42.4	02 : 22 : 40.33 +01 : 45 : 07.0	02 : 22 : 40.72 +01 : 44 : 31.1
RCS J022331 + 0118.4	02 : 23 : 30.73 +01 : 19 : 05.6	02 : 23 : 29.78 +01 : 18 : 56.2	02 : 23 : 30.58 +01 : 19 : 06.5	02 : 23 : 31.22 +01 : 18 : 29.9
RCS J022516 + 0011.5	02 : 25 : 17.59 +00 : 11 : 56.7	02 : 25 : 20.24 +00 : 10 : 35.8	02 : 25 : 17.83 +00 : 11 : 42.2	02 : 25 : 16.41 +00 : 11 : 32.7
RCS J022402 − 0227.8	02 : 24 : 02.42 −02 : 27 : 41.0	02 : 24 : 03.34 −02 : 28 : 15.8	02 : 24 : 02.69 −02 : 27 : 31.4	02 : 24 : 02.68 −02 : 27 : 49.3
RCS J033414 − 2824.6	03 : 34 : 12.84 −28 : 24 : 35.7	03 : 34 : 13.96 −28 : 23 : 38.5	03 : 34 : 12.67 −28 : 24 : 35.6	03 : 34 : 14.60 −28 : 24 : 36.1
RCS J035139 − 0956.3A	03 : 51 : 39.58 −09 : 56 : 40.2	03 : 51 : 44.07 −09 : 58 : 31.0	03 : 51 : 41.32 −09 : 56 : 57.2	···
RCS J035139 − 0956.3B	03 : 51 : 42.28 −09 : 55 : 04.7	03 : 51 : 39.95 −09 : 53 : 59.6	03 : 51 : 41.50 −09 : 55 : 47.8	···
RCS J044207 − 2815.0A	04 : 42 : 10.01 −28 : 15 : 09.3	04 : 42 : 13.57 −28 : 15 : 22.8	04 : 42 : 09.33 −28 : 15 : 03.6	···
RCS J044207 − 2815.0B	04 : 42 : 07.00 −28 : 14 : 40.9	04 : 42 : 08.18 −28 : 15 : 03.7	04 : 42 : 06.77 −28 : 14 : 43.8	···
RCS J051536 − 4325.5	05 : 15 : 36.77 −43 : 25 : 02.0	05 : 15 : 37.15 −43 : 25 : 14.2	05 : 15 : 37.25 −43 : 25 : 03.7	05 : 15 : 36.59 −43 : 25 : 34.6
RCS J051919 − 4247.8	05 : 19 : 21.76 −42 : 47 : 50.9	05 : 19 : 19.59 −42 : 47 : 52.2	05 : 19 : 21.55 −42 : 47 : 38.8	05 : 19 : 19.56 −42 : 47 : 51.3
RCS J092821 + 3646.5	09 : 28 : 27.44 +36 : 46 : 38.6	09 : 28 : 21.19 +36 : 46 : 28.0	09 : 28 : 25.45 +36 : 46 : 31.5	09 : 28 : 21.82 +36 : 46 : 34.4
RCS J092830 + 3646.0†	09 : 28 : 30.11 +36 : 46 : 00.8	09 : 28 : 40.62 +36 : 44 : 30.2	09 : 28 : 32.43 +36 : 45 : 38.7	···
RCS J093010 + 3841.2	09 : 30 : 13.64 +38 : 40 : 34.4	09 : 30 : 10.85 +38 : 41 : 29.0	09 : 30 : 12.63 +38 : 40 : 44.2	09 : 30 : 10.41 +38 : 41 : 13.5
RCS J112051 + 2527.6	11 : 20 : 47.76 +25 : 26 : 19.2	11 : 20 : 50.54 +25 : 27 : 35.6	11 : 20 : 48.80 +25 : 27 : 02.4	11 : 20 : 51.06 +25 : 27 : 37.1
RCS J112038 + 2522.1	11 : 20 : 36.15 +25 : 20 : 34.8	11 : 20 : 37.64 +25 : 22 : 18.0	11 : 20 : 36.65 +25 : 21 : 02.9	11 : 20 : 38.54 +25 : 22 : 06.6
RCS J132523 + 2919.4A	13 : 25 : 22.72 +29 : 19 : 44.9	13 : 25 : 23.64 +29 : 19 : 10.6	13 : 25 : 22.95 +29 : 19 : 46.6	13 : 25 : 23.72 +29 : 19 : 29.5
RCS J132523 + 2919.4B	13 : 25 : 30.90 +29 : 19 : 07.9	13 : 25 : 35.44 +29 : 19 : 38.8	13 : 25 : 34.37 +29 : 19 : 09.9	···
RCS J133212 + 2847.5	13 : 31 : 58.17 +28 : 45 : 19.3	13 : 31 : 50.67 +28 : 45 : 40.1	13 : 31 : 58.44 +28 : 45 : 54.2	···
RCS J144632 + 0859.2	14 : 46 : 36.66 +08 : 59 : 25.6	14 : 46 : 35.22 +08 : 59 : 12.4	14 : 46 : 35.06 +08 : 59 : 22.4	14 : 46 : 32.67 +08 : 59 : 17.2
RCS J144708 + 0949.0	14 : 47 : 10.07 +09 : 49 : 27.3	14 : 47 : 14.41 +09 : 48 : 47.2	14 : 47 : 08.43 +09 : 49 : 03.3	14 : 47 : 08.18 +09 : 49 : 01.8
RCS J161547 + 3057.3	16 : 15 : 46.46 +30 : 55 : 41.5	16 : 15 : 53.43 +30 : 55 : 46.4	16 : 15 : 46.74 +30 : 56 : 00.7	16 : 15 : 47.31 +30 : 57 : 18.6
RCS J162008 + 3046.7	16 : 20 : 04.21 +30 : 45 : 32.8	16 : 20 : 04.23 +30 : 44 : 55.3	16 : 20 : 05.25 +30 : 45 : 51.6	16 : 20 : 08.08 +30 : 46 : 42.6
RCS J211519 − 6309.5	21 : 15 : 19.96 −63 : 09 : 25.0	21 : 15 : 19.16 −63 : 09 : 34.5	21 : 15 : 18.81 −63 : 09 : 11.2	21 : 15 : 19.44 −63 : 09 : 30.6
RCS J211945 − 6209.8	21 : 19 : 57.69 −62 : 08 : 41.0	21 : 19 : 59.82 −62 : 08 : 34.8	21 : 19 : 58.88 −62 : 08 : 47.5	21 : 19 : 45.88 −62 : 09 : 49.2
RCS J212005 − 6204.8	21 : 20 : 04.20 −62 : 05 : 03.1	21 : 20 : 08.69 −62 : 04 : 09.5	21 : 20 : 06.24 −62 : 05 : 03.7	21 : 20 : 05.08 −62 : 04 : 52.5
RCS J212134 − 6335.8	21 : 21 : 54.70 −63 : 35 : 36.0	21 : 21 : 43.20 −63 : 35 : 50.4	21 : 21 : 51.92 −63 : 35 : 38.1	21 : 21 : 34.13 −63 : 35 : 52.4
RCS J215700 − 0441.9	21 : 56 : 58.62 −04 : 41 : 35.7	21 : 57 : 00.55 −04 : 42 : 03.3	21 : 56 : 59.69 −04 : 41 : 15.9	21 : 57 : 00.08 −04 : 41 : 57.6
RCS J231544 + 0052.8	23 : 15 : 43.57 +00 : 52 : 24.0	23 : 15 : 44.99 +00 : 53 : 12.8	23 : 15 : 43.89 +00 : 52 : 39.1	23 : 15 : 44.29 +00 : 52 : 51.6
RCS J231736 − 0103.0	23 : 17 : 34.83 −01 : 02 : 50.6	23 : 17 : 36.33 −01 : 02 : 57.7	23 : 17 : 35.37 −01 : 02 : 53.2	23 : 17 : 36.36 −01 : 03 : 02.8
RCS J231830 − 0024.5	23 : 18 : 29.74 −00 : 24 : 56.4	23 : 18 : 30.38 −00 : 24 : 40.8	23 : 18 : 30.18 −00 : 24 : 49.4	23 : 18 : 30.45 −00 : 24 : 32.5
RCS J234356 − 3517.5	23 : 43 : 57.63 −35 : 17 : 44.7	23 : 43 : 57.85 −35 : 17 : 24.9	23 : 43 : 56.69 −35 : 17 : 33.6	23 : 43 : 56.35 −35 : 17 : 32.5
RCS J234748 − 3535.1	23 : 47 : 49.28 −35 : 34 : 47.8	23 : 47 : 49.20 −35 : 35 : 10.9	23 : 47 : 48.68 −35 : 35 : 03.3	23 : 47 : 48.43 −35 : 35 : 07.9

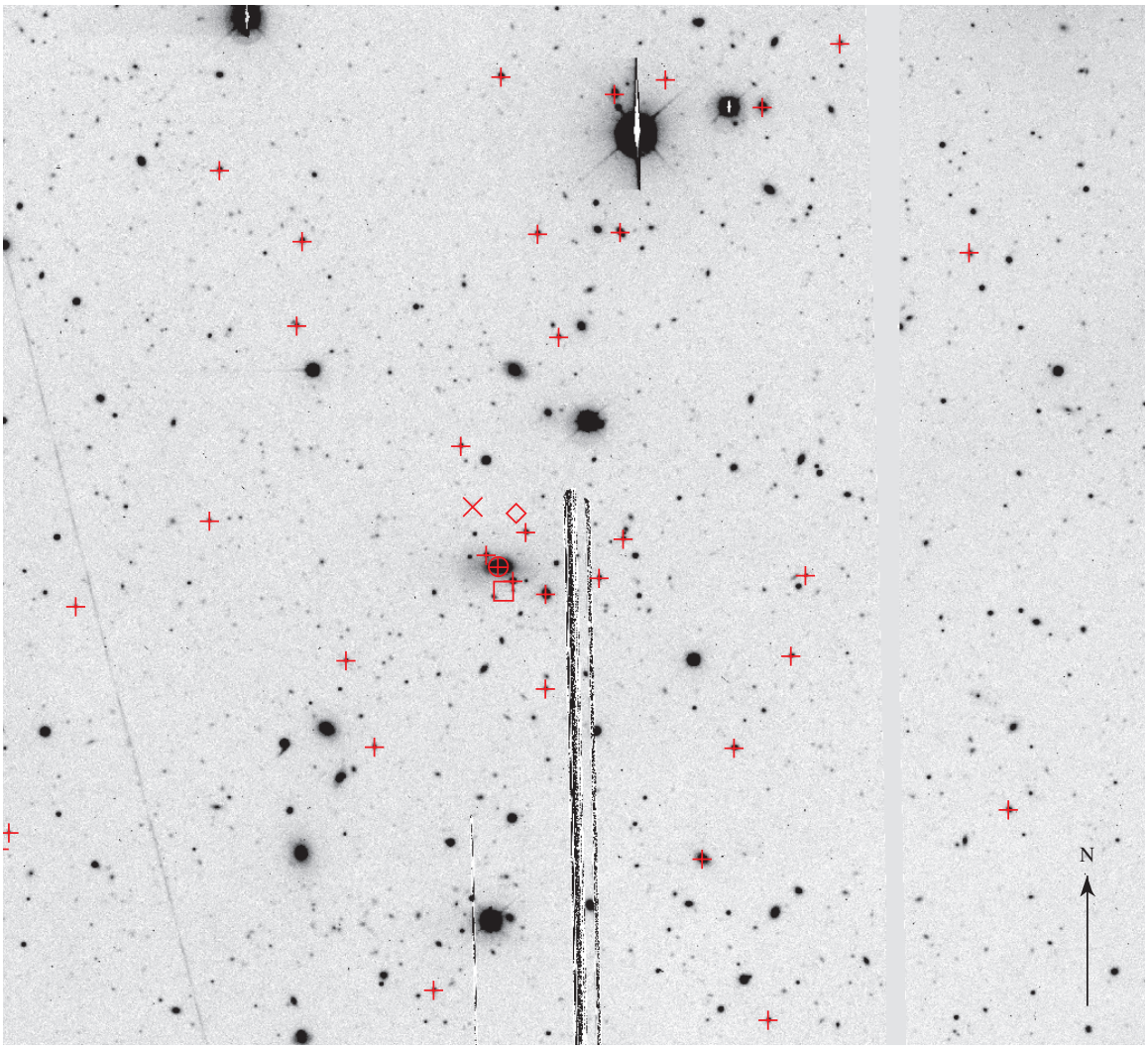

Figure 3.2 R_c band images: field of cluster RCS J022240+0144.5 ($z_{spec} = 0.2460$). Galaxies within 4000km/s of the cluster redshift are shown as crosses. Cluster centroids are shown as a circle, x, diamond, and box, for $(\mathrm{RA,Dec})_{spec}$, $(\mathrm{RA,Dec})_{BCG}$, $(\mathrm{RA,Dec})_{RS}$, and $(\mathrm{RA,Dec})_{GY05}$, respectively. North is marked by an arrow of length one arcminute.

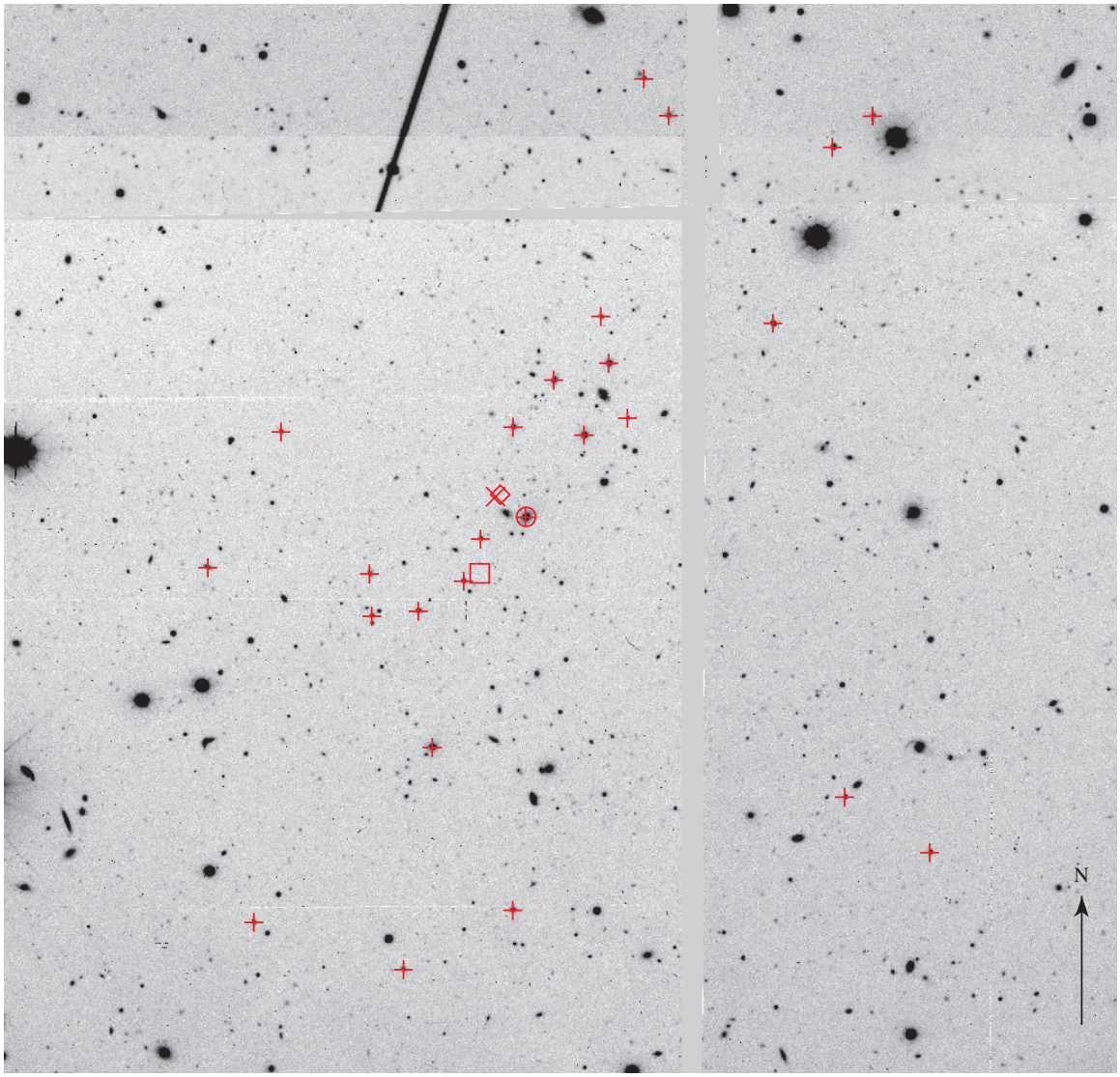

Figure 3.2, continued: cluster RCS J022331+0118.4 at redshift $z_{spec} = 0.4403$.

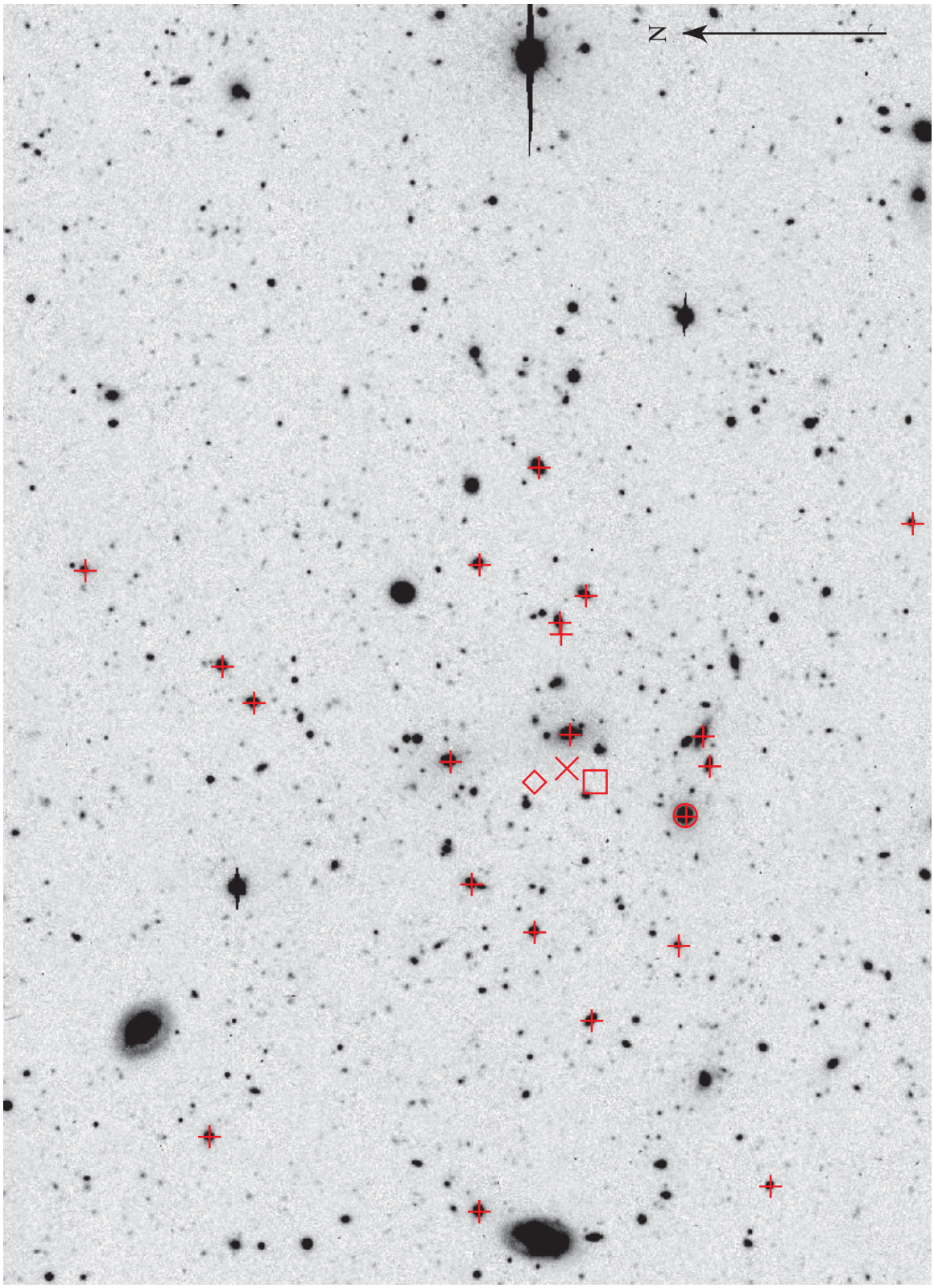

Figure 3.2, continued: cluster RCS J022402-0227.8 ($z_{spec} = 0.3295$).

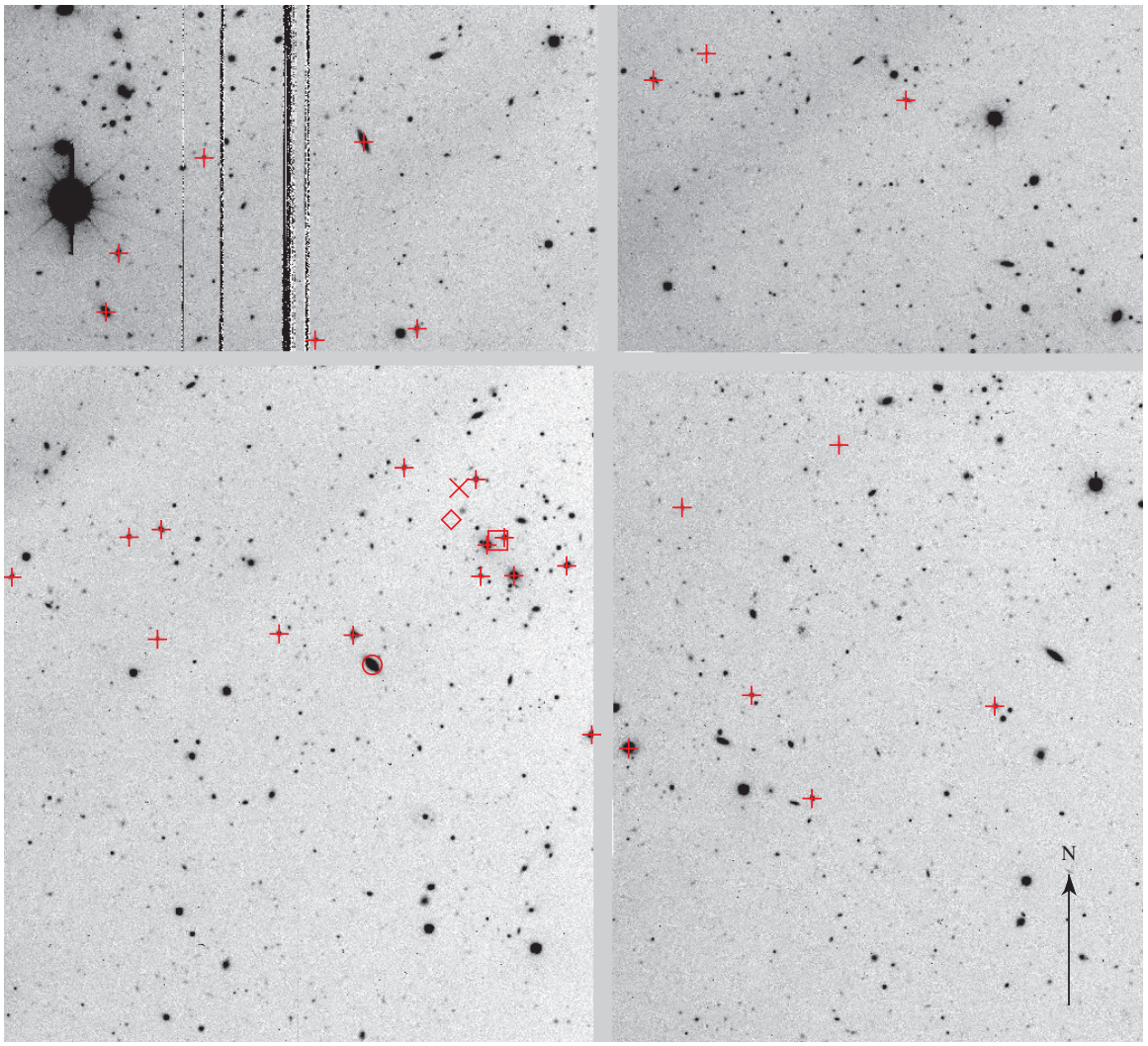

Figure 3.2, continued: cluster RCS J022516+0011.5 ($z_{spec} = 0.3576$).

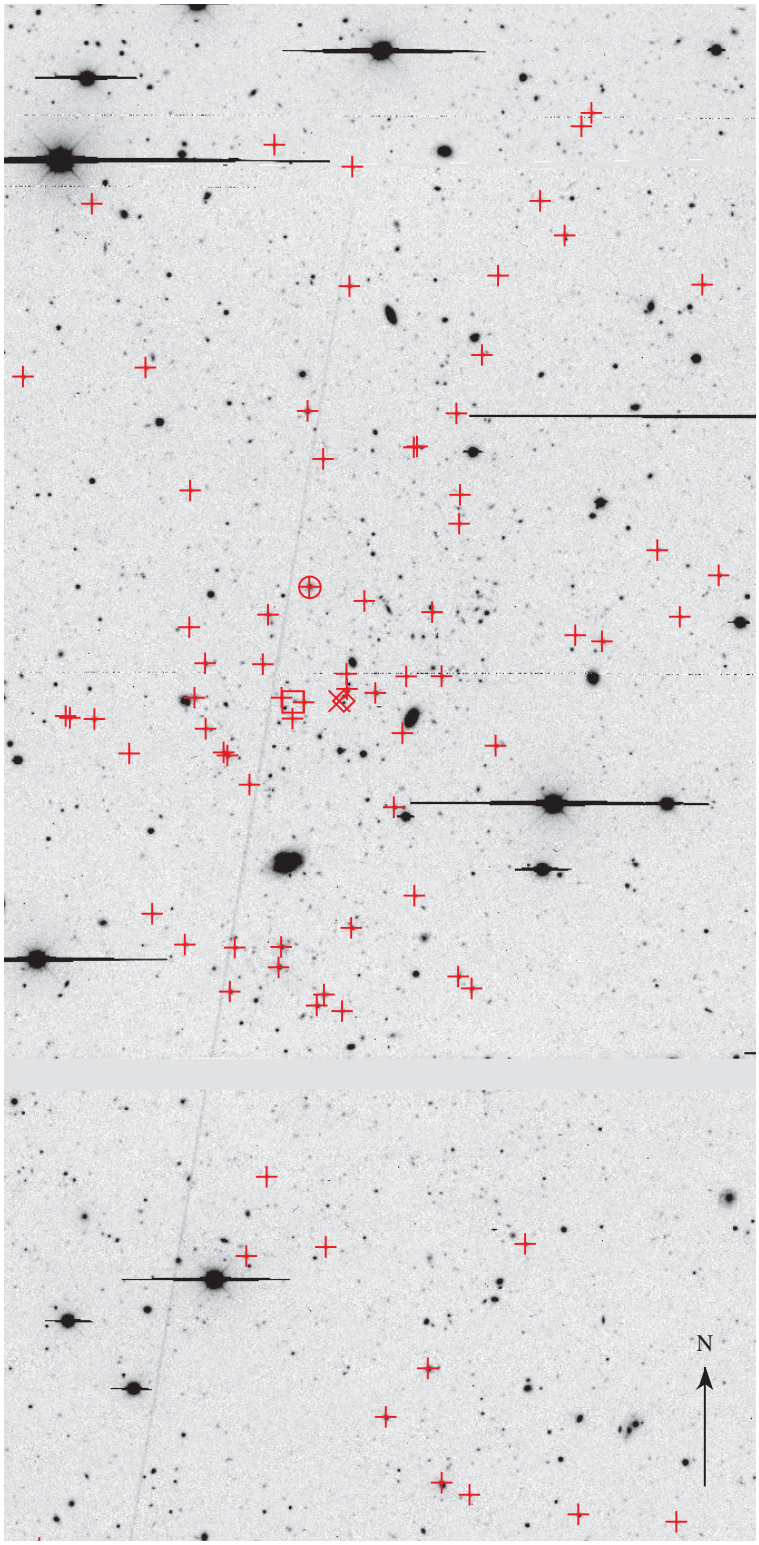

Figure 3.2, continued: cluster RCS J033414-2824.6 ($z_{spec} = 0.6642$).

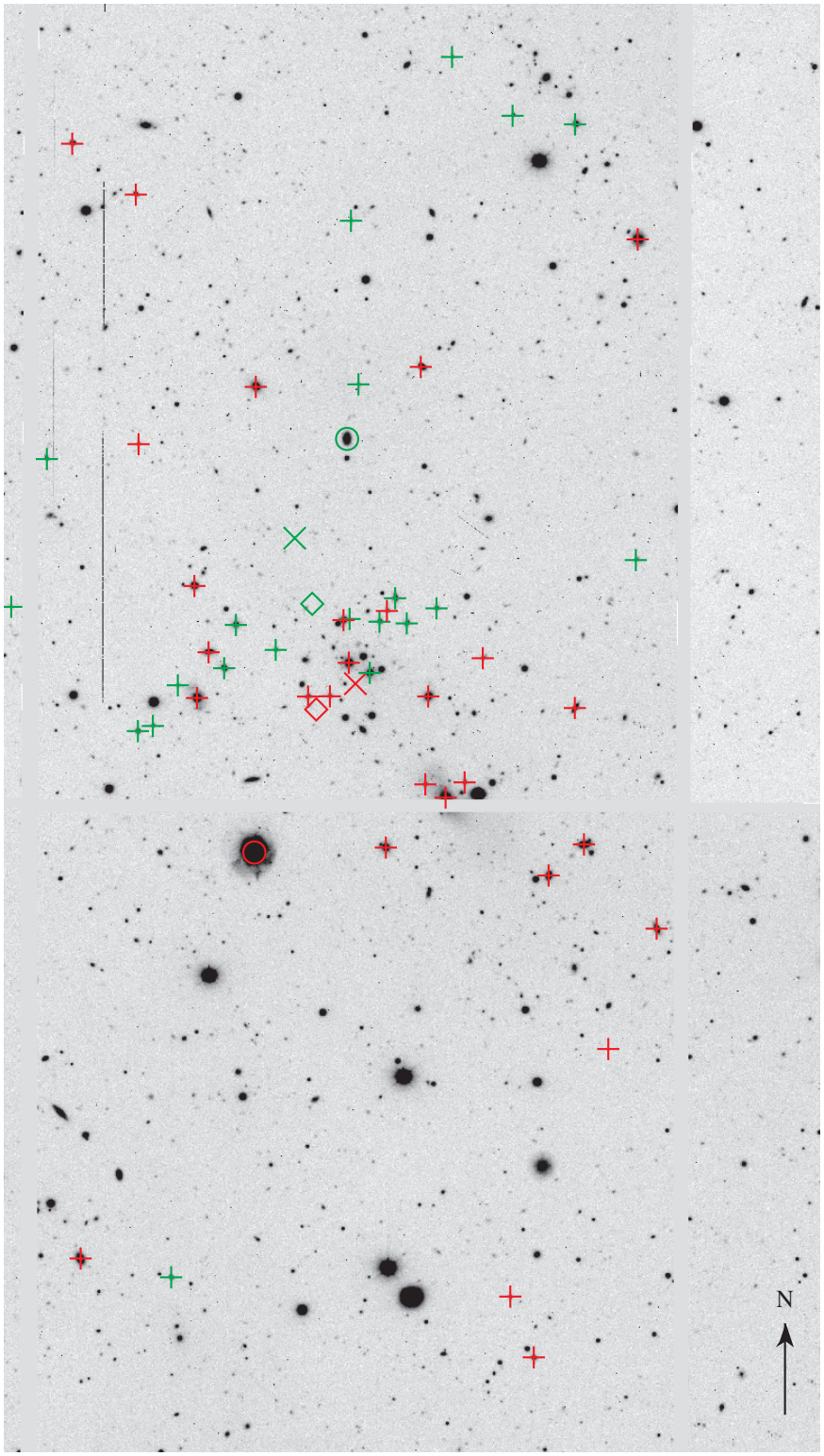

Figure 3.2, continued: clusters RCS J035139-0956.3A ($z_{spec} = 0.1678$, shown in red) and RCS J035139-0956.3B ($z_{spec} = 0.3054$, shown in green).

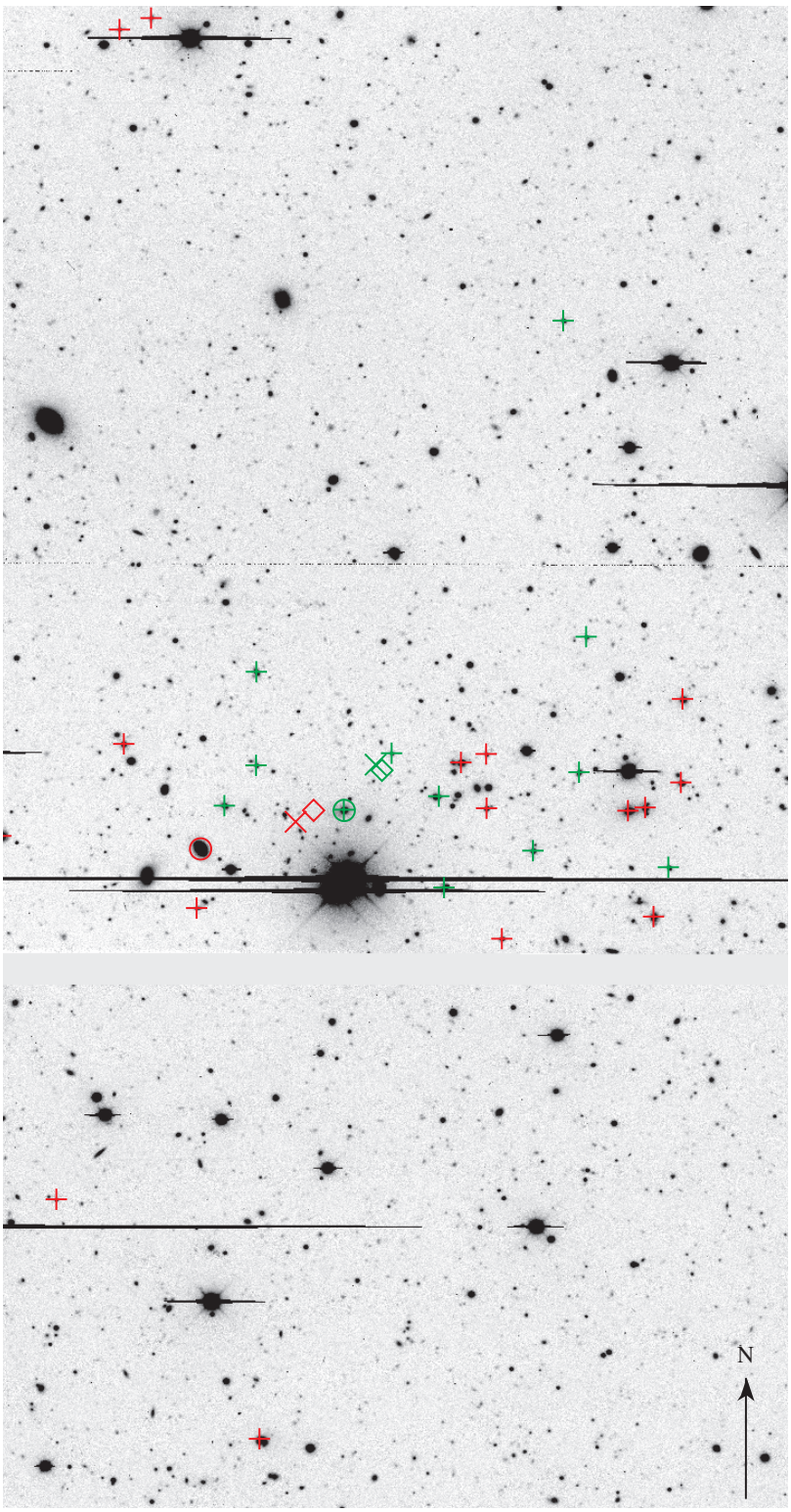

Figure 3.2, continued: clusters RCS J044207-2815.0A ($z_{spec} = 0.4108$, in red) and RCS J044207-2815.0B ($z_{spec} = 0.4663$, shown in green).

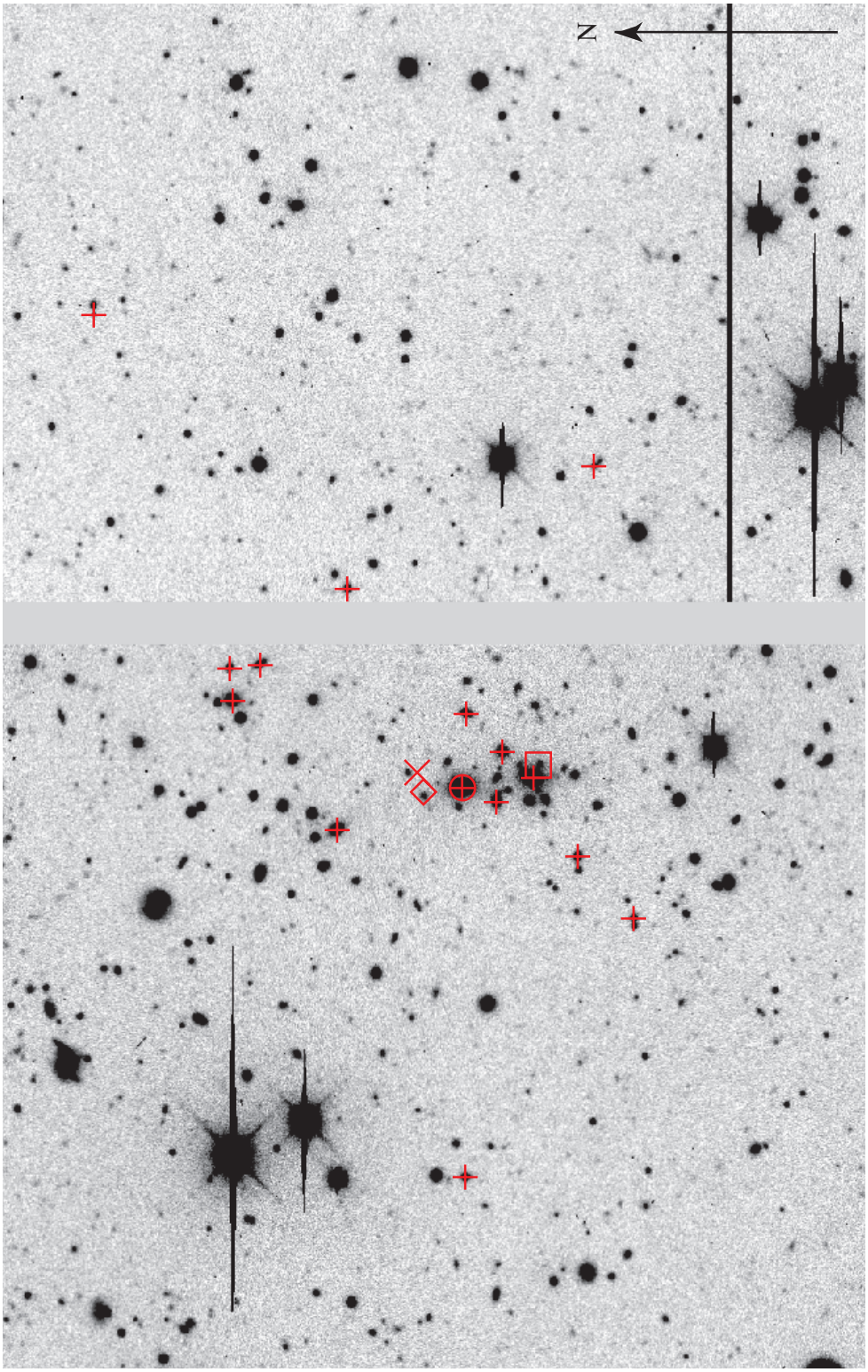

Figure 3.2, continued: cluster RCS J051536-4310.5 ($z_{spec} = 0.4245$).

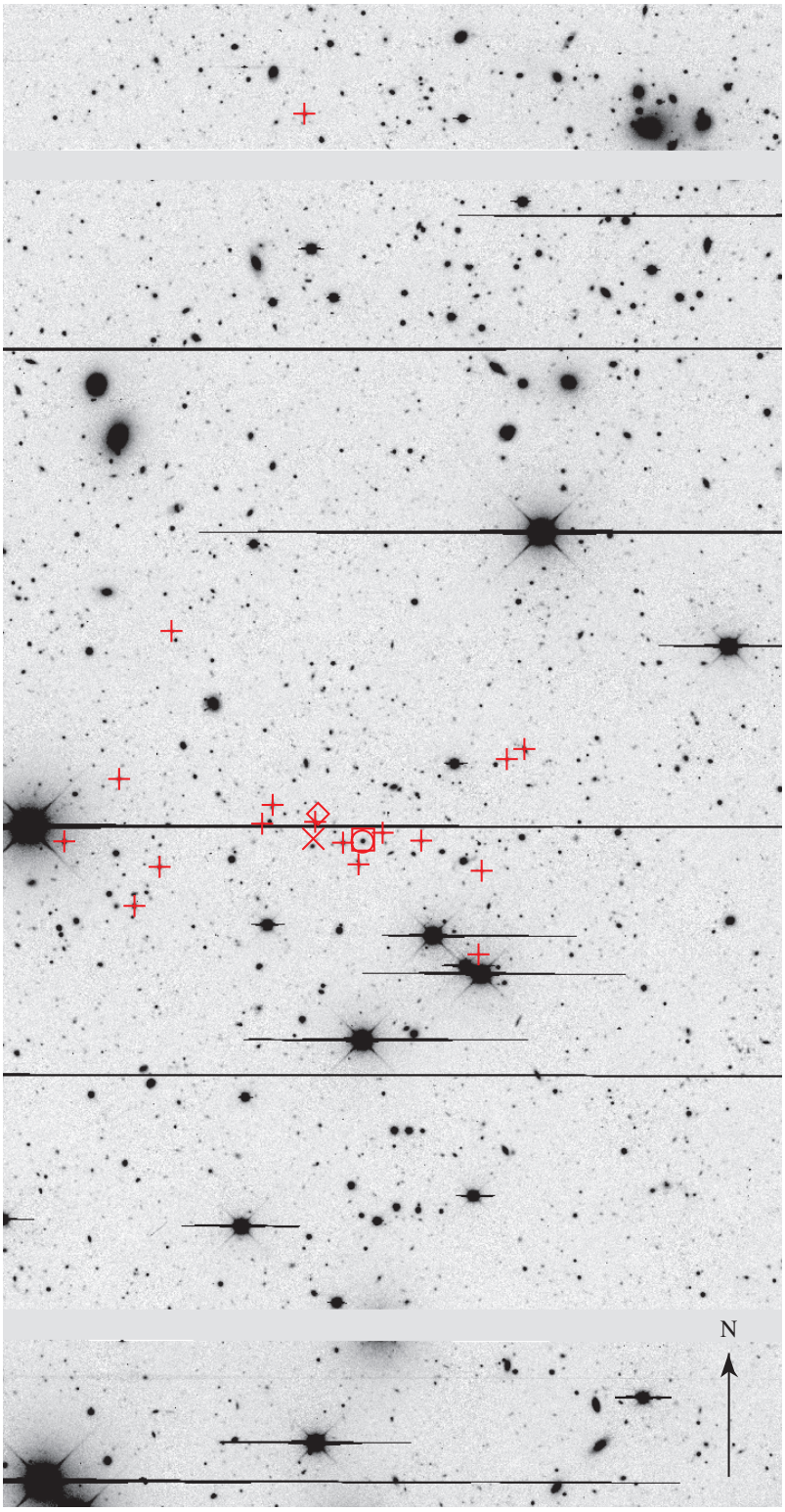

Figure 3.2, continued: cluster field RCS J051919-4247.8 ($z_{spec} = 0.5744$).

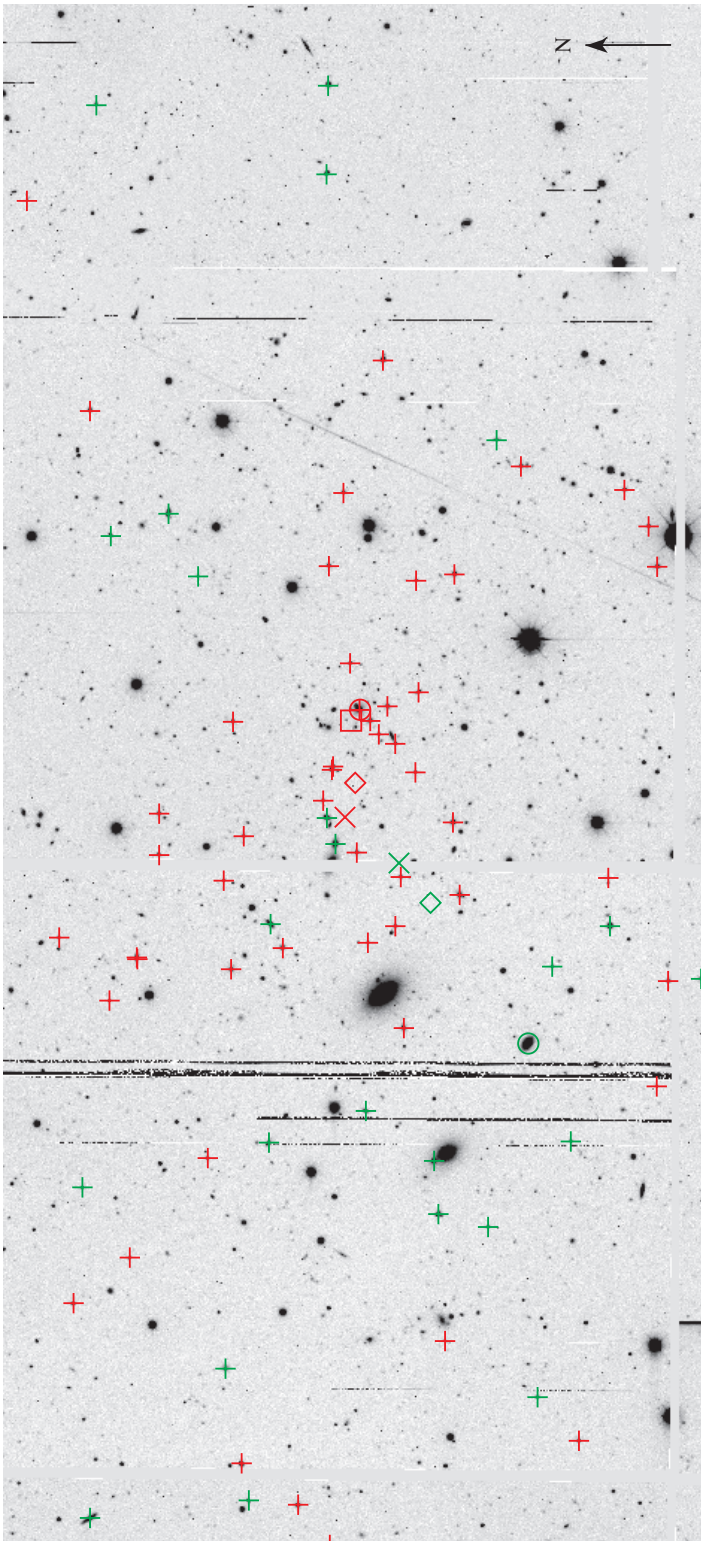

Figure 3.2, continued: cluster RCS J092821+3646.5 at $z_{spec} = 0.3926$ is shown in red, and RCS J092830+3646.0†($z_{spec} = 0.1402$) is green.

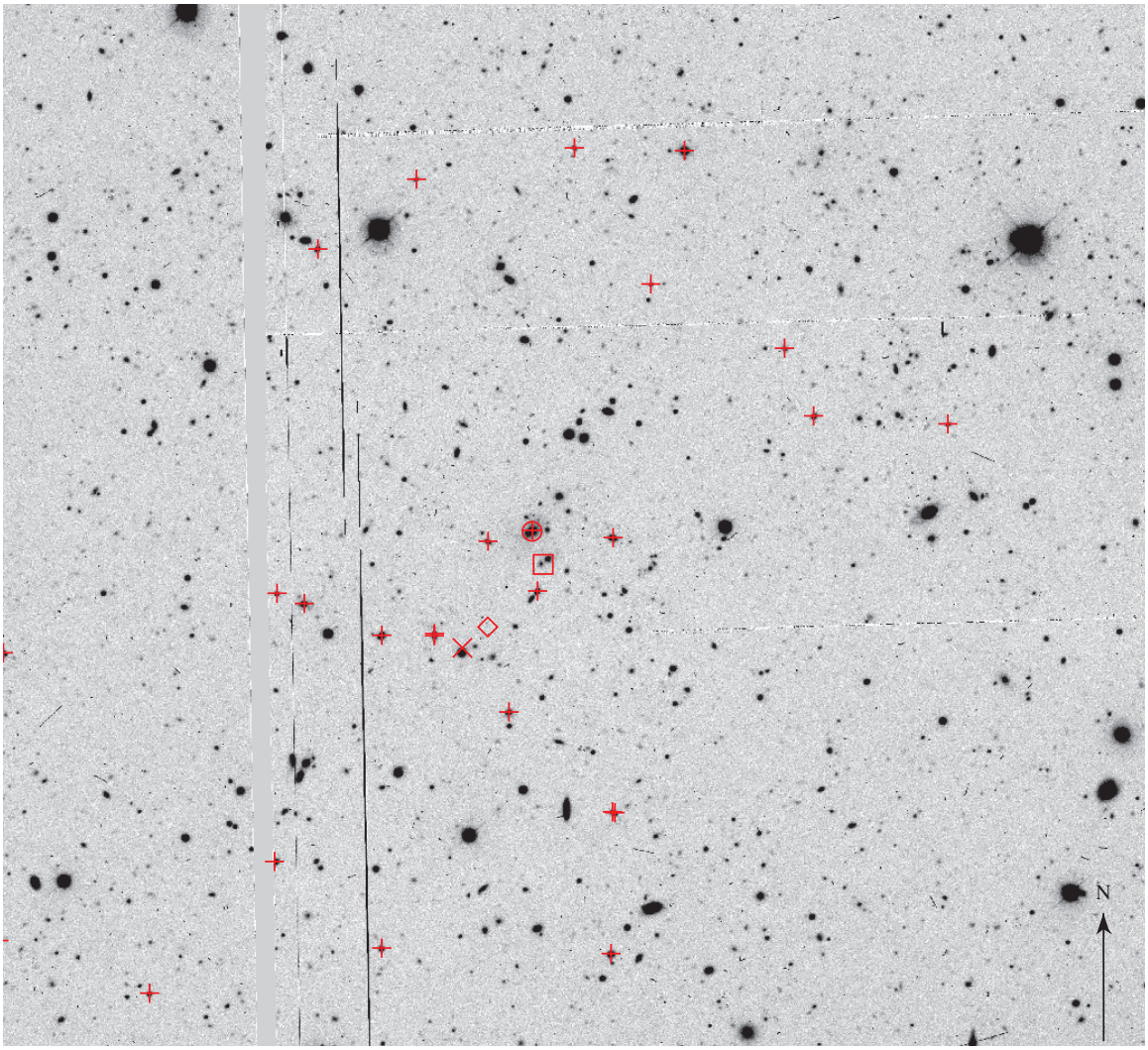

Figure 3.2, continued: cluster field RCS J093010+3841.2 ($z_{spec} = 0.4306$).

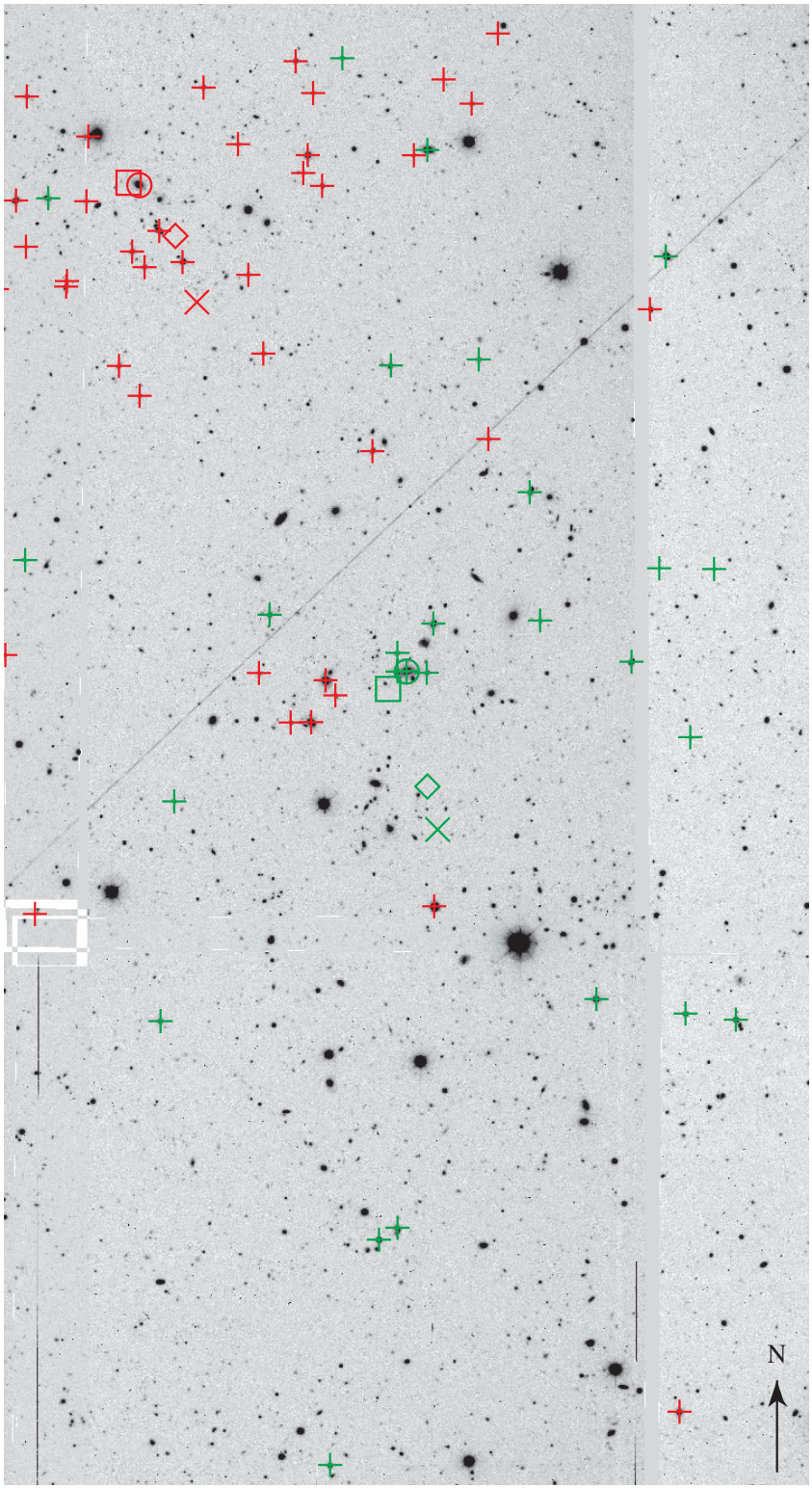

Figure 3.2, continued: cluster RCS J112051+1027.6 at $z_{spec} = 0.2621$ is shown in red, and RCS J112038+1022.1 at $z_{spec} = 0.3069$ is green.

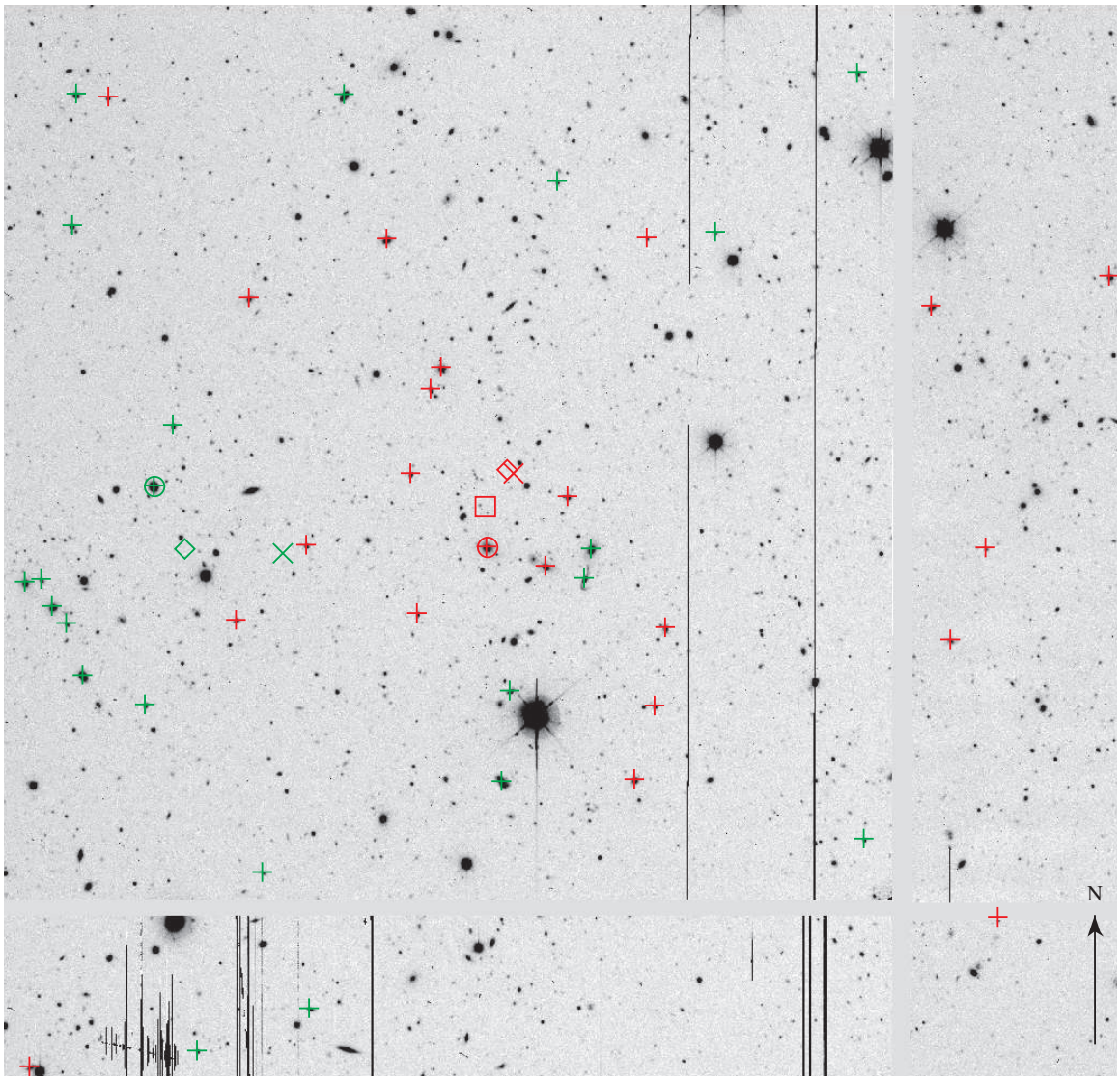

Figure 3.2, continued: cluster RCS J132523+2919.4A at $z_{spec} = 0.4291$ is shown in red, and RCS J131023+2919.4B ($z_{spec} = 0.2904$) is shown in green.

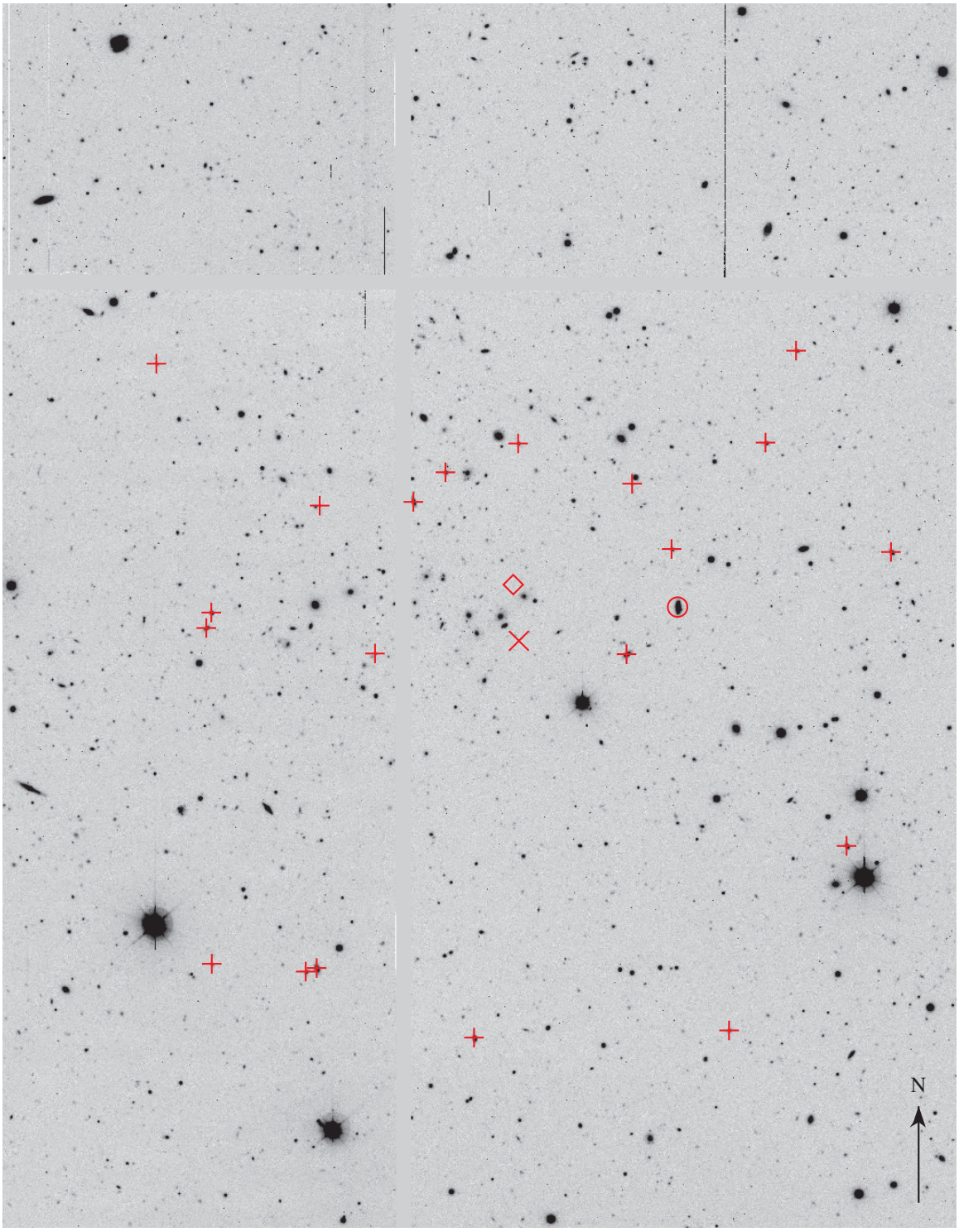

Figure 3.2, continued: cluster field RCS J133212+2847.5 ($z_{spec} = 0.2819$).

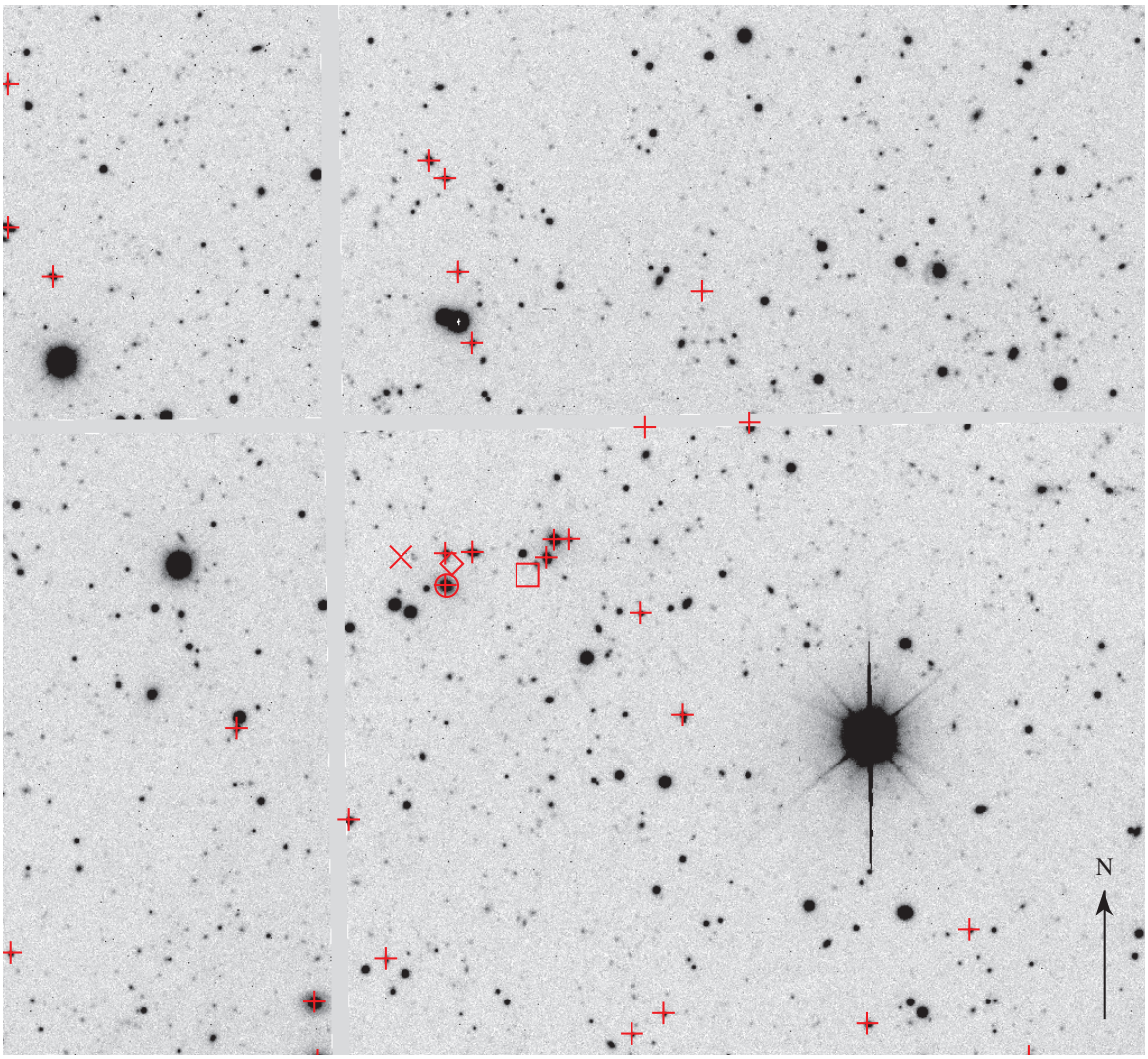

Figure 3.2, continued: cluster field RCS J144632+0859.2 ($z_{spec} = 0.2381$).

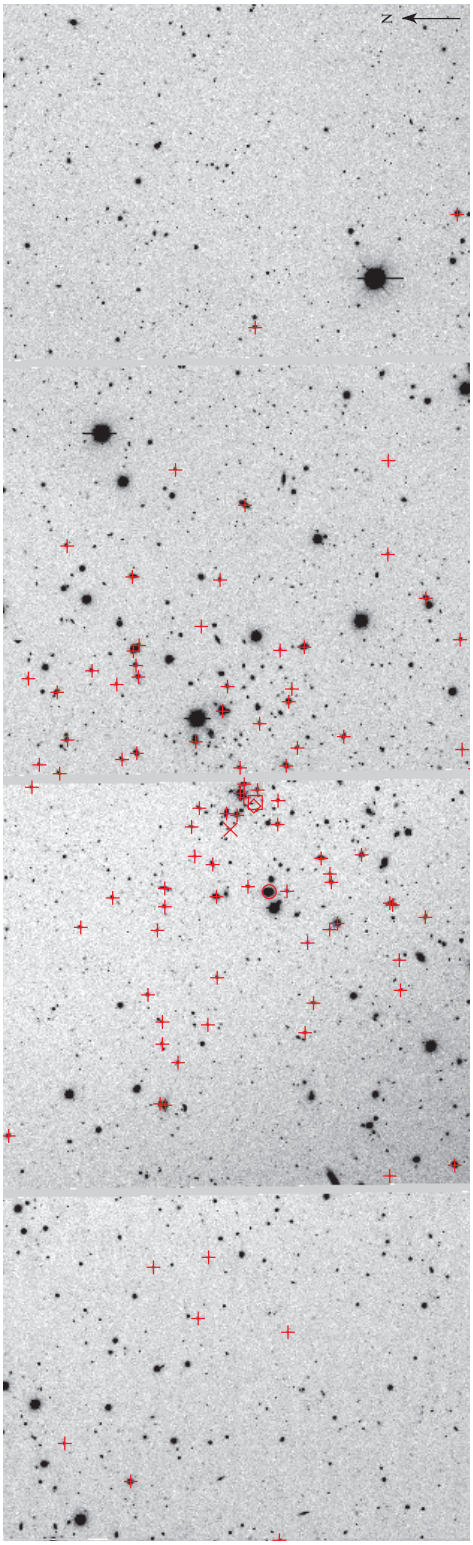

Figure 3.2, continued: cluster field RCS J144708+0949.0 ($z_{spec} = 0.2022$).

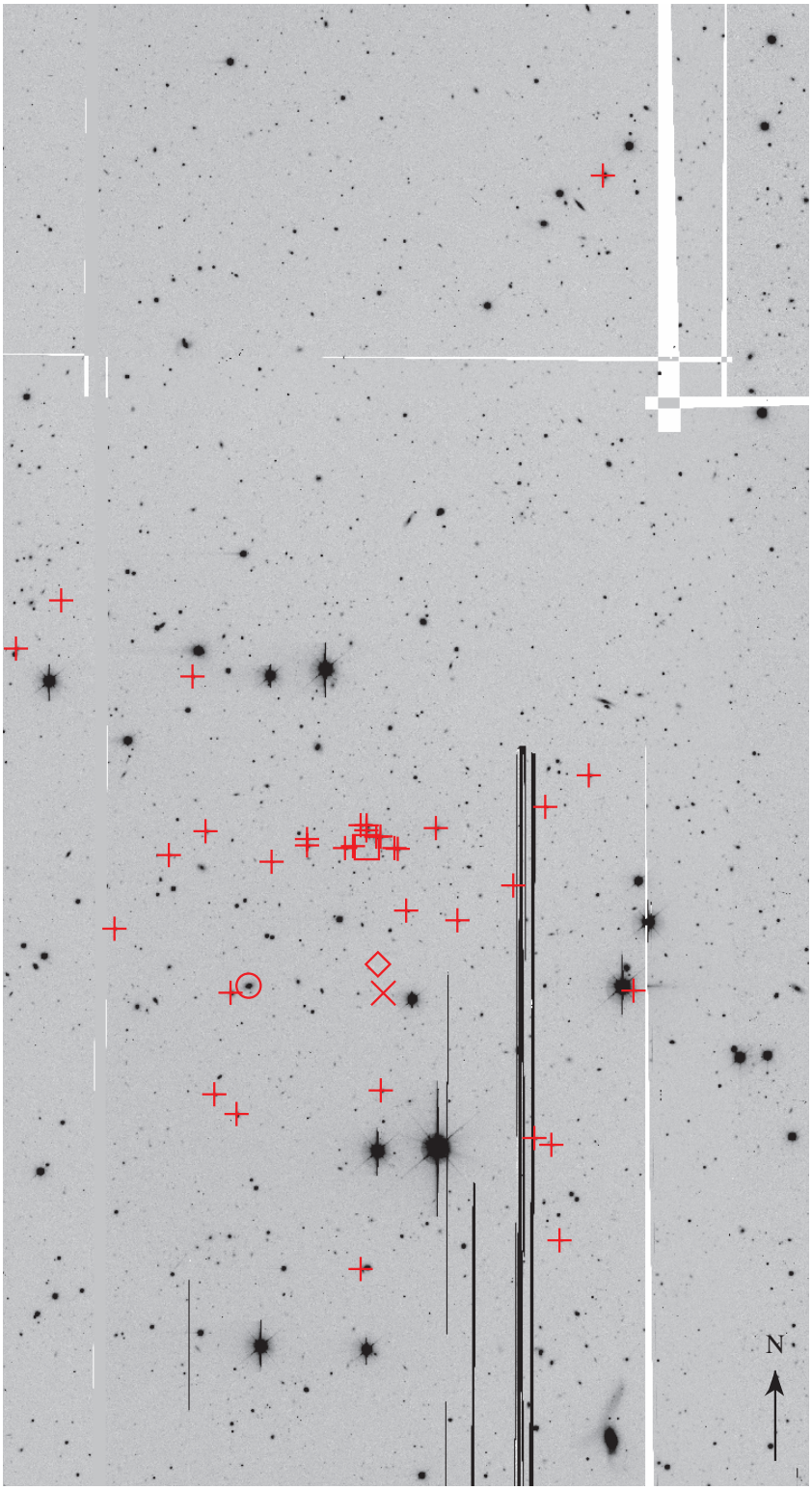

Figure 3.2, continued: cluster field RCS J161547+3057.3 ($z_{spec} = 0.4186$).

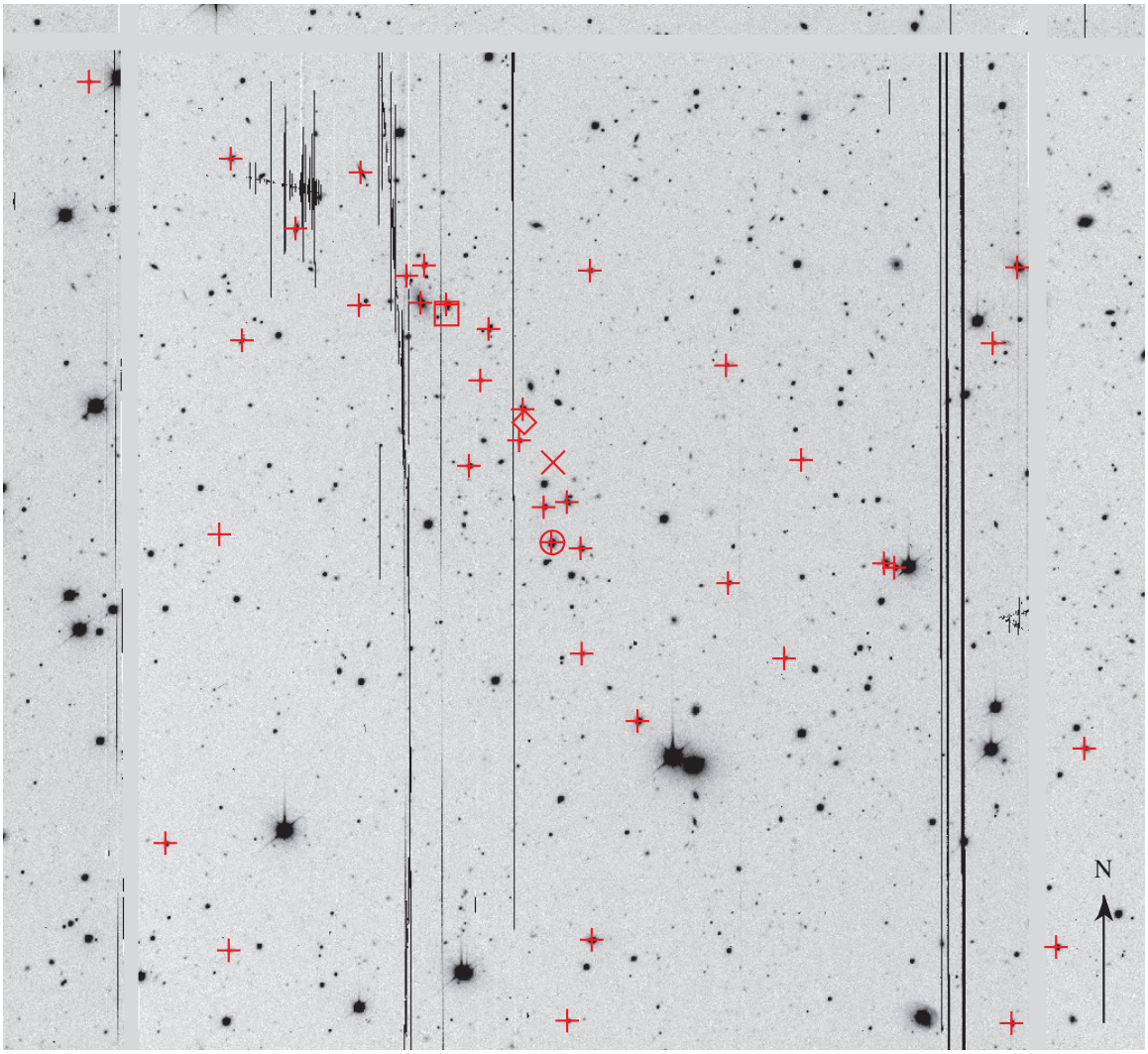

Figure 3.2, continued: cluster field RCS J162008+3046.7 ($z_{spec} = 0.2976$).

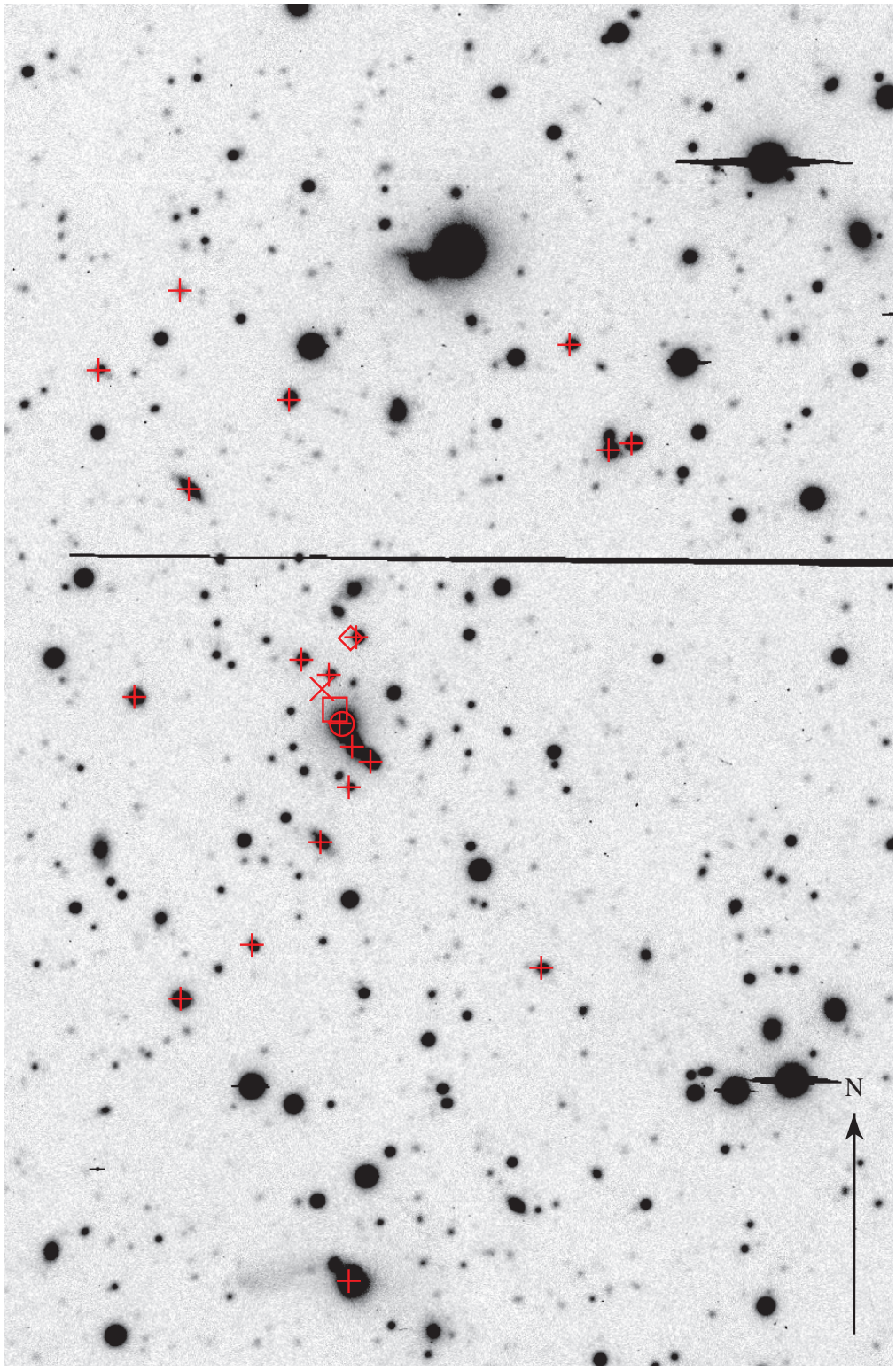

Figure 3.2, continued: cluster field RCS J211519-6309.5 ($z_{spec} = 0.2261$).

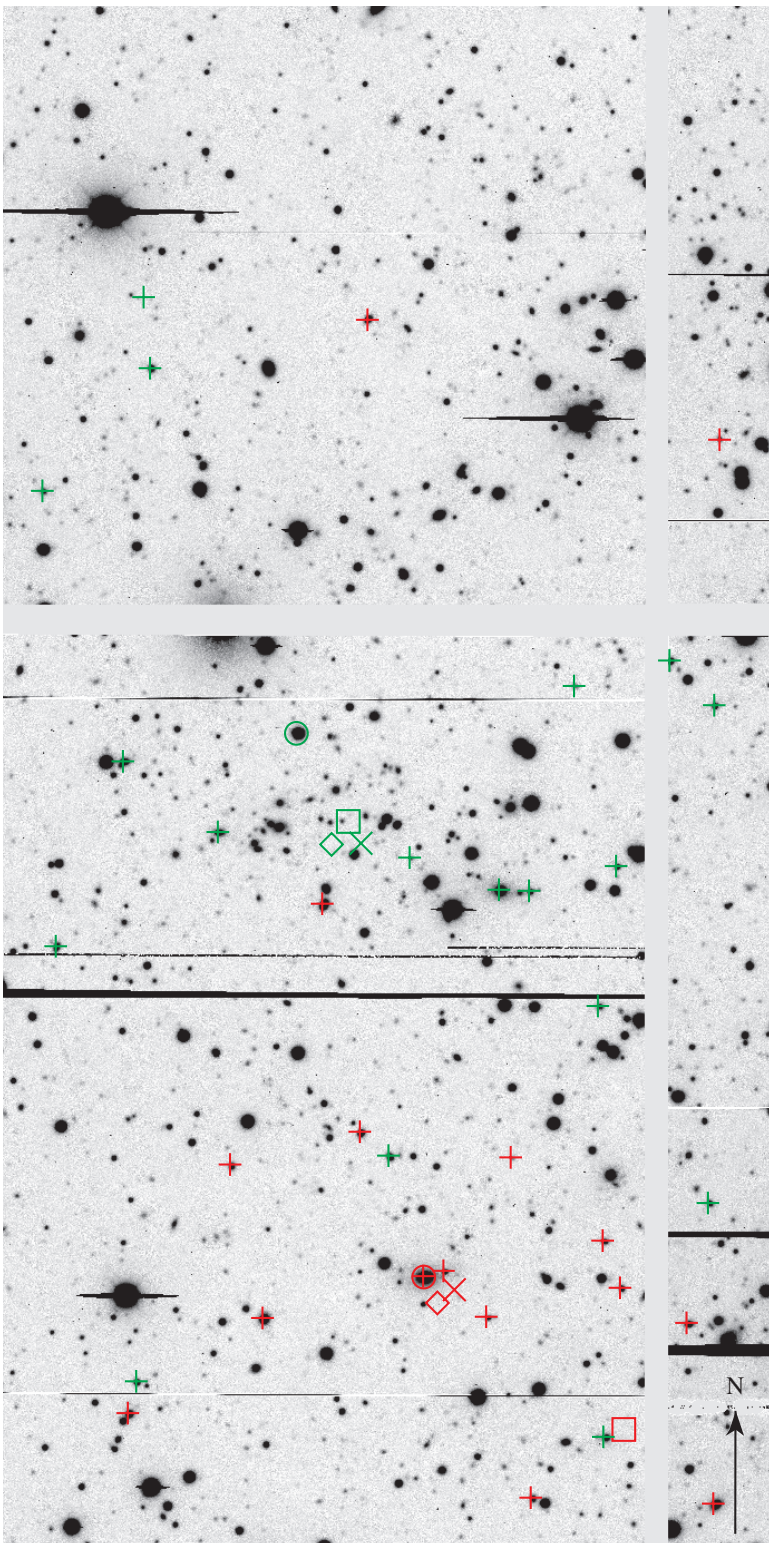

Figure 3.2, continued: cluster RCS J211945-6209.8 ($z_{spec} = 0.3108$) is in red, and RCS J212005-6204.8 ($z_{spec} = 0.3595$) is in green.

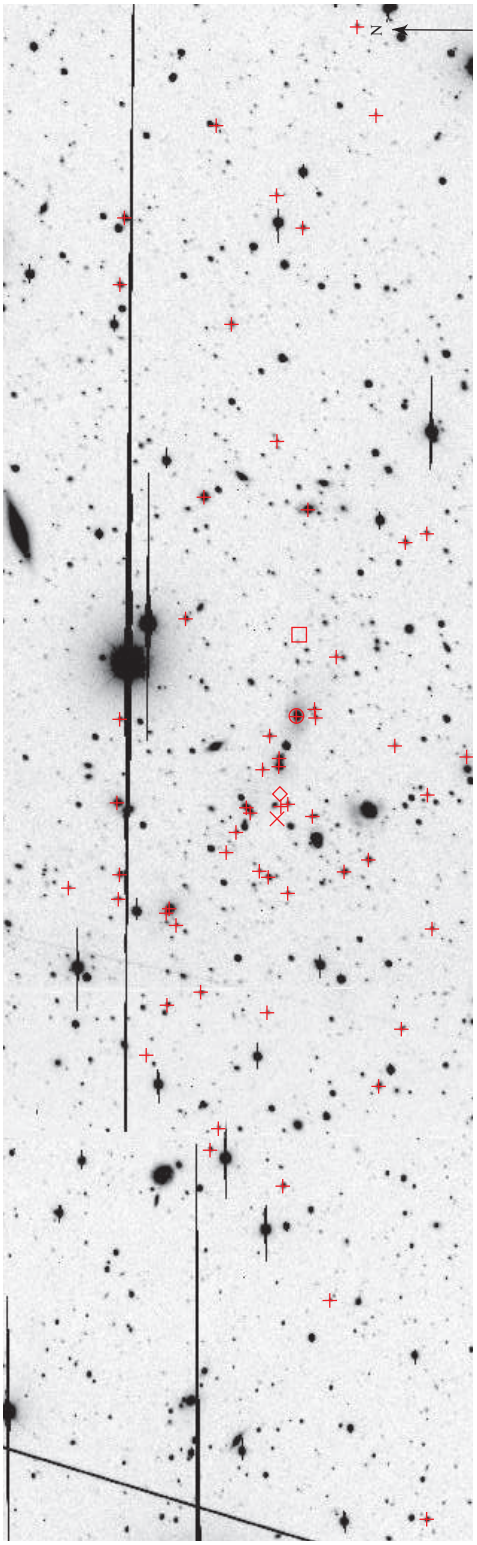

Figure 3.2, continued: cluster field RCS J212134-6335.8 ($z_{spec} = 0.2171$).

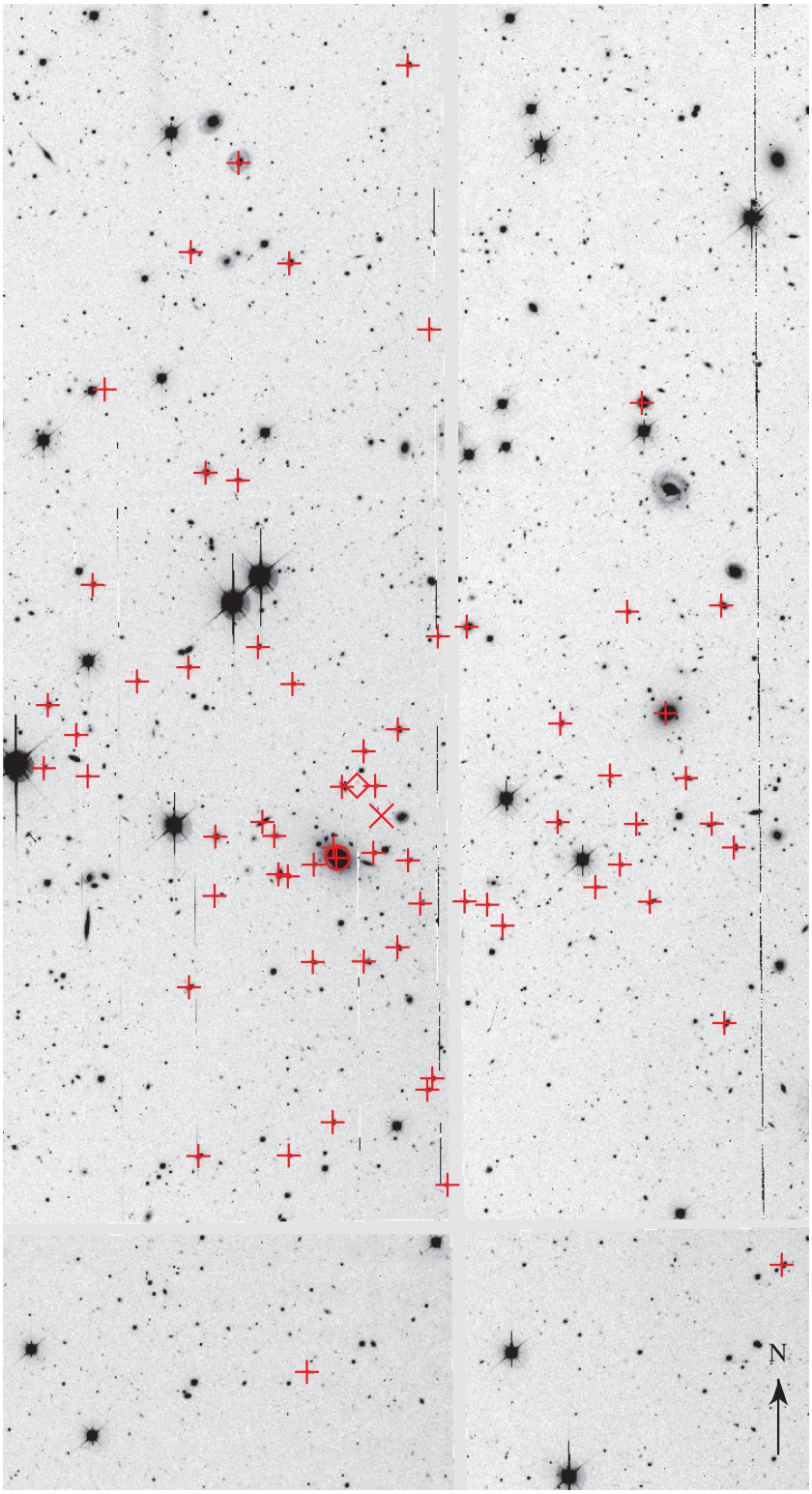

Figure 3.2, continued: cluster field RCS J215700-0441.9 ($z_{spec} = 0.1668$).

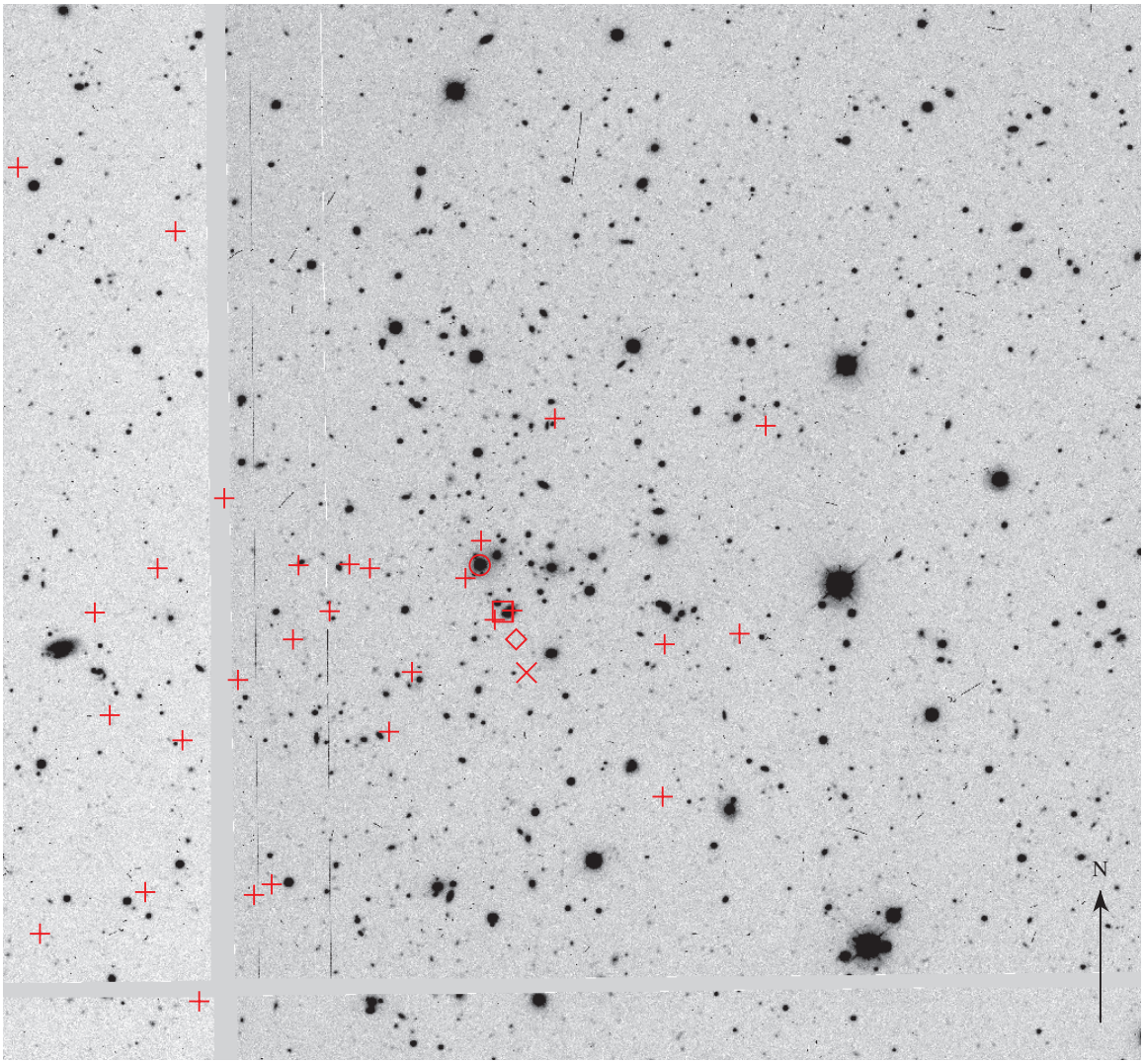

Figure 3.2, continued: cluster field RCS J231544+0052.8 ($z_{spec} = 0.3321$).

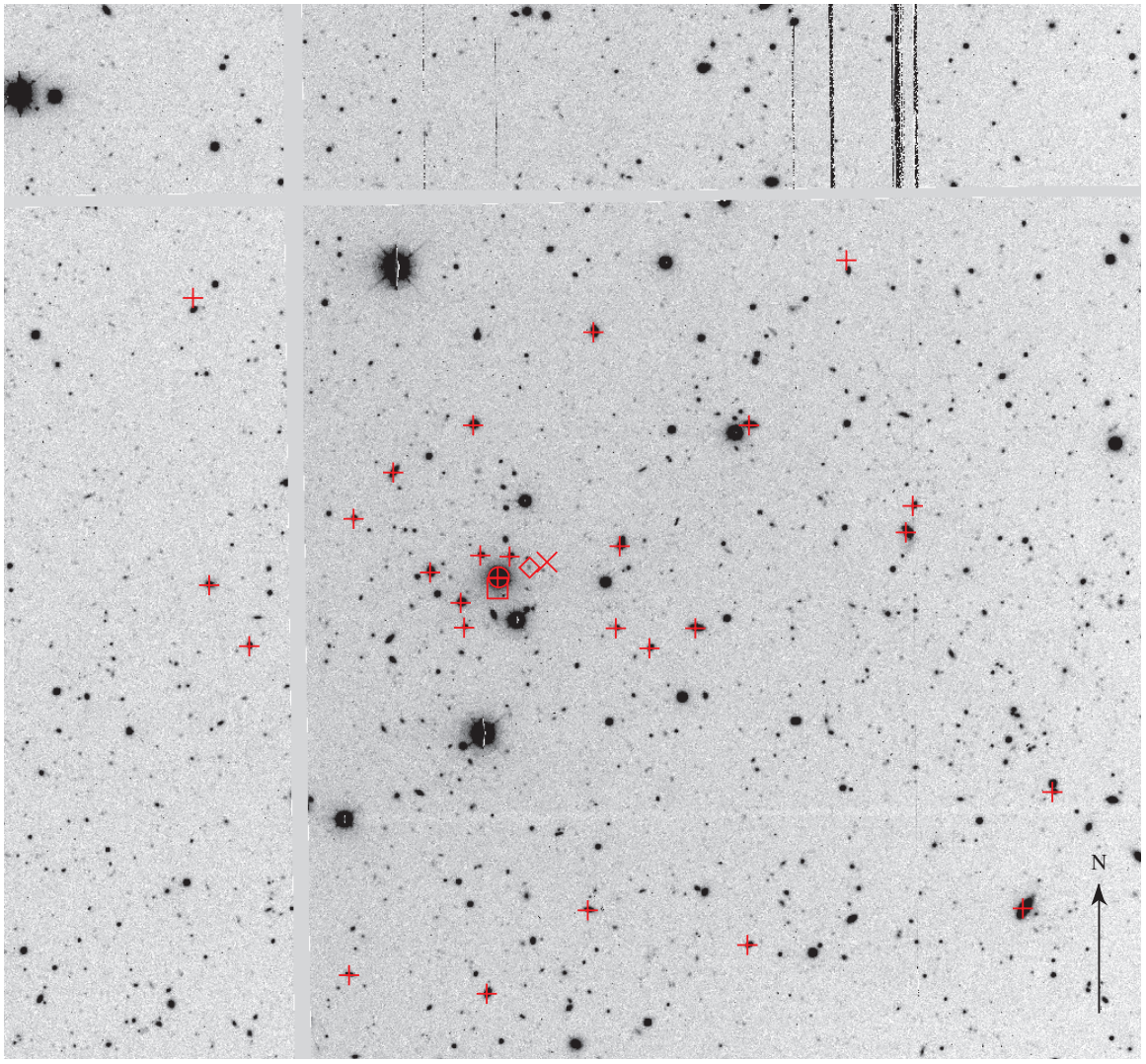

Figure 3.2, continued: cluster field RCS J231736-0103.0 ($z_{spec} = 0.2009$).

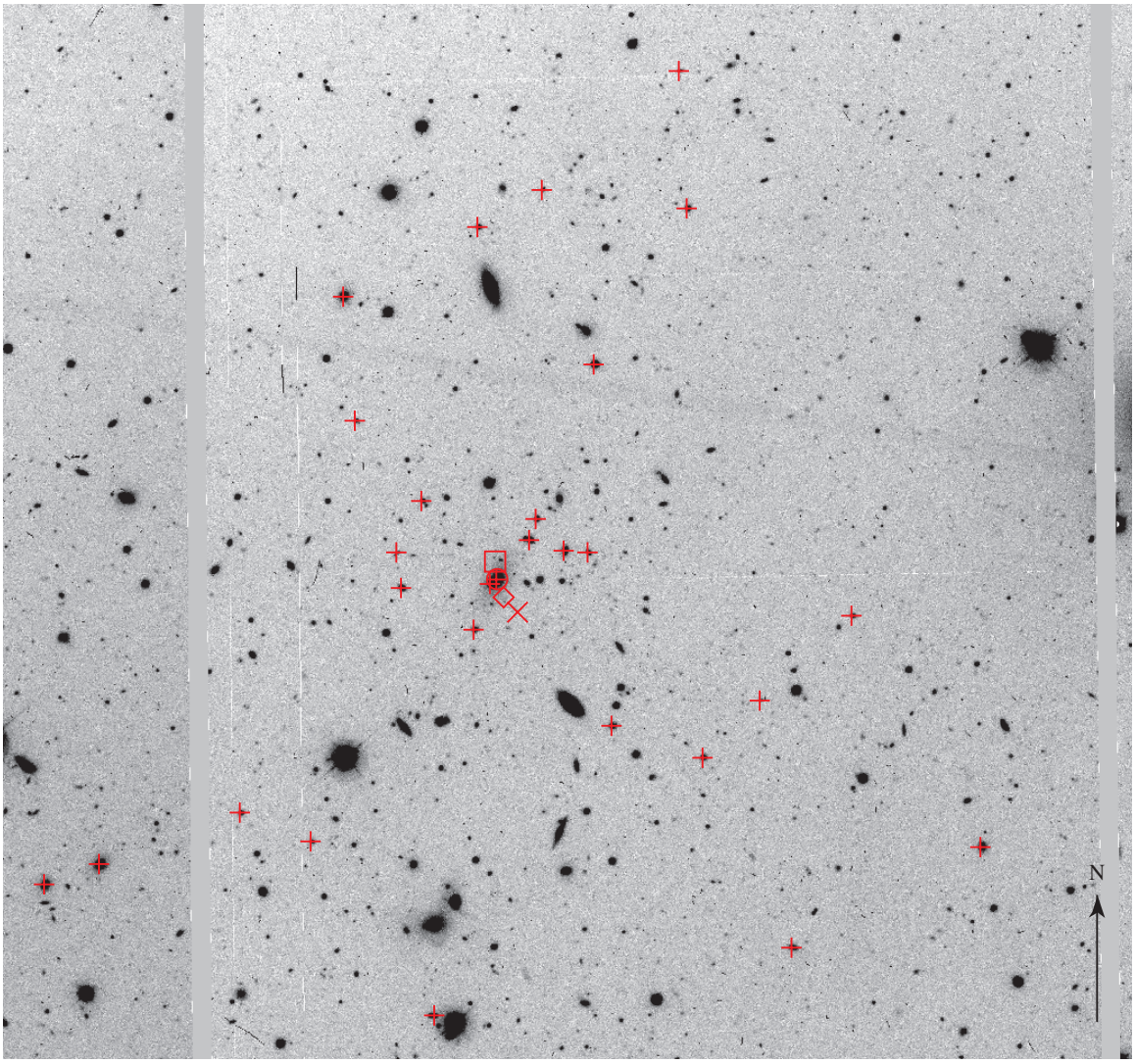

Figure 3.2, continued: cluster field RCS J231830-0024.5 ($z_{spec} = 0.3799$).

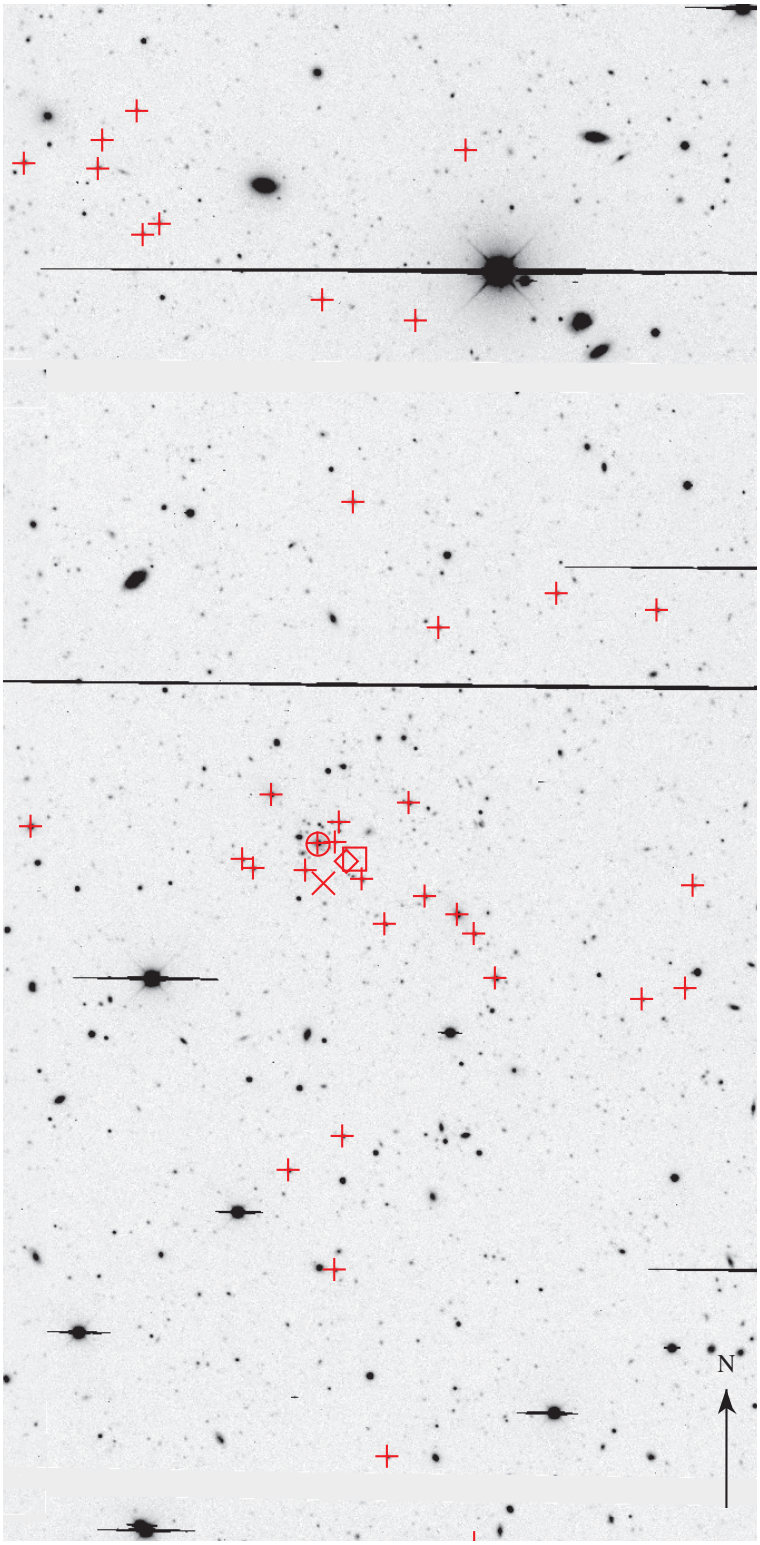

Figure 3.2, continued: cluster field RCS J234356-3517.5 ($z_{spec} = 0.4945$).

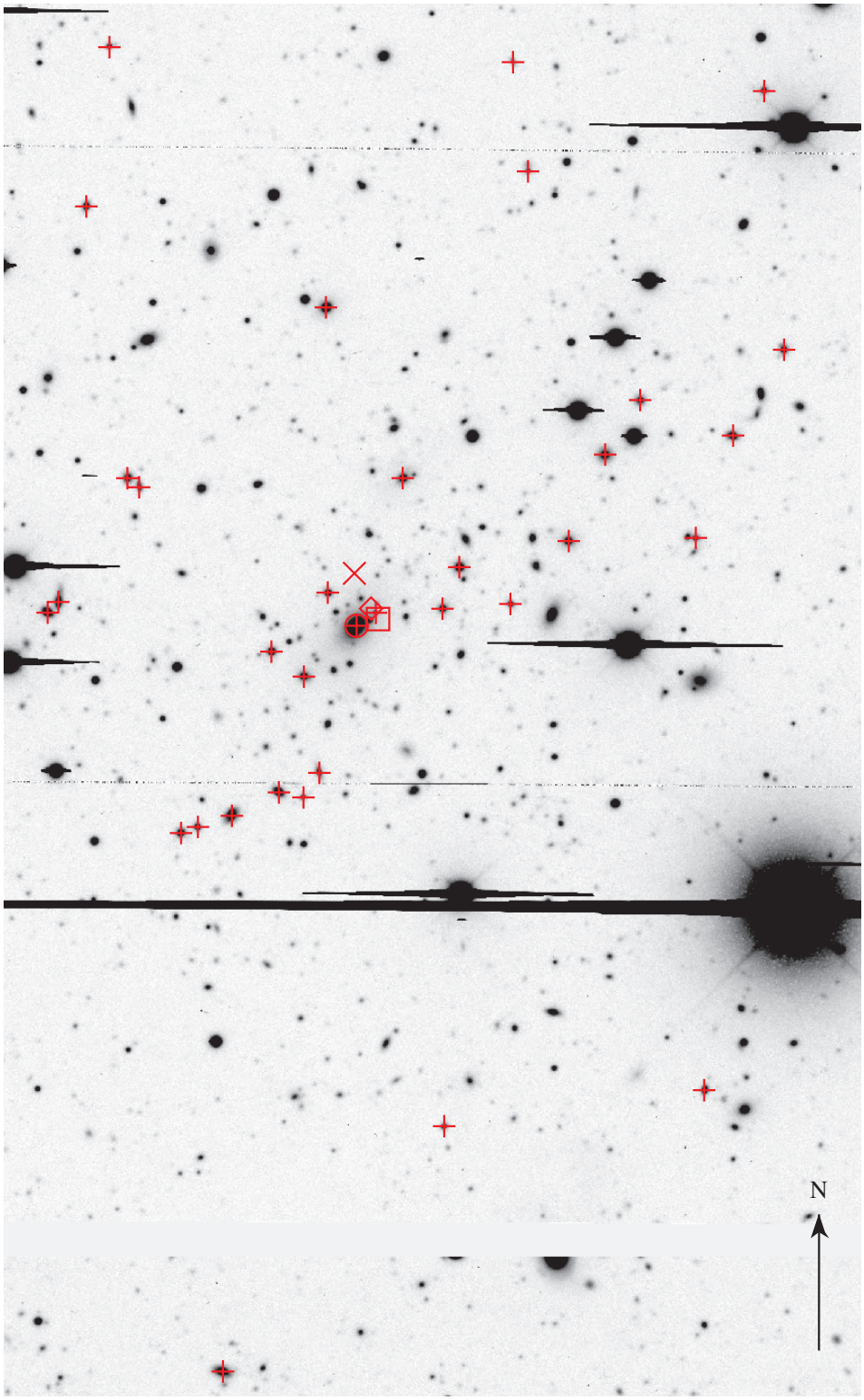

Figure 3.2, continued: cluster field RCS J234748-3535.1 ($z_{spec} = 0.2630$).

3.3 Dynamically-Derived Properties

Galaxy clusters are not isolated systems, but rather are simply the highest density peaks in the large scale structure of the universe. They have no sharp edges, and are superimposed upon a (relatively) smooth distribution of field galaxies. It is therefore difficult to define which galaxies belong to a cluster and which are interlopers. The lack of sharp edges also means that it is not trivial to determine the characteristic cluster scales in physical and velocity space, usually given by the virial radius and velocity dispersion. Moreover, the computation of these quantities depends on the cluster membership. We choose an iterative process, making initial guesses for the velocity dispersion σ and virial radius r_{vir} using a rough cut for cluster membership, using these guesses to properly assess cluster membership, and using the final set of members to produce accurate estimates of the velocity dispersion and virial radius.

3.3.1 Cluster Membership

To define the galaxy membership for each cluster we perform a rough velocity cut by excluding any galaxies separated by more than 4000km/s from the cluster redshift z_{clust}, and then pass this list of possible members to our interloper rejection scheme. Galaxy cluster-centric velocities are defined for each object i as $v_i = c(z_i - z_{clust})/(1 + z_{clust})$.

There are many possible techniques for determining cluster membership, from simple σ-clipping procedures or fixed-gap techniques such as the σ-gap technique of Zabludoff et al. (1990) to more sophisticated techniques utilizing both position and redshift information (see Fadda et al. 1996). We employ a modified version of the Fadda et al. (1996) shifting-gap procedure:

- Sort galaxies by increasing cluster-centric distance, and place in overlapping and shifting bins of radial size r_{gap}, or larger if necessary so that each bin contains at least n_{bin} galaxies.
- For each bin, apply a fixed-gap rejection scheme which sorts the galaxy velocities and removes all galaxies separated from their neighbours by more than v_{gap}. Iterate the fixed-gap scheme until the number of galaxies in each bin is stable.

Our technique differs from that of Fadda et al. (1996) only in our parameter choices. They use $n_{bin} = 15$, $r_{gap} = 0.4h^{-1}$Mpc, and $v_{gap} = 1000$km/s for a sample of nearby Abell clusters. We adjust these values to $n_{bin} = 10$, $r_{gap} = 0.5r_{vir}$ and $v_{gap} = \sigma$, using preliminary versions of r_{vir} and σ which were estimated using all galaxies within our rough velocity cut (the computation of σ and r_{vir} are described below). This adjustment accounts for the large richness range of our clusters. Example results of this scheme are shown in Figure 3.3.

As a test we have also employed the simpler scheme of Zabludoff et al. (1990), as well as the shifting-gap scheme using the Fadda et al. (1996) parameter choices, and achieved very similar

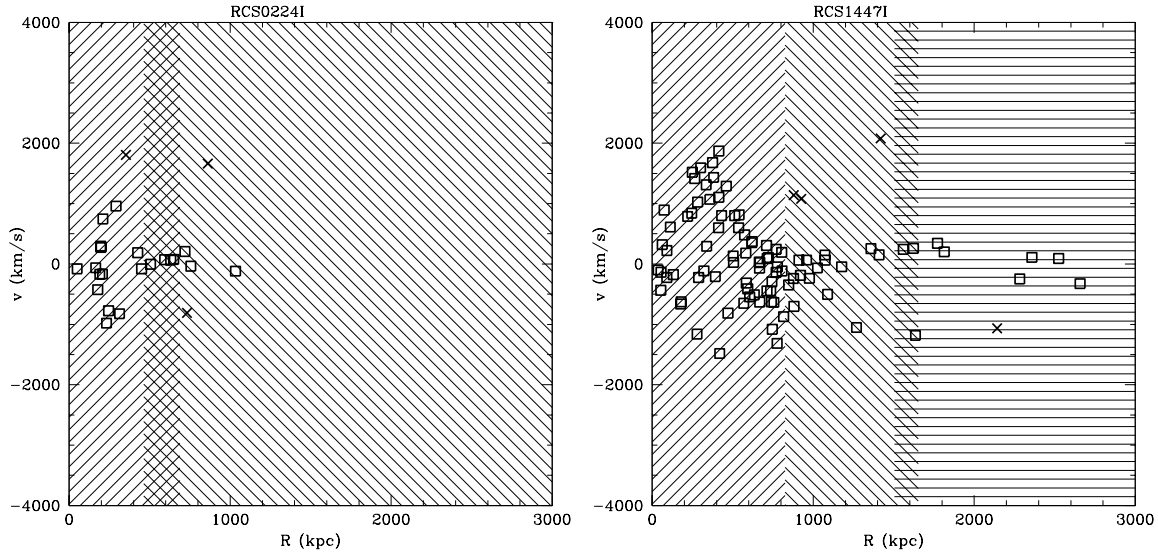

Figure 3.3 Example results from the shifting-gapper interloper rejection algorithm, showing velocity versus clustercentric radius. Open squares are cluster members, and x's are galaxies which were rejected as interlopers; hashed regions delimit the radial bins used by the algorithm. On the left is the moderate-richness cluster RCS J022402-0227.8, and on the right is RCS J144708+0949.9 which is our richest system.

results. The final number of members for each system is listed in column 5 of Table 3.2. Once membership is assigned for all systems, velocity dispersions and virial radii are re-computed as described below, using only the members. The cluster redshifts are also recomputed using only the members, but they do not change much (median $\delta v = 15$km/s).

3.3.2 Velocity Dispersions

Velocity dispersion is the basic estimate of velocity scale of a cluster, and is the most important ingredient for the calculation of virial mass. Often, this is computed simply as the standard deviation of the velocity distribution. However, the standard deviation is quite sensitive to outliers which may persist even after rejecting interlopers (and will certainly be present in the initial σ estimate used to set the gap size for our rejection algorithm). Therefore it is prudent to choose a more robust estimate for the cluster velocity scale. Beers et al. (1990) performed a detailed statistical study comparing scale estimators for various simulated datasets, and Girardi et al. (1993) applied these estimators to real data from 79 clusters; both studies favoured a composite estimate known as the "robust estimator" σ_{rob}. The robust estimator is either: the biweight estimator of scale σ_{biw} for datasets with at least 15 members, or the gapper estimator

σ_{gap} for smaller datasets. Both σ_{biw} and σ_{gap} are described in Beers et al. (1990); we present them briefly below:

- σ_{gap} uses the gaps in the ordered list of galaxy velocities:

$$\sigma_{gap} = \frac{\sqrt{\pi}}{n(n-1)} \sum_{i=1}^{n-1} w_i g_i \,, \tag{3.2}$$

  where $g_i = v_{i+1} - v_i$ are the velocity gaps between member galaxies, $w_i = i(n-i)$ are approximately Gaussian weights, and n is the number of galaxies.

- σ_{biw} uses the deviations of scaled velocities. The following calculation is performed iteratively until convergence:

$$\sigma_{biw} = \frac{\sqrt{n \sum_{|u_i|<1} v_i^2 (1-u_i^2)^4}}{\left| \sum_{|u_i|<1} (1-u_i^2)(1-5u_i^2) \right|} \,, \tag{3.3}$$

  where $u_i = v_i / 9S$ and S is the σ_{biw} estimate from the previous iteration (or the median absolute deviation for the first iteration).

For our clusters all estimators (simple Gaussian, gapper, and biweight) always agree within 1 standard deviation, and we use only the σ_{rob} values in this work. We also correct the velocity dispersions for redshift measurement errors using the formula of Danese et al. (1980). This formula should, in principle, be applied using the individual measurement error for each galaxy, but in our case the individual errors are unknown. We assume an error of 84km/s (as found from redundant observations in §2.4.2) for all galaxies. This is not strictly correct but should be sufficiently accurate for our purposes, since the total correction factors are only a few km/s (and always less than 5% of the velocity dispersion). The robust velocity dispersion estimates, along with their Jackknife errors, are given in column 6 of Table 3.2.

3.3.3 Virial Radii

Formally, the virial radius can be defined as the radius within which a system's energy is partitioned such that it obeys the virial theorem. However, this cannot in practice be calculated because the form of the potential is not known *a priori*. Instead the virial radius is usually calculated using the mean projected separation of galaxies in the cluster (for example Rood & Dickel 1979; Barnes 1983; Diaferio et al. 1993; Carlberg et al. 1996; Eke et al. 2004). Carlberg et al. (1996, hereafter C96) used the following definition (equation 2):

$$R_{vir}^{-1} = \left(\sum_i w_i \right)^{-2} \sum_{i<j} \frac{w_i w_j}{|R_i - R_j|} \,, \tag{3.4}$$

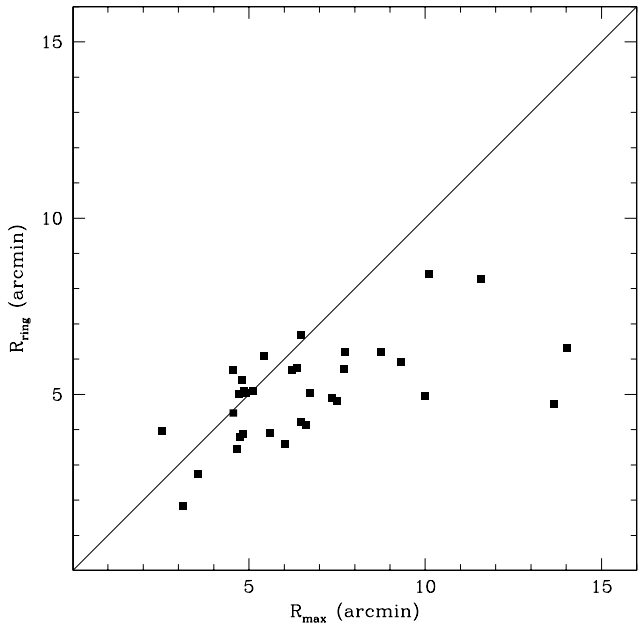

Figure 3.4 Ring estimates of the cluster virial radii R_{ring}, versus available field size R_{max}. Equality is shown as a solid line; note that R_{ring} exceeds the available field size for a substantial fraction of the clusters.

where R_i are the projected clustercentric radii of the member galaxies, and w_i are the empirical weights discussed in §2.5. They noted that simple harmonic estimates such as this are problematic when the observations are enclosed by a rectangular window, and introduced an alternate "ringwise" estimate (equation 3 in C96):

$$R_{ring}^{-1} = \left(\sum_i w_i \right)^{-2} \sum_{i<j} w_i w_j \frac{2}{\pi(r_i + r_j)} K(k_{ij}) \, , \tag{3.5}$$

where $k_i j^2 = 2\sqrt{r_i r_j}/(r_i + r_j)$ and $K(k)$ is the complete elliptic integral of the first kind.

We have implemented this formula for our clusters, but find the resulting R_{ring} to be unreliable: as illustrated in Figure 3.4 the virial radii are somewhat correlated with the available field size, and in some cases the virial radii even exceed the field size. Therefore, we use another way to determine r_{vir}. Following Carlberg et al. (1997), we adopt a dynamical estimate of virial radius, defined as the radius within which the mean interior density (as estimated from the virial mass) is 200 times the critical density:

$$r_{200} = \frac{\sqrt{3}\sigma}{10H(z)} \, , \tag{3.6}$$

where $H(z)$ is the Hubble constant at the redshift of the cluster, and the density is assumed to be of the form $\rho(r) \propto 1/r^2$. This estimate is not ideal, since the measured physical and

velocity scales of the cluster are no longer independent. However, it appears that much larger field sizes would be required in our spectroscopic survey to avoid this. Also, recent work by Biviano et al. (2006) suggests that cluster masses estimated from velocity dispersions alone (i.e., without independent r_{vir} measurements) may in general be more reliable, especially for systems with relatively few members such as the clusters in our survey. The r_{200} estimates are given in column 7 of Table 3.2, along with their Jackknife errors.

3.3.4 Masses

We estimate cluster masses simply using the virial theorem. We insert our robust velocity dispersions and dynamical virial radii into the following equation:

$$M_{200} = \frac{3}{G}\sigma^2 r_{200} \ . \tag{3.7}$$

The cluster M_{200} values, and their Jackknife errors, are presented in column 8 of Table 3.2. As explained in C96, this equation will in fact overestimate the true cluster mass. It should be corrected by a "surface pressure" term of $4\pi\rho\sigma_r^2 r_b^3$ which compensate for the finite boundary r_b within which the mass is computed. Unfortunately, the amount of this correction depends on the form of the mass profile, which is not known *a priori*; in fact, its determination is one of the main goals of this thesis. Here we simply note that this correction should be smaller than 50% (calculated by C96 for the simple but somewhat extreme case of a singular isothermal sphere).

3.3.5 Luminosities

Cluster luminosities are computed as a weighted sum of the R_c-band luminosities of cluster members within r_{200}:

$$L_{Rc,200} = \sum_i w_i \ W_{ring}(R_i) \ l_i \ , \tag{3.8}$$

where the sum is over all member galaxies within r_{200} which are above our fiducial magnitude limit of $M^* + 2$. The w_i are the empirical weights as described in §2.5. Following Yee et al. (1996b), we also implement an additional weight to compensate for the rectangular shape of the spectroscopic field: $W_{ring}(R_i)$ is the ratio of the area of an annulus at radius R_i divided by the area of the portion of that annulus covered by our field (see Figure 3.5). The l_i are rest R_c-band luminosities of the galaxies. We convert from apparent magnitude with K-corrections using template galaxy spectra from Coleman et al. (1980), convolved with the filter response and quantum efficiency curves. The template spectrum is chosen based on our Scl spectral type (see §2.5). We also perform an evolutionary correction to the mean redshift of our cluster sample ($<z>= 0.338$), using the values tabulated by Poggianti (2004).

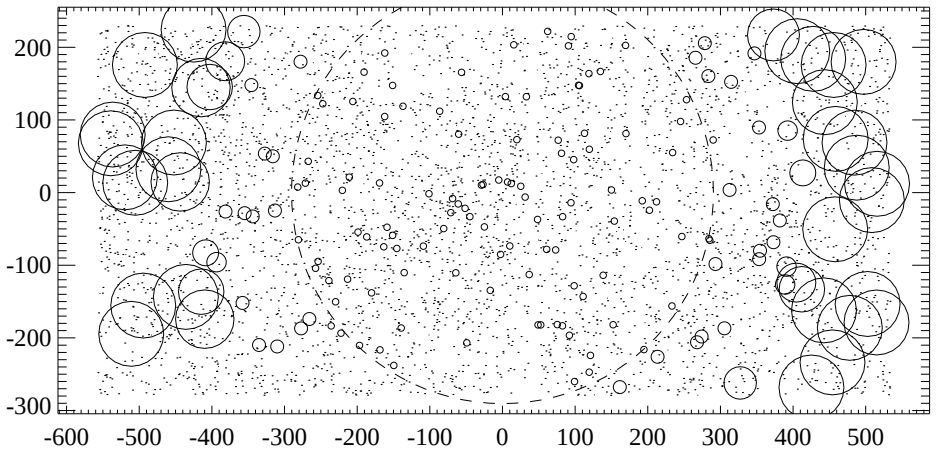

Figure 3.5 Example of ring weights: the field of cluster RCS J092821+3646.5 (RA and Dec in arcminutes). Each galaxy from the photometric catalog is shown as a dot. Circles denote galaxies with measured redshifts, where the size of the circle is proportional to the galaxy's weight $W_{ring}(R_i)$. The virial radius r_{200} is marked as a dashed circle.

We apply a faint-end correction to the cluster luminosities, correcting from our limit of $M^* + 2$ down to zero luminosity. To do this, we must assume a form of the luminosity function. As in §2.5 we choose the Schechter function of low redshift Abell clusters from Yee & López-Cruz (1999): $M^* = -22.2 - 1.4z$ and faint-end slope $\alpha = -1$. Although we are implicitly assuming that the cluster luminosity function is universal, the correction is quite small ($\sim 10\%$) so that small differences in the form of the luminosity function would not significantly affect our luminosities. Finally, we convert the $L_{Rc,200}$ values to solar units, using $M_{Rc}(\odot) = 4.39$. Cluster luminosities along with Jackknife errors are given in column 9 of Table 3.2.

3.3.6 The effect of centre choice

As discussed in §3.2, we computed four estimates of cluster centre. The results above were calculated using the centroid estimate computed from spectroscopic members only: $(\mathrm{RA,Dec})_{spec}$. In Figure 3.6 we compare them to results computed using the other centroid estimates. We find that the choice of centre makes very little difference to the cluster velocity dispersion (em cf., Girardi et al. 1996); this is not surprising, because cluster velocity dispersions vary only slowly with radius. Consequently the cluster masses agree very well. The cluster luminosities depend more strongly on cluster centre, primarily because of the weights we employ to account for incompleteness: a shift in centroid could include (or exclude) objects with fairly high geometric weights, which can significantly boost (or dampen) the total measured luminosity within r_{200}.

Table 3.2. Global properties of the clusters

Cluster Name	z_{phot}	B_{gcR}	z_{spec}	N_{mem}	σ (km/s)	r_{200} (kpc)	M_{200} ($10^{14} M_\odot$)	$L_{Rc,200}$ ($10^{11} L_\odot$)
RCS J022240 + 0144.5	0.258	585 ± 184	0.2460	35	762 ± 113	1685 ± 250	6.83 ± 2.93	15.88 ± 5.60
RCS J022331 + 0118.4	0.481	350 ± 161	0.4403	22	372 ± 89	767 ± 129	0.79 ± 0.38	13.30 ± 4.77
RCS J022402 − 0227.8	0.395	758 ± 206	0.3295	21	455 ± 102	928 ± 211	1.24 ± 0.82	8.09 ± 2.17
RCS J022516 + 0011.5	0.410	975 ± 226	0.3576	30	525 ± 96	1150 ± 182	2.44 ± 1.15	12.35 ± 3.89
RCS J033414 − 2824.6	0.683	1270 ± 306	0.6642	70	240 ± 31	663 ± 69	0.68 ± 0.21	31.30 ± 7.47
RCS J035139 − 0956.3A*	···	454 ± 172	0.1678	27	391 ± 68	826 ± 126	0.75 ± 0.34	6.06 ± 1.85
RCS J035139 − 0956.3B*	···	248 ± 152	0.3054	20	579 ± 114	1165 ± 234	2.40 ± 1.55	6.64 ± 2.70
RCS J044207 − 2815.0A*	···	538 ± 192	0.4108	17	719 ± 162	1362 ± 222	4.29 ± 1.98	12.06 ± 4.21
RCS J044207 − 2815.0B*	···	720 ± 187	0.4663	11	663 ± 94	1200 ± 205	3.11 ± 1.53	10.23 ± 3.76
RCS J051536 − 4325.5	0.400	1002 ± 228	0.4245	15	653 ± 194	1315 ± 390	3.92 ± 5.43	16.67 ± 6.66
RCS J051919 − 4247.8	0.606	522 ± 184	0.5744	17	172 ± 155	466 ± 86	0.21 ± 0.11	5.11 ± 2.32
RCS J092821 + 3646.5	0.426	1385 ± 259	0.3926	50	842 ± 88	1592 ± 145	6.72 ± 1.80	25.94 ± 5.21
RCS J092830 + 3646.0†*	···	94 ± 120	0.1402	23	393 ± 99	895 ± 209	0.92 ± 0.70	0.76 ± 0.39
RCS J093010 + 3841.2	0.518	409 ± 168	0.4306	26	587 ± 114	1107 ± 183	2.35 ± 1.10	11.00 ± 3.68
RCS J112038 + 2522.1	0.329	456 ± 173	0.3069	16	236 ± 199	684 ± 221	0.48 ± 0.38	5.19 ± 2.53
RCS J112051 + 2527.6	0.246	509 ± 176	0.2621	35	345 ± 80	689 ± 121	0.48 ± 0.27	4.71 ± 1.47
RCS J132523 + 2919.4A	0.410	436 ± 174	0.4291	21	439 ± 144	1141 ± 241	2.57 ± 1.48	7.22 ± 2.61
RCS J132523 + 2919.4B*	···	12 ± 115	0.2904	23	865 ± 164	1869 ± 354	9.76 ± 5.22	4.25 ± 1.54
RCS J133212 + 2847.5*	···	-21 ± 113	0.2819	18	199 ± 125	602 ± 142	0.32 ± 0.24	0.70 ± 0.51
RCS J144632 + 0859.2	0.246	251 ± 149	0.2381	28	692 ± 150	1536 ± 333	5.14 ± 3.34	8.75 ± 2.74
RCS J144708 + 0949.0	0.168	1333 ± 246	0.2022	90	709 ± 61	1536 ± 134	4.96 ± 1.28	20.52 ± 3.43
RCS J161547 + 3057.3	0.454	1132 ± 226	0.4186	34	1072 ± 188	2090 ± 406	15.63 ± 9.06	20.54 ± 5.07
RCS J162008 + 3046.7	0.319	384 ± 164	0.2976	39	654 ± 133	1452 ± 226	4.61 ± 2.01	12.05 ± 2.99
RCS J211519 − 6309.5	0.331	582 ± 188	0.2261	22	345 ± 60	770 ± 133	0.64 ± 0.32	10.40 ± 3.93
RCS J212005 − 6204.8	0.472	399 ± 188	0.3595	16	502 ± 107	1174 ± 188	2.60 ± 1.23	4.53 ± 1.83
RCS J211945 − 6209.8	0.234	243 ± 144	0.3258	15	281 ± 109	581 ± 120	0.30 ± 0.46	6.37 ± 4.49
RCS J212134 − 6335.8	0.351	712 ± 200	0.2171	57	711 ± 74	1569 ± 148	5.36 ± 1.49	41.54 ± 9.56
RCS J215700 − 0441.9	···	192 ± 117	0.1668	65	658 ± 65	1511 ± 150	4.56 ± 1.36	25.97 ± 8.71
RCS J231544 + 0052.8	0.353	1176 ± 240	0.3321	29	415 ± 53	897 ± 100	1.13 ± 0.38	21.81 ± 8.06
RCS J231736 − 0103.0	0.235	512 ± 176	0.2009	20	338 ± 60	752 ± 149	0.58 ± 0.38	3.92 ± 1.34
RCS J231830 − 0024.5	0.447	581 ± 191	0.3799	27	626 ± 100	1187 ± 186	2.75 ± 1.23	19.39 ± 7.31
RCS J234356 − 3517.5	0.452	630 ± 186	0.4945	39	775 ± 120	1273 ± 165	3.84 ± 1.42	14.83 ± 3.83
RCS J234748 − 3535.1	0.289	1388 ± 260	0.2630	36	845 ± 122	1852 ± 268	9.22 ± 4.03	34.97 ± 7.60

*As stated in §2.6.2, these clusters are blended or low-significance RCS clusters; therefore B_{gcR} values have been recomputed based on their spectroscopic redshifts and centroids.

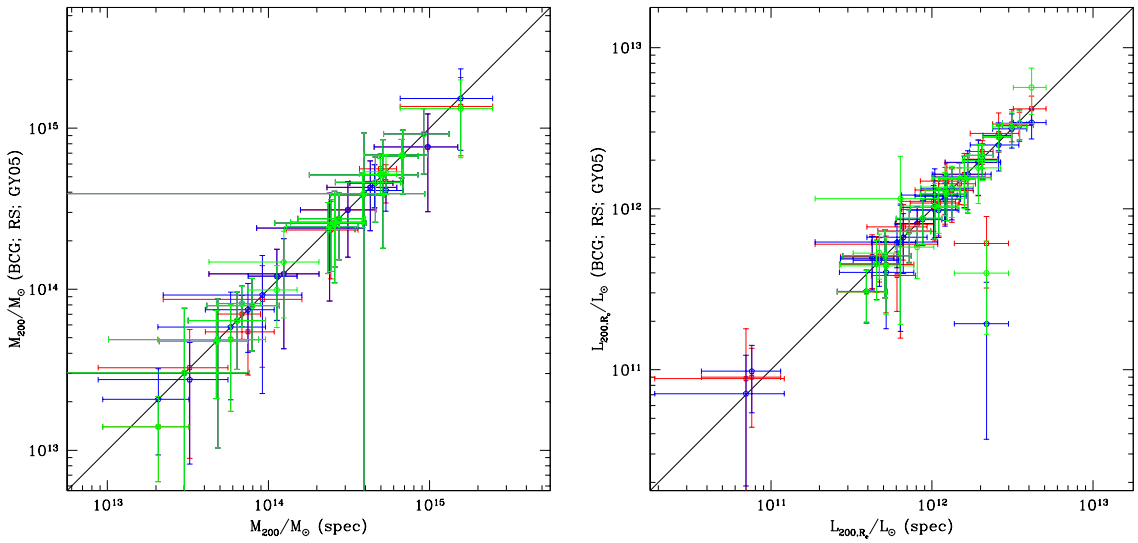

Figure 3.6 Comparison of masses (left) and luminosities (right) for different cluster centroids. The abscissas are $(\mathrm{RA,Dec})_{spec}$, and the other estimates are ordinates. Comparison between the $(\mathrm{RA,Dec})_{spec}$ and $(\mathrm{RA,Dec})_{BCG}$ estimates are shown as squares, $(\mathrm{RA,Dec})_{RS}$ as blue pentagons, and $(\mathrm{RA,Dec})_{GY05}$ as green hexagons. The 1:1 relations are shown as solid lines.

Nevertheless, the luminosity estimates agree within the errors for all but one cluster. The outlier is RCS J231544+0052.8, for which the $(\mathrm{RA,Dec})_{spec}$ estimate of luminosity is 2σ removed from the other estimates; in this apparently extreme case there are many more objects within r_{200} computed using the spectroscopic centroid, which significantly boost the luminosity.

Thus, the masses and luminosities we compute are robust through variants of cluster centroid. For the remainder of this chapter we will continue to use the spectroscopic centroid estimate, as we present the scaling relations between cluster dynamical parameters.

3.4 Cluster Scaling Relations

3.4.1 Richness versus Mass

One of the primary scientific motivations for current and planned cluster surveys is the measurement of w, the dark energy equation of state. Cosmological parameters such as Ω_M, σ_8, and w can be estimated from the evolution of the number density of clusters $N(M,z)$. The use of cluster abundances is independent of and complementary to other methods for calculating w, such as those using fluctuations in the cosmic microwave background or using supernovae of type Ia as standard candles. However, it is simply not feasible to determine masses for all

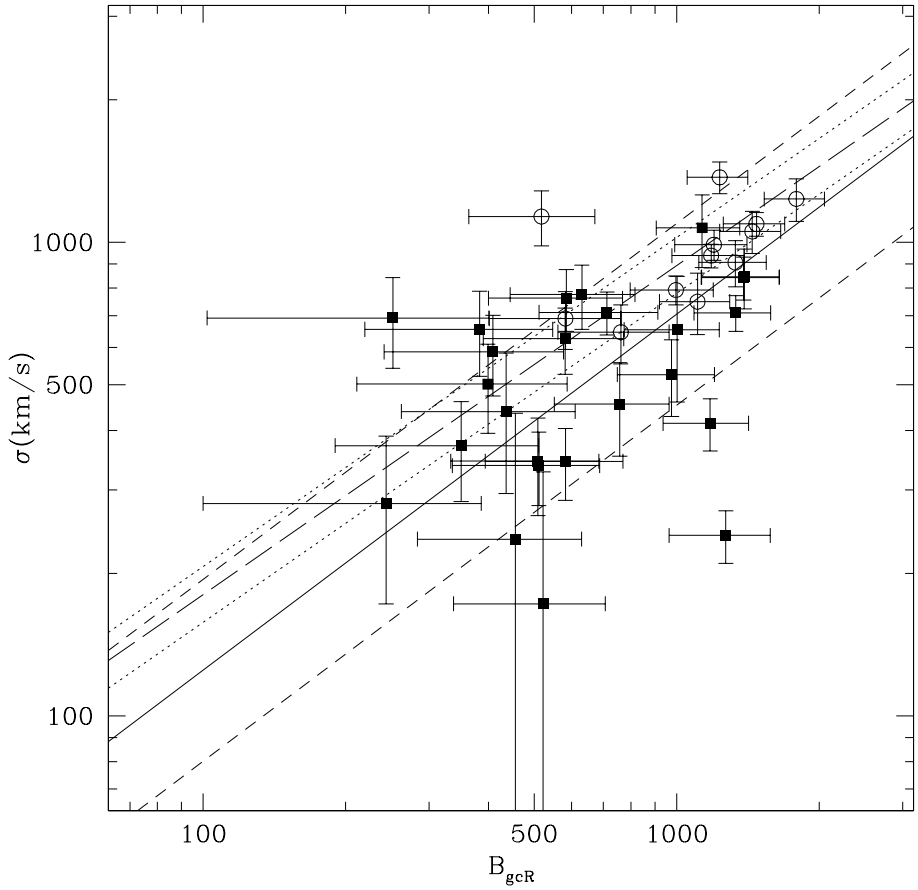

Figure 3.7 Richness versus velocity dispersion. RCS clusters from this work are shown as solid squares, CNOC1 clusters are shown as open circles. Solid line is a bisector fit[2] to the RCS clusters, and the medium-dashed lines enclose a 68% confidence interval about the fit. Also shown is the best-fit relation for the CNOC1 clusters: the long-dashed and dotted lines are the best bisector line and 68% interval respectively.

clusters in a large survey. The RCS cluster survey contains a very large sample of clusters (for instance, $\sim$1000 clusters were used for cosmological parameter estimation by Gladders et al. 2006), making follow-up of all clusters prohibitive, while the ongoing RCS2 survey will have ten times as many clusters. Clearly, then, a calibration between cluster mass and a cheaper observable such as optical richness is a necessary component of such surveys.

In Figure 3.7 we present the relation between velocity dispersion and cluster richness (as given by B_{gcR}; see §2.2.2 for details) for our sample. A bisector fit along with bootstrapped

errors yields the following relation:

$$\log(\sigma/\mathrm{km\,s^{-1}}) = (0.59 \pm 1.6) + (0.75 \pm 0.57) \log B_{gcR} \; ; \tag{3.9}$$

a confidence interval of $\pm$227km/s about this encloses 68% of the datapoints. Note that this is more than twice as large as the mean error of 92km/s on our velocity dispersion measurements, indicating an intrinsic scatter about this relation (as Figure 3.7 clearly shows). This scatter is due to the difficulty inherent in using such simple quantities to describe the many different types of clusters detected in a survey such as the RCS. Cluster masses are calculated using the virial theorem; while this is valid for relaxed clusters, clusters undergoing mergers may not be so well described by masses estimated simply from velocity dispersions. The CNOC1 clusters, which due to their X-ray selection should generally be more relaxed than RCS clusters, are also shown in Figure 3.7 and have the following best-fit relation[3]:

$$\log(\sigma/\mathrm{km\,s^{-1}}) = (0.87 \pm 1.5) + (0.70 \pm 0.50) \log B_{gcR} \; ; \tag{3.10}$$

with a scatter of $\pm$104km/s. The X-ray selected CNOC1 clusters do indeed follow a much tighter relation between richness and velocity dispersion than the RCS clusters.

Of course, the relation of greater interest is not between richness and velocity dispersion, but between richness and mass. This is shown in Figure 3.8. We use a bisector fit of $\log M_{200}$ versus $\log B_{gcR}$, and find:

$$\log(M_{200}/M_{\odot}) = (8.3 \pm 3.4) + (2.1 \pm 1.2) \log B_{gcR} \; , \tag{3.11}$$

with a 68% confidence interval of $\pm$0.46dex. This result is in good agreement with the Yee & Ellingson (2003) result for CNOC1 clusters.

Recently, Gladders et al. (2006, hereafter G06) presented the first cosmological constraints from the RCS survey. Their work utilized "self-calibration" (Majumdar & Mohr 2004), in which the evolution of the cluster abundance is fit to the cluster mass calibration alongside the cosmological parameters. They used the same form for the mass-richness relation, but also included a redshift evolution term:

$$M_{200} = 10^{A} \; {B_{gcR}}^{\alpha} \; (1+z)^{\gamma} \; . \tag{3.12}$$

Using the self-calibration method, G06 derived Ω_M and σ_8 values in agreement with the literature, as well as these values of the cluster mass parameters: $A = 10.05 \pm 0.89$, $\alpha = 1.64 \pm 0.79$, and $\gamma = 0.4 \pm 1.96$. Remarkably, although these values were derived from an unconstrained fit to the abundance data, they are in excellent agreement with our result. Unfortunately our sample does not extend sufficently far in redshift to constrain the redshift evolution term along

[3]Note that the richnesses presented in Yee & Ellingson (2003) were total B_{gc} values, whereas we present here the red-sequence B_{gcR} estimates; thus our relation is slightly different from that presented in Yee & Ellingson (2003).

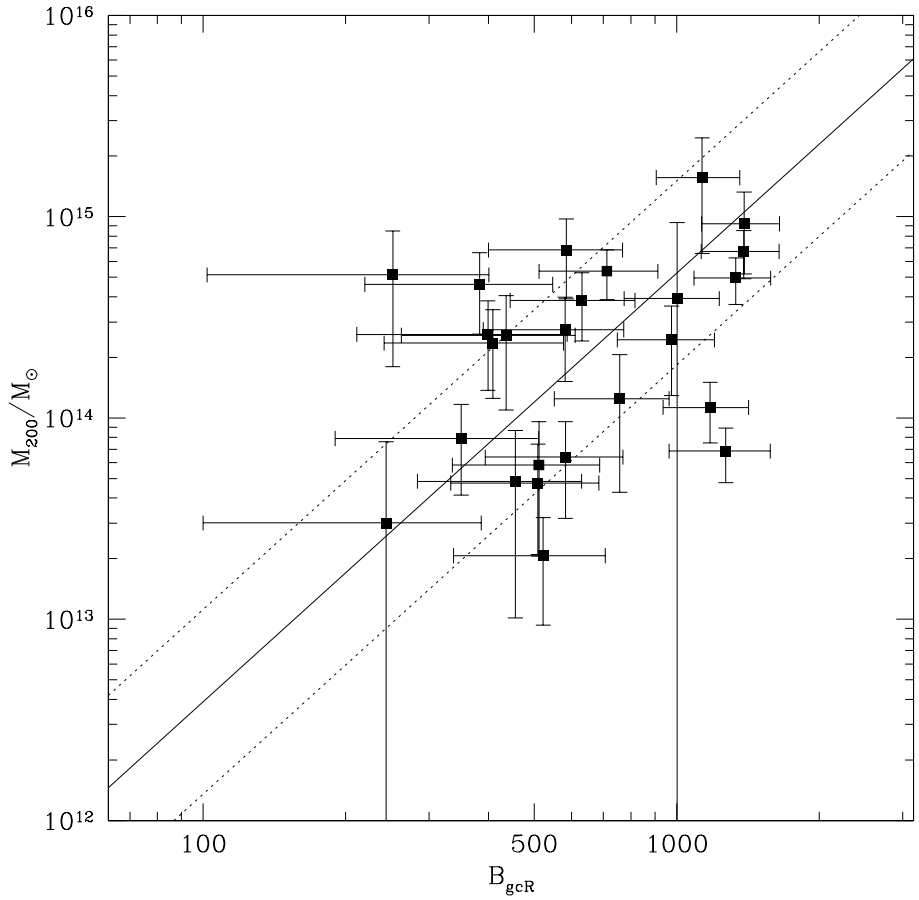

Figure 3.8 Richness versus mass, with a bisector fit shown as a solid line, and the 68% confidence interval about this fit shown as dotted lines.

with the mass and richness; constraints on γ will require a large sample extending out to high redshift.

In addition to the mass-richness calibration itself, G06 included a final cluster physics parameter in their analysis: f_{sc}, the scatter in the mass-richness relation. They derived $f_{sc} = 0.73 \pm 0.20$ from self-calibration, which also agrees very well with the scatter of $f_{sc} = 0.65$ we obtain for our clusters. G06 showed that f_{sc} does not need to be small so long as it is known. Ideally one should know not only the fractional scatter, but also its uncertainty and evolution. Our sample is not large enough to constrain the error on, or possible evolution of, f_{sc}; as with the $M - B_{gcR}$ relation itself, improvements can only be made with a larger sample. As discussed by G06, a more precise determination of A, α, and f_{sc} and their uncertainties is crucial for tightening the constraints on cosmological parameters. It is therefore very important to improve the mass calibration of RCS clusters.

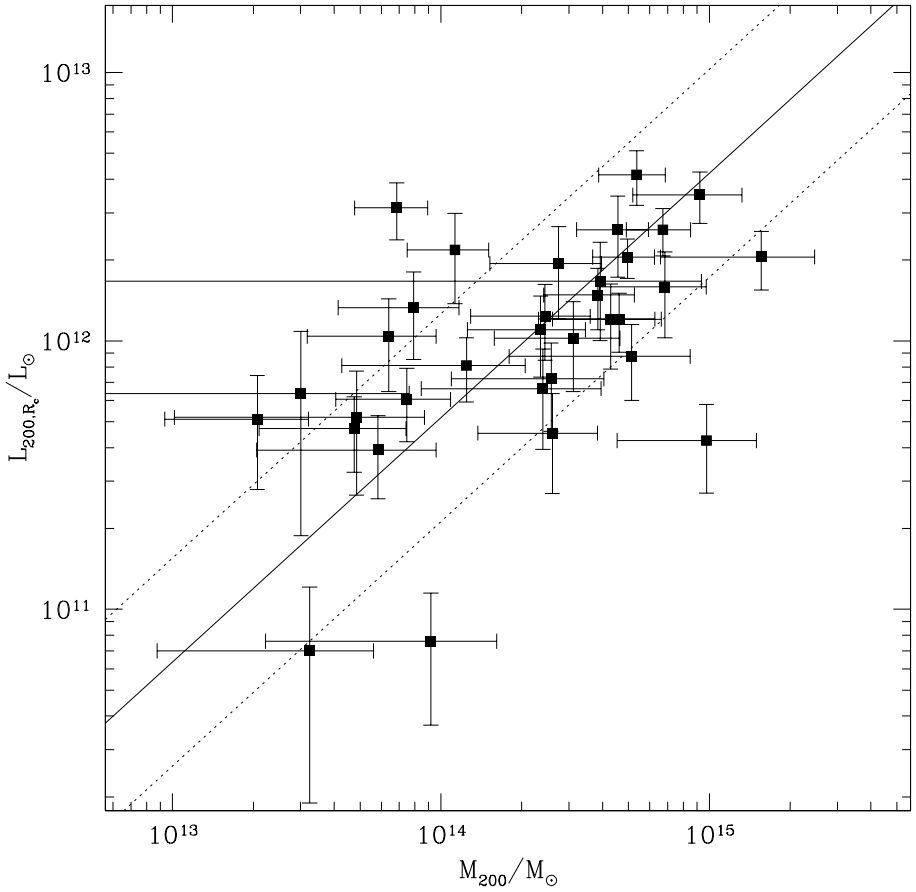

Figure 3.9 Mass versus light (R_c-band) within r_{200}. The solid line is the best-fit bisector, and the dotted lines show the 68% confidence interval about the relation.

3.4.2 Mass-to-Light Ratios

An important element of current cosmological models is the connection between structure growth and galaxy formation. In particular, it is useful to know whether galaxies cluster differently from the dark matter haloes in which they reside. This connection can be constructed theoretically using the halo occupation distribution (HOD), which essentially predicts the number of galaxies residing in a halo as a function of halo mass. More directly testable are the predicted ratios of mass to luminosity for systems such as galaxies, groups, and clusters. These ratios are set by the star formation efficiency within a system. If the luminosity is measured in a red band such as the R_c available from the RCS survey data, then the mass-to-light ratio (M/L) is related to the star formation history of the system; while for bluer bands, it tracks the current star formation rate. The average M/L ratio of clusters has been used to

estimate the matter density of the universe Ω_M (see, for example, C96). More recent studies (e.g., Bahcall & Comerford 2002; Eke et al. 2004; Tinker et al. 2005, hereafter T05) have instead addressed the dependence of the mass-to-light ratio on system mass. Generally, current models of structure formation predict a minimum M/L ratio at some characteristic scale ($\sim 10^{12} M_\odot$) — representing the scale at which star formation is most efficient. Star formation is less efficient for haloes smaller or larger than this characteristic scale, which leads to higher M/L ratios for large groups and galaxy clusters, up to a plateau value which is related to the amplitude of matter fluctuations (σ_8), a dependence illustrated nicely in Figure 6 of T05.

Although the relation of interest for comparison with models is between M/L and M, obviously these quantities have highly correlated errors. Therefore we instead fit the relation between M and L. We perform a bisector fit along with bootstrapped errors, and find:

$$\log(L_{200,Rc}/L_\odot) = (-1.0 \pm 2.8) + (0.91 \pm 0.19) \log(M_{200}/M_\odot)\,, \tag{3.13}$$

with 68% confidence interval of $\pm 0.39 \log(L_\odot)$. The data along with this fit are shown in Figure 3.9.

Although the relation between luminosity and mass is not particularly well constrained from our data alone, there does seem to be an emerging consensus among different samples. We compare our results with other observations in Figure 3.10[4]. We include the CNOC1 clusters (C96) and those CNOC2 groups with at least 5 members (Carlberg et al. 2001), as well as the weak-lensing reanalysis of the CNOC2 groups by Parker et al. (2005) which were stacked into two "ensemble" groups. We also include groups from the 2dFGRS by Eke et al. (2004)[5] which were also binned into ensembles, and SDSS groups and clusters by (Díaz & Muriel 2005). We display the SDSS systems in Figure 3.10 by a hashed region, which represents the best-fit relation and its error. We have made corrections to the results where necessary, including applying our $h = 0.7$ value for the Hubble constant, and applying small conversions to the R_c band using colours from Fukugita et al. (1995). We find good agreement between these results, which is remarkable because the samples are very different. The RCS clusters were found as overdensities in colour and angular space; the SDSS, 2dF, and CNOC2 systems were found by applying a friends-of-friends algorithm to redshift surveys; and the CNOC1 clusters were X-ray selected. Although the scatter is large even among clusters of a single type, this agreement is a great confirmation that different cluster selection procedures do find similar types of clusters (at least in terms of their global properties).

We also compare our results to the models of T05 and Marinoni & Hudson (2002). The T05

[4]This figure includes "full" Jackknife errors on the M/L ratios: for each Jackknife dataset we re-compute σ and r_{200} to allow for full variation in both M and L. This provides slightly different estimates of uncertainty than simple error propagation, because the dependence of both M and L on the virial radius means that their uncertainties are correlated.

[5]Results for the CNOC2 lensing groups and the 2dFGRS groups were kindly provided by Laura Parker and Vince Eke, by private communication.

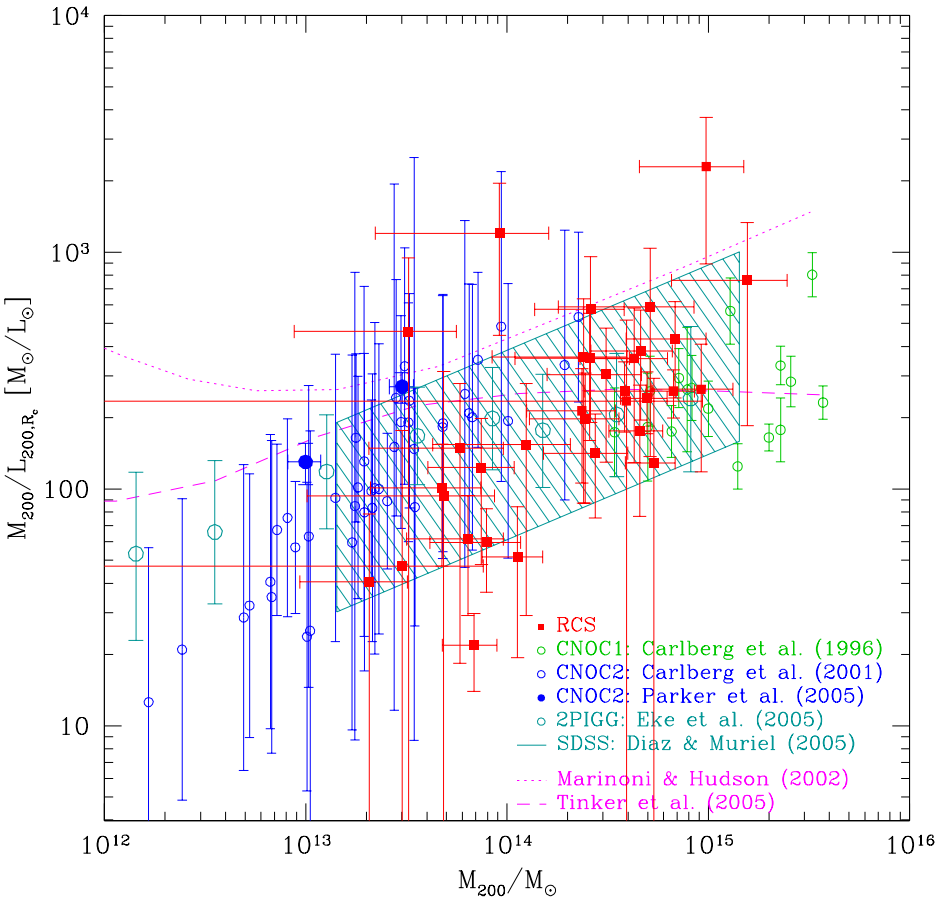

Figure 3.10 Mass versus mass-to-light ratio (R_c–band) for RCS clusters, compared to other work.

models were created using HOD on simulated ΛCDM clusters, and depend on the choice of σ_8; we show their $\sigma_8 = 0.9$ result. Marinoni & Hudson (2002) used Press-Schechter formalism to construct their models for several cosmologies; we show their ΛCDM result. As above, we apply our choice of Hubble constant and make colour corrections using Fukugita et al. (1995) colours. The Marinoni & Hudson (2002) model over-predicts the M/L values at all masses; to bring their model into agreement with the observed relation would require a brightening of approximately 1mag in their luminosities. The Marinoni & Hudson (2002) models were computed for blue luminosities and we have applied a simple correction to the R_c–band, so it is perhaps not surprising that we find an offset in the resulting M/L_{Rc} values. In contrast, the T05 models require only a small correction from Sloan r' to R_c, so they should provide a much better comparison to our RCS result. Figure 3.10 shows that they do map onto the data overall, but cannot accurately reproduce the observed behaviour at either low or high masses.

At low mass, the T05 M/L values are too high. Also they show a plateau for $M > 10^{14} M_{\odot}$, whereas the observed clusters show no plateau until at least $> 10^{15} M_{\odot}$. The values of σ_8 in the T05 models can tune the height of the plateau (higher σ_8 leads to higher plateau M/L value), but σ_8 does not affect the mass scale at which it occurs or the values of M/L at low masses. It seems the T05 model M/L ratios require alteration at both low and high masses in order to fit the observed relation. This is equivalent to adjusting the predicted star-formation efficiency. The T05 models over-predict the star-formation efficiency at low masses, and reach the minimum star-formation efficiency too early. Overall, the models do not reflect the relation between M/L and mass in observed groups and clusters.

3.5 Summary

In this chapter we have presented the global properties of RCS clusters over a large range in richness and redshift. We introduced several estimates of the cluster central location, and found that cluster dynamical parameters were not strongly affected by different choices of centroid. We also found that the two-filter photometric redshift estimates provided by the RCS cluster-finding algorithm agree well with spectroscopic redshift estimates for our clusters. We estimate the scatter in this relation to be only $\delta z \sim 0.04$, over the redshift range of our cluster sample ($z \leq 0.6$). We discussed the important issue of removing interlopers from clusters, and presented a new scaling for the shifting-gap interloper removal scheme of Fadda et al. (1996). Velocity dispersions were estimated robustly, but limited field sizes made independent calculation of virial radii unreliable. Masses were calculated using the virial theorem, and luminosities were estimated using the empirical weights presented in chapter 2.

Our analysis represents a first attempt to measure the calibration of mass to richness for RCS clusters using galaxy dynamics. This calibration is vital for large ongoing and planned cluster surveys, which hope to use the evolution of the cluster mass function to constrain w. We have compared our result to the work of G06, and found very good agreement with the cluster mass calibration they derived from an *unconstrained* fit to the cluster mass function. Progress in this field will require a new larger sample of clusters, extending out to higher redshifts[6] than our limited range of $z \leq 0.6$, in order to determine if there is any evolution in the mass-richness relation. Also, G06 have shown that it is not necessary that the scatter in the mass calibration of clusters be small, so long as it is well understood. Although our sample is sufficient to provide an estimate of the scatter in the mass-richness relation, a larger sample would be required to estimate the uncertainty on the scatter. With the advent of large-format multi-object spectrographs such as IMACS on Magellan, such large follow-up projects are now possible.

[6] N.B., much of the power to constrain cosmology comes from the $z \sim 1$ regime

We have also presented the relation between mass and light for groups and clusters, which links massive dark matter structures to the galaxies they host. Our results agree with the M/L vs. M relations for various datasets, including massive X-ray clusters and spectroscopically identified groups. Models of galaxy formation predict a minimum M/L ratio at the mass scale at which maximally efficient star formation occurs, followed by rising M/L ratios above this mass scale. Although the details depend on choices of cosmological parameters such as σ_8, it seems that current models are unable to match the observed trend.

Chapter 4

Mass and Light Profiles of Clusters

4.1 Introduction

In this chapter we examine the structure of the clusters whose observations were presented in chapter 2, and whose global properties were estimated in chapter 3. Our analysis is essentially a reconstruction of the mass profile of clusters using the galaxies as dynamical tracers, via the Jeans equation. We outline the procedure for this reconstruction in §4.2. We stack the RCS clusters into an "ensemble" in order to boost statistics. The observational ingredients required for the analysis are the number density and line-of-sight velocity dispersion profiles of the member galaxies, which we present in §4.3.2 and §4.3.3. These measurements include statistical treatment of unrelated field galaxies contaminating the cluster space, a correction particularly important at large radii where the density of cluster galaxies is comparable to that of field galaxies.

We perform the Jeans analysis for the ensemble RCS cluster in §4.3.4. We discuss degeneracies between the resulting dynamical parameters, and compare the shape of the mass profile to the expected value from simulations. In §4.3.5 we use a higher order moment of the velocity distribution to constrain the shapes of the galaxy orbits. This independent estimate of the orbital anisotropy removes an inherent degeneracy in the Jeans analysis, allowing us to more tightly constrain the mass profile. We present the dependence of the cluster mass-to-light ratio on clustercentric radius in §4.3.6, and compare with results from other observations of galaxy groups and clusters. We also perform some tests on the robustness of our results, which are described in §4.4.

In §4.5 we examine the dependence of the mass distribution with total mass. We divide the sample into ensembles of different masses, and perform dynamical analysis on each ensemble separately. We estimate the concentration of the density profile as a function of mass, and compare with the prediction from simulations of dark matter haloes. Finally in §4.6 we perform dynamical analysis on two ensembles with different mean redshifts. We estimate the

concentration parameter for each, and attempt for the first time to constrain the evolution of the concentration as a function of cluster redshift,.

4.2 The Jeans Modelling Technique

One of the most common ways to estimate the mass profile of a galaxy cluster (or other stellar systems, such as a galaxy or globular cluster) is using the velocities of members of the system and applying the Jeans equation (see, for example, §4.2 of Binney & Tremaine 1987):

$$M(<r) = -\frac{\sigma_r^2 r}{G}\left(\frac{d\ln\nu}{d\ln r} + \frac{d\ln\sigma_r^2}{d\ln r} + 2\beta\right) , \tag{4.1}$$

where σ_r is the velocity dispersion in the radial direction, ν is the number density, and $\beta = 1 - \sigma_t^2/\sigma_r^2$ is the velocity anisotropy parameter. This equation applies to equilibrium, non-rotating, spherical systems. The observable profiles $\Sigma(R)$ and $\sigma(R)$ are simply projections of $\nu(r)$ and $\sigma_r(r)$. This equation is tricky to solve directly, because it requires derivatives of often noisy data; therefore it is desirable to invert the problem. In this work we use the method of van der Marel et al. (2000, hereafter vdM00)[1]:

1. Parameterize the observed $\Sigma(R)$ profile with a fitting function. Deproject it using Abel integration to find the intrinsic number density $\nu(r)$.

2. Choose a model mass density profile. We use a generalized version of the universal profile found by Navarro et al. (1996, 1997, hereafter NFW) for simulated dark matter haloes:
$$\frac{\rho(r)}{\rho_0} = \left(\frac{r}{a}\right)^{-\gamma}\left[1 + \left(\frac{r}{a}\right)\right]^{\gamma-3} ; \tag{4.2}$$
ρ_0 and a are the normalization and scale radius, and γ is the inner slope (e.g., $\gamma = 1$ corresponds to the NFW profile, and $\gamma = 0$ has an inner core). This generalized form was introduced by vdM00. For the NFW case, it is straightforward to compare the fit scale radius to the concentration parameter c used in simulations: $c = 1/a$.

3. Choose a model for the velocity anisotropy. We restrict ourselves to models with constant $\beta(r)$.

4. Use the model $\rho(r)$ and $\beta(r)$, along with the number density $\nu(r)$, to compute a predicted projected velocity dispersion profile $\sigma(r)$. Compare this with the observed profile.

The parameter ranges used for the calculations are given in table 4.1. This procedure yields a best-fitting model — i.e., best-fit density profile parameters (ρ_0, a, γ) and anisotropy parameter β. These parameters are degenerate, because the $\sigma(R)$ profile alone does not contain

[1]Several Fortran codes for this analysis were generously provided by Roeland van der Marel.

Table 4.1. Parameter ranges for Jeans modelling

Parameter	Minimum	Maximum	Sampling	Number of points
σ_r/σ_t	$\frac{1}{3}$	3	logarithmic	11
γ	0	2	linear	21
a	0.1	10	logarithmic	21

enough information to constrain both the mass density and anisotropy. This is a well known degeneracy (see, for example, vdM00; Biviano & Girardi 2003; Łokas & Mamon 2003; Łokas et al. 2006, hereafter LM06) Higher-order moments of the velocity distribution are required to break the degeneracy (see §4.3.5).

4.3 The Ensemble RCS Cluster

In our survey there are only $\sim$10–100 members per cluster, insufficient to compute velocity dispersion and number density profiles for each cluster individually. Therefore, we stack the clusters together into a single "ensemble" RCS cluster, employing the usual scaling (Carlberg et al. 1997, hereafter C97; Biviano & Girardi 2003): the projected cluster-centric radius and velocity of each galaxy are scaled by the virial radius and velocity dispersion for its parent cluster, yielding a dataset of $(R/r_{200}, v/\sigma)$ points. This stacking procedure has the advantage of washing out possible asphericity or substructure of the individual clusters, which makes the Jeans modelling more reliable. We include in this ensemble (and all other ensembles in this chapter) only the galaxies above our average completeness limit of $M^* + 2$ (see §2.5). The number-weighted average mass of this ensemble is $3.9 \times 10^{14} M_\odot$. We show the ensemble cluster in R–v space in Figure 4.1. The core region of the cluster is well sampled, out to $\sim 2r_{200}$; outside this radius the number of cluster members drops off rapidly. We consider only galaxies within a broad velocity cut-off of $|v| \leq 25\sigma$: wide enough to include many field galaxies but narrow enough to avoid regions of redshift space our survey was not designed to probe (i.e., where we no longer properly sample the field). There are 1056 galaxies in the ensemble within this velocity cut. We define the "cluster" region to have $|v| \leq 3\sigma$, and the "field" region to have $5\sigma \leq |v| \leq 25\sigma$; the region between 3–5$\sigma$ may include both field and cluster (or in-falling) galaxies, and so we exclude it in all analysis. The cluster and field regions contain 706 and 336 galaxies, respectively (the number of members in this ensemble is lower than the total one

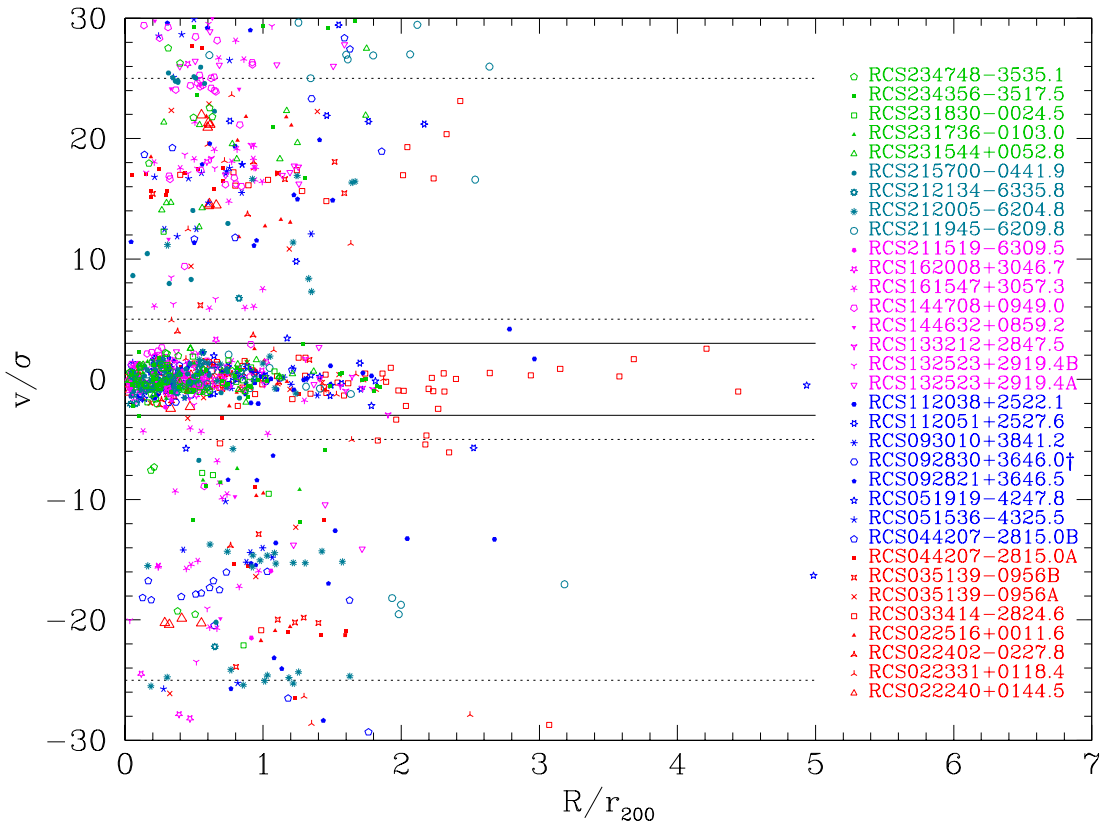

Figure 4.1 The ensemble RCS galaxy cluster. Solid lines enclose the "cluster" region of R–v space, and dotted lines enclose the foreground and background "field" regions.

would obtain from Table 3.2 because of the magnitude cut we impose).

4.3.1 Contamination From Field Galaxies

Field galaxies will also be present in the "cluster" region of this ensemble (or any cluster, for that matter), because background and foreground galaxies will be projected into the cluster redshift space. These interlopers are indistinguishable from true members which are bound to the cluster. Therefore, they cannot be removed from the sample and must be treated statistically. We do this by computing the density of galaxies in the "field" region of R–v space, and using it to estimate the density of interloping galaxies within the cluster; details are described in §4.3.2 and §4.3.3.

4.3.2 The Number Density Profile

One of the main ingredients necessary to calculate mass profiles using the Jeans equations is the radial profile of the number density of galaxies. Because we have already computed

Table 4.2. Background weights, number of members, and maximum radii for the RCS clusters

Cluster Name	N_{mem}	R_{max}/r_{200}	W_{back}
RCS J022240 + 0144.5	18	0.64	0.5
RCS J022331 + 0118.4	21	1.87	1.0
RCS J022402 − 0227.8	18	1.11	1.0
RCS J022516 + 0011.5	19	1.17	1.0
RCS J033414 − 2824.6	56	5.46	1.0
RCS J035139 − 0956.3A	17	1.55	0.5
RCS J035139 − 0956.3B	11	2.43	1.0
RCS J044207 − 2815.0A	12	1.26	1.0
RCS J044207 − 2815.0B	13	1.21	1.0
RCS J051536 − 4325.5	12	0.67	1.0
RCS J051919 − 4247.8	13	4.94	1.0
RCS J092821 + 3646.5	38	1.73	1.0
RCS J092830 + 3646.0†	6	1.60	0.5
RCS J093010 + 3841.2	20	1.39	1.0
RCS J112038 + 2522.1	17	2.96	1.0
RCS J112051 + 2527.6	13	4.68	1.0
RCS J132523 + 2919.4A	16	1.41	1.0
RCS J132523 + 2919.4B	10	0.50	1.0
RCS J133212 + 2847.5	10	1.90	1.0
RCS J144632 + 0859.2	16	0.60	0.5
RCS J144708 + 0949.0	52	1.70	0.5
RCS J161547 + 3057.3	30	1.30	1.0
RCS J162008 + 3046.7	24	1.02	1.0
RCS J211519 − 6309.5	16	0.76	1.0
RCS J211945 − 6209.8	12	3.88	1.0
RCS J212005 − 6204.8	13	1.24	1.0
RCS J212134 − 6335.8	39	1.18	0.5
RCS J215700 − 0441.9	36	0.93	0.5
RCS J231544 + 0052.8	25	1.37	1.0
RCS J231736 − 0103.0	13	0.88	0.5
RCS J231830 − 0024.5	22	1.13	1.0
RCS J234356 − 3517.5	32	1.85	1.0
RCS J234748 − 3535.1	35	0.87	1.0

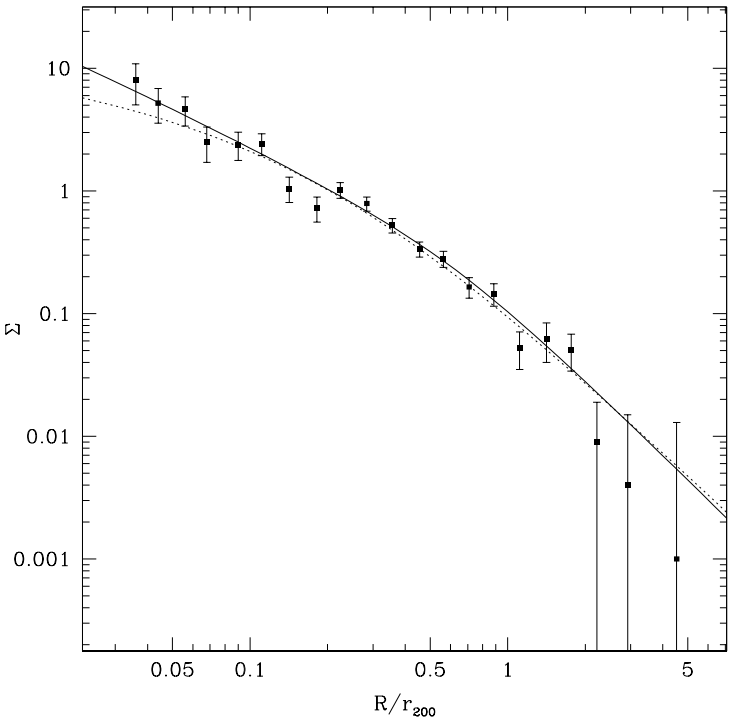

Figure 4.2 Number density profile of RCS clusters, with Jackknife errors (arbitrary normalization). The uncertainties at large radii are due to small number statistics: the final two radial bins contain fewer than 5 objects each. The best-fit modified Nuker law is shown as a solid line, and the projected NFW profile is shown as a dotted line.

geometric weights to account for incompleteness in the redshift catalogues (see §2.5), this is a relatively straightforward calculation of the weighted number of galaxies per unit area, with only a few complicating factors:

- Because the clusters have different maximum R/r_{200} (as can clearly be seen in Figure 4.1), an additional weight is necessary. At each radius R_i we compute W_{clust}, the total number of members in the ensemble divided by the number of members in all clusters for which the maximum radius $r_{max,j} \geq R_i$.

- As mentioned above we must account for interloping field galaxies. Following C97, we make the simplifying assumption that the density of interloping galaxies is independent of radius and velocity, and count the average weighted number of galaxies in the "field" region per unit velocity, $\langle N_{back} \rangle$. The number is then divided by the effective area, which is simply the average area of coverage for each cluster weighted by the number of members in each cluster. The density thus calculated represents the number of interloping

galaxies per unit area and velocity. This background density is subtracted from the computed number density in each radial bin.

- Some of the RCS clusters are at sufficiently low redshifts that their foregrounds are poorly sampled (for instance, RCS J035139-0956.3A at $z_{spec} = 0.1678$). In these cases, we simply use the background region (i.e., $v > +5\sigma$) to estimate background, and divide the resulting number by a background weight $W_{back} = 0.5$.

Table 4.2 lists the number of members and maximum radii for the RCS clusters (using only galaxies brighter than $M^* + 2$ within the $|v| \leq 3\sigma$ "cluster" region), as well as the W_{back} values. These corrections have little effect at small radii (where the density of cluster members is much larger than that of the field galaxies and R_i is much smaller than the maximum radius of any cluster) and become increasingly important beyond r_{200}. The number density profile $\Sigma(R)$, with Jackknife errors, is shown in Figure 4.2.

We fit the number density profile to a projected NFW model using the formula of Łokas & Mamon (2001):

$$\begin{aligned}
\Sigma(R) &= \left(\frac{200}{3}\right)\rho_0 c^2 g(c) \quad \frac{1 - \left|x^2-1\right|^{-1/2} C^{-1}(1/x)}{\left(x^2-1\right)^2} \text{, where} \qquad (4.3)\\
g(c) &= 1/\left[\ln(1+c) - c/(1+c)\right] \text{ ,}\\
C^{-1}(x) &= \begin{cases} \text{acos}(x) & \text{if } x < 1 \\ \text{acosh}(x) & \text{if } x > 1 \end{cases} \text{, and}\\
x &\equiv c(R/r_{200}) \text{ .}
\end{aligned}$$

The best-fit projected NFW model has concentration parameter $c = 4.8 \pm 0.9$, in agreement with expectation from simulations (Nagai & Kravtsov 2005). See §4.5.3 for further discussion of concentration parameters.

For use in the Jeans equations, $\Sigma(R)$ must be de-projected using the Abel equation. To that end we follow vdM00 and parameterize the $\Sigma(R)$ profile using a modified Nuker law:

$$\Sigma(R) = \Sigma_b \quad 2^{(\beta-\gamma)/\alpha}(R/r_b)^{-\gamma}[1 + (R/r_b)^{\alpha}]^{-(\beta-\gamma)/\alpha}[1 + (R/r_c)^{\delta}]^{-(\epsilon-\beta)/\delta} \text{ ,} \qquad (4.4)$$

and find the best-fitting parameters: $\Sigma_b = 0.877$, $r_b = 0.2368$, $r_c = 0.60$, $\alpha = 0.1$, $\beta = 2.2243$, $\gamma = 0.0$, $\delta = 2.4035$, $\epsilon = 3.0$ (although note that these parameters are highly correlated). As Figure 4.2 shows, the best-fit modified Nuker profile is nearly identical to the projected NFW model, except at small radii where it fits the data slightly better than the comparatively shallow NFW profile. Both provide acceptable fits, with reduced $\chi^2 = 0.86$ and 1.29 respectively.

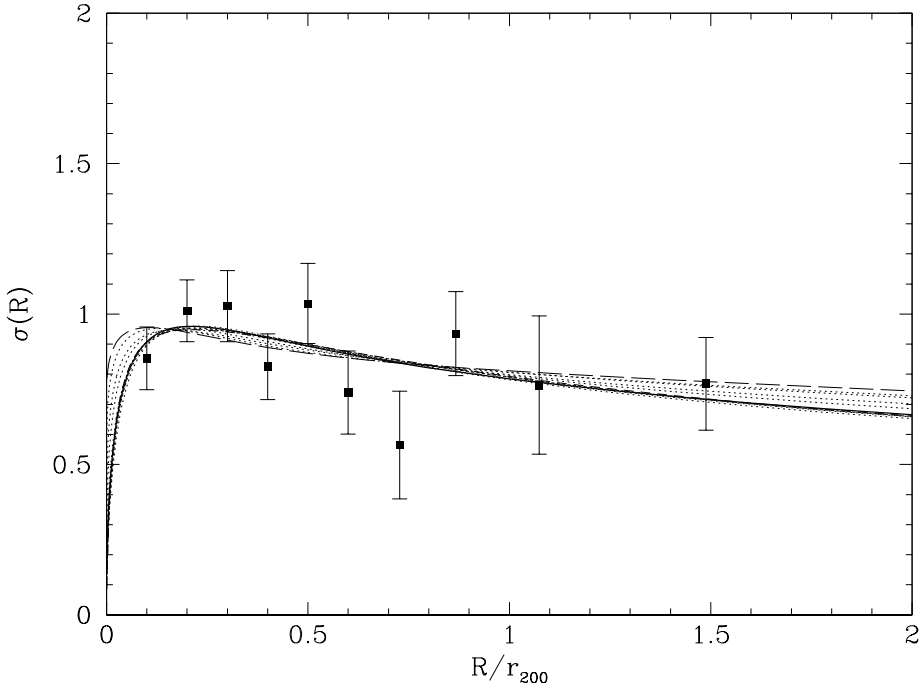

Figure 4.3 Projected velocity dispersion profile, computed in 51-point running bins and resampled at intervals of $0.1r_{200}$ or larger to ensure that datapoints are independent. Also shown are predicted profiles for the best-fit model for each anisotropy: the thick line is an isotropic model, the long-dashed line has strong radial anisotropy ($\sigma_r/\sigma_t = 3$), and the short-dashed line has strong tangential anisotropy with $\sigma_r/\sigma_t = 1/3$ (though it is nearly invisible, on top of the isotropic model).

4.3.3 The Velocity Dispersion Profile

The second observed quantity required for Jeans modelling is the line-of-sight velocity dispersion $\sigma(R)$. We compute velocity dispersion as a second moment of the velocity distribution, with a weighting scheme to subtract interlopers. The v/σ data points are placed into velocity bins of width 0.1σ (although the results are insensitive to reasonable choices of bin width); associated with each bin i are v_i, the mean velocity, and n_i the number of galaxies in the bin. We compute $\langle n_{field} \rangle$, the expected number of field galaxies in each velocity bin, as the average number of galaxies per bin in the "field" region between 5–25σ. Then the velocity dispersion is simply

$$\sigma^2 = \frac{\sum w_i v_i^2}{\sum w_i} - \langle v_i \rangle^2 \ , \tag{4.5}$$

where $w_i = n_i - \langle n_{field} \rangle$ and the sums are over the "cluster" region $|v| \leq 3\sigma$. Errors are estimated by Jackknife using the whole $|v| \leq 25\sigma$ region. We compute the velocity dispersion

in running bins of 51 galaxies, which we sample in intervals of $0.1r_{200}$ or wider to ensure that the resulting datapoints are independent. The resulting profile is shown in Figure 4.3. We have compared this profile to that obtained using the robust velocity dispersion estimator described in §3.3.2. The two methods yield virtually identical results at small radii, but σ_{rob} is higher by ~ 0.1 at large R due to the larger fraction of interlopers.

4.3.4 The Mass Profile

We have applied the Jeans modelling technique outlined in §4.2 to the $\nu(r)$ and $\sigma(R)$ profiles for the ensemble RCS cluster. The best fit was obtained for $\sigma_r/\sigma_t = 0$, $\gamma = 0.3$, and $\log a = -0.8$, with reduced $\chi^2 = 0.8$. In order to explore these results further, we examine the χ^2 contours (spline-interpolating between the locations where models were computed). As can be seen in Figure 4.4, the parameters are not well constrained. This is expected, due to the degeneracy between anisotropy and mass density mentioned in §4.2. Figure 4.3 illustrates the point, plotting the predicted $\sigma(R)$ profiles of the best-fit (a, γ) for each σ_r/σ_t. The models range from very tangential to very radial anisotropies, but changes in the mass density compensate to produce a similar velocity dispersion profile. The only significant differences arise at very small radii, where the models are unconstrained by data. The corresponding enclosed mass profile is shown in Figure 4.5. Although the best-fit $M(< r)$ is quite dependent on anisotropy, the enclosed mass at $r \sim r_{200}$ is stable. This result is in agreement with that found for CNOC1 clusters by vdM00, and suggests that the virial masses and mass-to-light ratios estimated in Chapter 3 are not significantly affected by the shapes of galaxy orbits.

In addition to the well-known degeneracy between mass and anisotropy, there appears to be a degeneracy even for fixed β. In Figure 4.6 we show the confidence contours for the isotropic models. Although the minimum χ^2 is obtained for $\log a = -0.8$ and $\gamma = 0.3$, the contours of constant χ^2 are banana-shaped and allow for the full range of computed a and γ. That is, we are unable to individually constrain both the scale radius and inner slope. A similar degeneracy was found for 2dFGRS clusters by Biviano & Girardi (2003), as well as for CNOC1 clusters (R. van der Marel, personal communication). This is perhaps not surprising: these data-sets simply do not extend to sufficiently small radii to properly constrain the inner slope of the density profile. It is certainly desirable to determine γ, which is a matter of some debate (e.g., Diemand et al. 2005; Lu et al. 2006, and references therein), but this would require a different approach such as strong lensing arc statistics (Sand et al. 2005) to probe the core regions of clusters. It would also be interesting to test the expected $\rho \propto r^{-3}$ behaviour at large radii, but our data do not extend sufficiently far in radius for such a test; also, at large radii the assumption of dynamical equilibrium needed for Jeans modelling no longer holds, so the outer regions of clusters are better examined using another method (for instance the caustic method of Diaferio & Geller 1997; Diaferio 1999). However, for a fixed value of γ, Figure

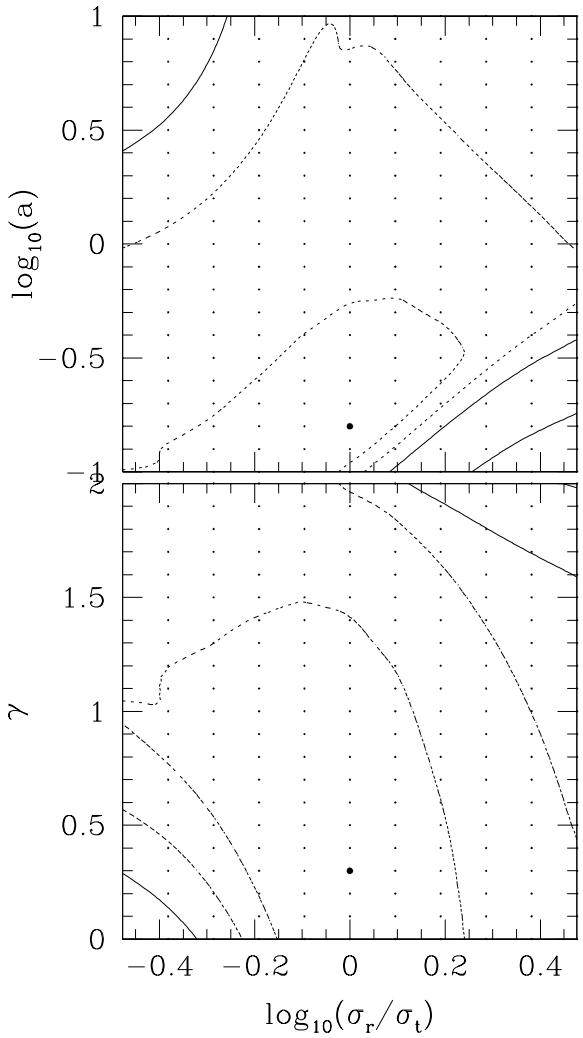

Figure 4.4 Confidence contours of the mass and anisotropy parameters for the RCS ensemble cluster. Dots denote the locations at which the Jeans modelling was performed; the large dot shows the location with minimum χ^2. Confidence contours were constructed using spline interpolation: dotted lines are linearly spaced χ^2 contours, and solid line contours correspond to 1σ and 2σ confidence.

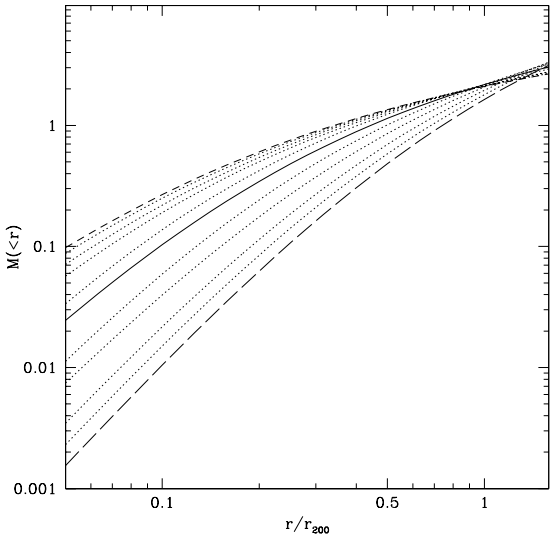

Figure 4.5 Mass profile of the RCS ensemble cluster, for different choices of anisotropy. Lines are defined as for Figure 4.3 (the thick line is the best-fit isotropic model).

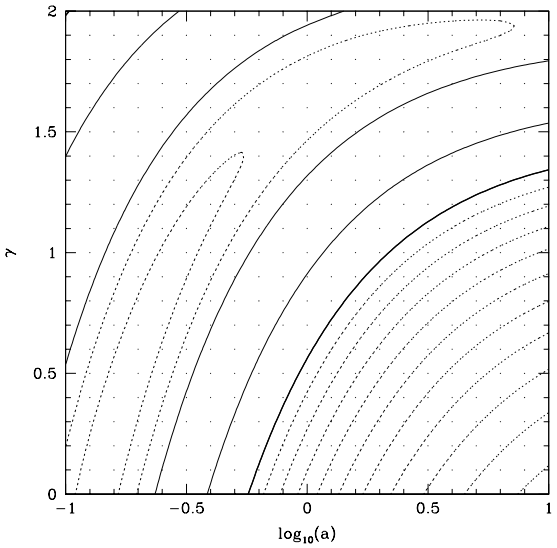

Figure 4.6 Confidence contours of the mass parameters, for the isotropic model. Dots denote the locations at which the Jeans modelling was performed. Thin solid lines correspond to 1σ and 2σ confidence limits; thick solid line corresponds to 3σ. Inner dotted lines are linearly spaced χ^2 contours, and outer dotted lines are logarithmically spaced.

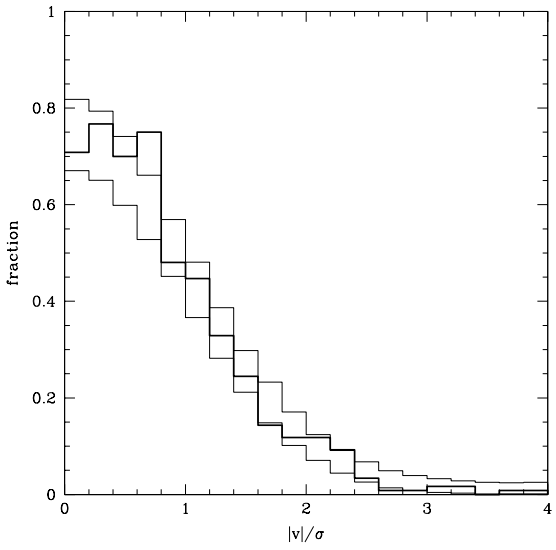

Figure 4.7 Velocity histogram of the ensemble cluster, heavy line. Thin lines enclose the predictions for Monte-Carlo drawings of an isotropic model plus background.

4.6 shows that the scale radius is well determined. For the NFW case with isotropic orbits ($\sigma_r/\sigma_t = 0, \gamma = 1$), we recover scale radius $a = 0.29^{+0.21}_{-0.12}$, very similar to the scale radius found by vdM00 for CNOC1 clusters. This is equivalent to a concentration parameter $c = 3.4^{+2.5}_{-1.4}$, in agreement with predictions from cosmological simulations (see §4.5.3 for further discussion).

4.3.5 Constraints on the Orbital Anisotropy

Although Jeans modelling produces a degeneracy between the mass density and the anisotropy of galaxy orbits, this degeneracy can be broken by examining the full velocity profile rather than simply the velocity dispersion. Models with radial anisotropy have peaked velocity histograms, those with tangential anisotropy have flat-topped histograms, and isotropic orbits lead to a Gaussian distribution. In Figure 4.7 we qualitatively examine the deviation of the observed histogram from a model Gaussian. The model includes an offset due to field galaxies, and we perform a Monte-Carlo drawing to estimate the uncertainty in the histogram. We find that the observed histogram agrees very well with the Gaussian prediction.

To further explore possible orbital anisotropy for the RCS ensemble cluster, we can employ higher order moments of this distribution. This has become a common practice (e.g., vdM00, LM06). Straightforward statistics such as kurtosis depend on the shape of the wings of the distribution, which are sensitive to interlopers (although tests by LM06 on 10 simulated clusters show no significant problems in recovering the correct velocity anisotropy using

kurtosis). We follow vdM00 and use the Gauss-Hermite moments (van der Marel & Franx 1993). The moment relevant for our use, analogous to the kurtosis, is h_4: h_4 is negative for flat-topped distributions and positive for peaked distributions. That is, $h_4 < 0$ indicates tangential anisotropy and $h_4 > 0$ indicates radial anisotropy (and of course, for the isotropic case we recover a Gaussian: $h_4 = 0$.). We calculate h_4 from the velocity distribution of Figure 4.7 after subtracting the offset due to interlopers, and estimate uncertainty using Monte-Carlo drawing: we find $h_4 = -0.025 \pm 0.028$. The equivalent range in anisotropy is approximately $0.96 < \sigma_r/\sigma_t < 1.004$ (see Figure 8 of vdM00). That is, in accordance with our qualitative assessment, the velocity distribution of the ensemble cluster is consistent with a Gaussian. In fact, although the negative h_4 favours a slight tangential anisotropy, Sanchis et al. (2004) and Łokas et al. (2006) have shown that measured anisotropies tend to be biased slightly low. Therefore it is likely that the true value of h_4 is even closer to zero, and we conclude that the galaxy orbits of the RCS ensemble cluster must be nearly isotropic.

4.3.6 The Mass-to-Light Ratio Profile

With a mass model in hand, we can easily compute the mass-to-number density ratio profile of the ensemble cluster as a proxy for the mass-to-light ratio. $\rho(r)/\nu(r)$ is shown in Figure 4.8 for the best-fit mass model for each value of σ_r/σ_t. This profile depends strongly on the anisotropy of the system: for radially/tangential anisotropy we find a falling/rising $\rho(r)/\nu(r)$ with radius. However, in §4.3.5 we showed that the ensemble RCS cluster has roughly isotropic orbits. For the isotropic case, $\rho(r)/\nu(r)$ is nearly flat as a function of radius, at least for $R \geq 0.1 r_{200}$, where our mass profile is constrained by the data.

Another estimate of M/L can be made by directly computing the luminosity rather than using the number density. We compute luminosities using the same procedure we employed in estimating the total luminosity within r_{200} (see §3.3.5), for different maximum radii. The resulting profile is a projected enclosed luminosity: $L_{Rc}(< R)$. For isotropic NFW models, Łokas & Mamon (2001) provide a formula for the enclosed projected mass:

$$M_{NFW}(< R) = \left(\frac{600\pi}{3}\right) \rho_0 g(c) \quad \left[\frac{C^{-1}(1/x)}{|x^2-1|^{1/2}} + \ln\left(\frac{x}{2}\right)\right] \tag{4.6}$$

where $g(c)$, x, and $C^{-1}(x)$ are given in Equation 4.4. We divide this mass by $L_{Rc}(< R)$, and present the projected enclosed mass-to-light ratio profile in Figure 4.9. We find the M/L to be consistent with a line of zero slope, although it does decline slightly with radius. Note that this result implies that the M/L ratios of chapter 3 are not strongly dependent on the apertures used to compute them.

Our derived M/L_{Rc} profile for the RCS ensemble cluster is in excellent agreement with profiles found for CNOC1 clusters by both C97 and vdM00, as well as for nearby Abell clusters

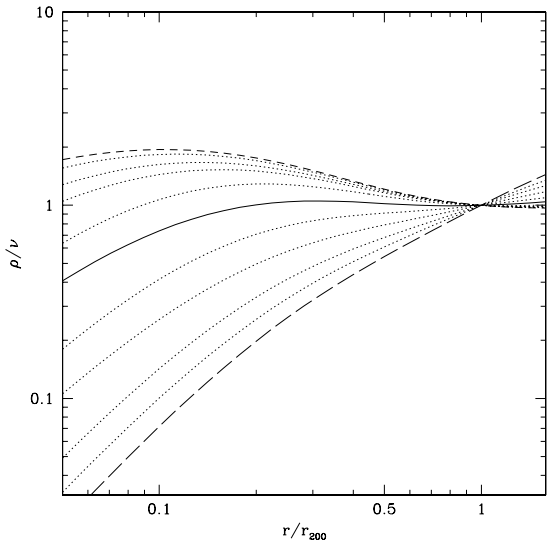

Figure 4.8 Ratio of mass density to number density as a function of radius, normalized by $\rho/\nu(R = r_{200})$. Lines are defined as for Figure 4.3 (the isotropic model is shown as a thick line).

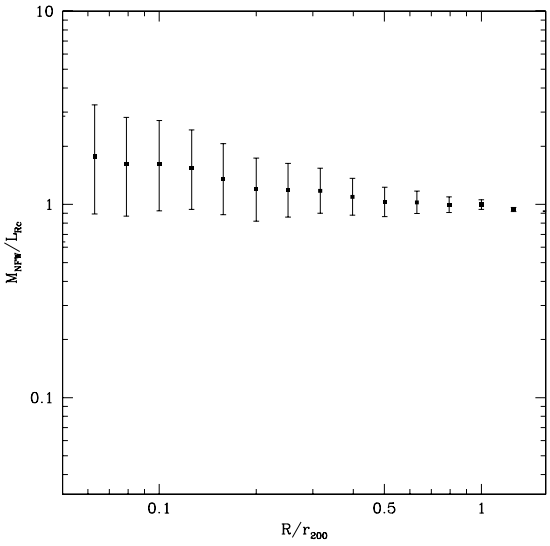

Figure 4.9 Projected enclosed mass-to-light ratio as a function of radius, using the best-fitting NFW model and the observed luminosity profile. Error bars include Jackknife errors in the observed luminosity profile as well as 1σ variation in the concentration parameter. Profile is normalized to the value at $R = r_{200}$.

in both R-band (Katgert et al. 2004) and K-band (Rines et al. 2004), and for 2dFGRS clusters (Biviano & Girardi 2003). Our result is at odds with the rising mass-to-light ratio found for galaxy groups in the CNOC2 survey (Carlberg et al. 2001), although a weak lensing analysis of these same groups by Parker et al. (2005) is again consistent with a nearly constant M/L which suggests that the Carlberg et al. (2001) work may need to be revisited.

4.4 Testing the Jeans Modelling

We have performed a few simple tests of the robustness of our modelling. First, we test results for the well-studied CNOC1 ensemble clusters, using the number density profile of C97 and the velocity dispersion profile of vdM00. We test the stability of the model against perturbation of the velocity dispersion, by perturbing the large-R points in the $\sigma(R)$ profile. Although the formal best-fit values of $(\sigma_r/\sigma_t, \gamma, a)$ vary considerably, this is simply because of the degeneracies involved: the minimum χ^2 simply shifts along the banana-shaped confidence contours whose position remains stable. For instance, for isotropic NFW models, the best-fit concentration values agree well within the 1σ uncertainties even when the final point in the $\sigma(R)$ profile is shifted upwards by three times its uncertainty. The concentration also remains stable when we use our own version of $\Sigma(R)$ and $\sigma(R)$ for re-scaled radii (using r_{200} values adjusted for our chosen cosmology), with velocity dispersion restricted to $R \leq r_{200}$ — although the uncertainty is considerably larger with this limited radial range.

We have also tested the resilience of the concentration parameter to changes in radial sampling of $\sigma(R)$ for the ensemble RCS cluster. The value of c changes little, either when $\sigma(R)$ is restricted to radii within r_{200} or when it is sampled out to $1.7r_{200}$ at intervals of $0.1r_{200}$ (which leads to dependent datapoints for radii beyond $0.6r_{200}$). Thus it appears that c is insensitive to moderate perturbations in the input data for both the CNOC1 and RCS ensemble clusters. Concentrations for the test models are listed in Table 4.3.

It is of course important to know not only how sensitive a measurement is to perturbations of the input data, but how close it is to the *true* value. vdM00 explored the effects of nonsphericity using stacked axisymmetric Hernquist models, and found essentially no bias in the profiles of projected intensity, velocity dispersion, or Gauss-Hermite moment; their results were also stable to changes in radial scaling. Sanchis et al. (2004) and LM06 have used N-body simulations of dark matter haloes; they found that, although the velocity dispersion and kurtosis profiles are affected by effects found in cosmological simulations (such as nonsphericity and substructure), the concentration and anisotropy are robust. Although these results are certainly encouraging, the vdM00 tests were performed on somewhat idealized models while Sanchis et al. (2004) and LM06 use a somewhat different modelling method and do not address possible issues arising from the stacking of individual clusters into ensembles. Ultimately, we

Table 4.3. Output concentrations for various test inputs

Run #	Input data	c[1]
CNOC1 ensemble cluster		
1	$\Sigma(R)$ from Carlberg et al. (1997), $\sigma(R)$ from van der Marel et al. (2000)	$3.0^{+1.6}_{-1.0}$
2	same as run 1, but outermost $\sigma(R)$ point shifted up by $1\times$ uncertainty	$2.7^{+1.5}_{-1.0}$
3	same as run 1, but two outermost $\sigma(R)$ points shifted up by $1\times$ uncertainty	$2.5^{+1.4}_{-0.9}$
4	same as run 1, but outermost $\sigma(R)$ point shifted up by $3\times$ uncertainty	$2.5^{+1.2}_{-0.8}$
5	re-scaled radii, recomputed $\Sigma(R)$ and $\sigma(R)$, $R \leq r_{200}$	$5.0^{+3.5}_{-2.0}$
RCS ensemble cluster		
1	$\Sigma(R)$ and $\sigma(R)$ as shown in Figures 4.2 and 4.3	$3.4^{+2.5}_{-1.4}$
2	same as run 1, but $\sigma(R)$ sampled at $0.1r_{200}$ intervals out to $1.7r_{200}$	$3.3^{+2.3}_{-1.3}$
3	same as run 2, but $\sigma(R)$ for $R \leq r_{200}$ only	$3.9^{+3.0}_{-1.7}$

[1]concentration parameter for isotropic NFW model (i.e., $\sigma_r/\sigma_t = 0$, $\gamma = 1$).

plan to test our technique using cosmological simulations, but such extensive testing is beyond the scope of this thesis.

4.5 Results as a Function of Cluster Mass

In order to explore the dependence of dynamical parameters on cluster mass, we must split our data into several ensembles of different masses. Because the RCS clusters generally have low masses (see Table 3.2), we will also include CNOC1 clusters. Since the CNOC1 clusters follow the same scaling relation between mass and luminosity as the RCS clusters (cf. Figure 3.10), and the ensemble CNOC1 and RCS clusters have similar dynamical properties, these two families of clusters appear to be homologous and so we deem it safe to stack the CNOC1 and RCS clusters together.

To properly stack the ensembles, the clusters must have appropriately scaled velocities and radii, and should all be sampled to the same depth. We update the CNOC1 cluster data, by rescaling their masses and r_{200} using our current cosmology and by sampling down to

Table 4.4. Global properties of the CNOC1 clusters

Cluster name	z_{spec}	r_{200}/Mpc	$M_{200}/10^{14}M_{\odot}$	N_{mem}	R_{max}/r_{200}	W_{back}
A2390	0.2280	2.4	20.1	193	1.99	1.0
MS0015	0.5465	2.3	24.0	62	0.91	1.0
MS0302	0.4245	1.3	3.7	31	1.12	1.0
MS0440	0.1965	1.4	3.5	48	1.94	0.5
MS0451N	0.2011	2.2	15.0	124	1.86	0.5
MS0451S	0.5391	2.5	33.1	60	0.77	1.0
MS0839	0.1930	1.7	6.6	48	0.87	0.5
MS1006	0.2604	2.0	11.2	31	0.54	1.0
MS1008	0.3063	2.2	17.2	72	0.58	0.5
MS1224	0.3255	1.7	7.5	27	0.78	1.0
MS1231	0.2353	1.5	4.5	80	1.50	1.0
MS1455	0.2568	2.5	22.0	55	0.52	1.0
MS1512	0.3727	1.4	4.7	48	2.90	1.0
MS1621	0.4275	1.6	6.8	106	2.57	1.0

$M^* + 2$ rather than the original absolute magnitude $M_r = -18.5$ cutoff employed by C97. We also recompute the absolute magnitudes of the CNOC1 clusters to include the same evolution corrections as the RCS clusters (cf., §3.3.5): correcting to redshift $z = 0.338$ using corrections tabulated by Poggianti (2004). Choosing a magnitude limit relative to M^* not only reduces its redshift dependence, but also minimizes the effect of the (small) difference between our R_c magnitudes and the CNOC1 Gunn r. In Table 4.4 we present the re-computed global properties of the CNOC1 clusters, along with their W_{back} values, membership numbers and maximum radii; as for the RCS clusters, we report N_{mem} and R_{max} for only the galaxies brighter than $M^* + 2$ and within $|v| \leq 3\sigma$.

With both the RCS and CNOC1 clusters properly scaled, we can now construct several combined RCS+CNOC1 ensembles of different masses. We choose to create three ensembles, enough to provide some leverage on the mass scale. The three ensembles also have ~ 560 members each, and sufficient radial coverage to construct number density and velocity dispersion profiles out to at least r_{200}. Jeans modelling does not require more than ~ 100 galaxies per ensemble and we could therefore split the data into more ensembles by argument of sheer

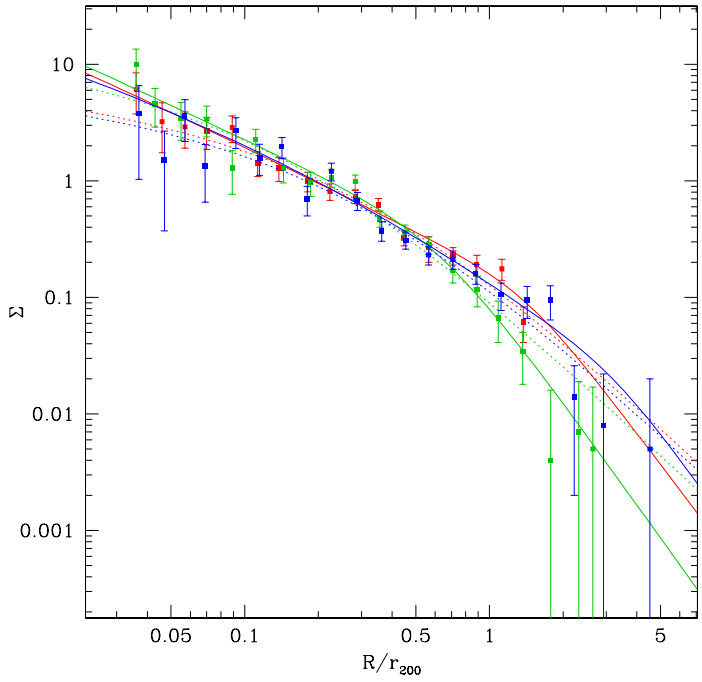

Figure 4.10 Number density profile of ensemble RCS+CNOC1 clusters. Best-fit models are shown as lines (defined as for Figure 4.3). The high-mass ensemble is shown in red, medium-mass in green, and low-mass in blue.

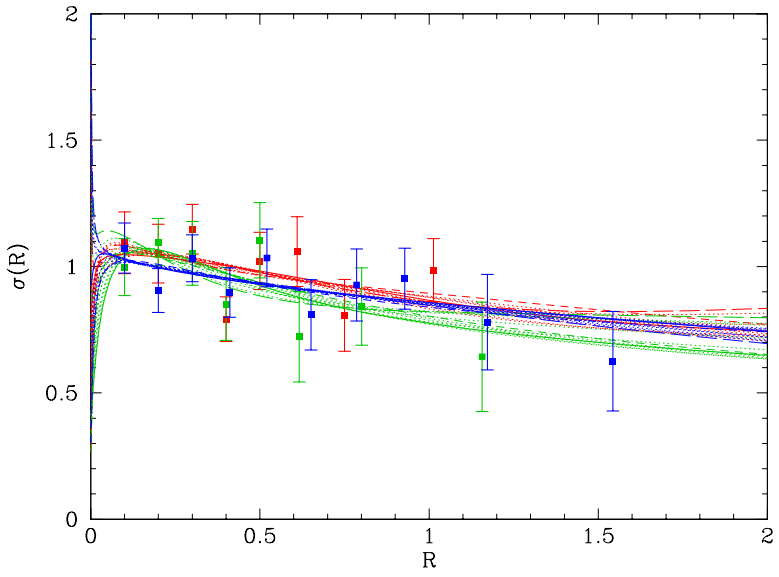

Figure 4.11 Projected velocity dispersion profile of ensemble RCS+CNOC1 clusters. Best-fit models are shown as lines (defined as for Figure 4.3), colours are as defined for Figure 4.10.

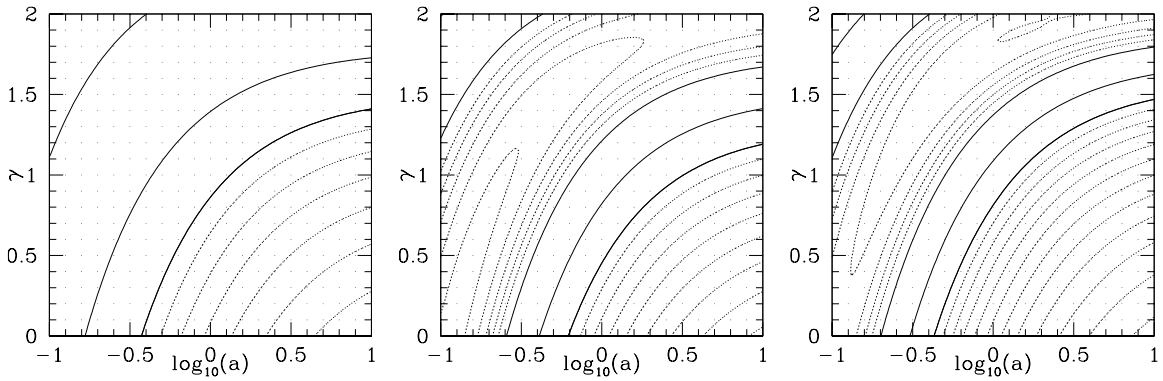

Figure 4.12 Confidence contours of the mass parameters (isotropic), for the RCS+CNOC1 ensembles. The leftmost plot is for the high-mass ensemble, the middle plot is for medium mass, and the rightmost plot is for the low-mass ensemble. Contour levels are defined as for Figure 4.6, all at the same absolute reduced χ^2 values.

numbers alone. However, the highest mass ensemble of three is already limited to $R \leq r_{200}$; creating more ensembles would cause a bias, in that the massive clusters would have small radial extent. Also, if we restrict the number of ensembles, at least 7 clusters make up each ensemble. Thus we retain the primary advantage of our stacking procedure: features of individual clusters such as asphericity and substructure are washed out, making the spherical Jeans modelling more reliable. Median masses of the ensembles are given in Table 4.5. We compute $\Sigma(R)$ and $\sigma(R)$ for these ensembles in the same way as described in §4.3; the resulting profiles are shown in Figures 4.10 and 4.11.

Our Jeans modelling yields similar results to that for the ensemble RCS cluster. Figure 4.12 shows the confidence contours for the isotropic models, using identical reduced χ^2 contour levels for the three ensembles. Roughly the same (γ, a) space is favoured for each of the ensembles. The only significant difference is the wider confidence region (i.e., greater uncertainty) for the highest mass ensemble. This uncertainty is not surprising, since the radial extent of this ensemble is substantially smaller than that of the two lower mass ensembles (as can be readily seen in Figures 4.10 and 4.11).

4.5.1 The Orbital Anisotropy of the RCS+CNOC1 Ensembles

Velocity histograms for the ensembles are shown in Figure 4.13, and the Gauss-Hermite moments h_4 are listed in Table 4.5. The 1σ range in h_4 over all ensembles is roughly equivalent to $0.94 < \sigma_r / \sigma_t < 1.03$. The galaxies in these ensemble clusters are on similar orbits as those of the ensemble RCS cluster: the ensembles all have slightly tangential anisotropies, though at only

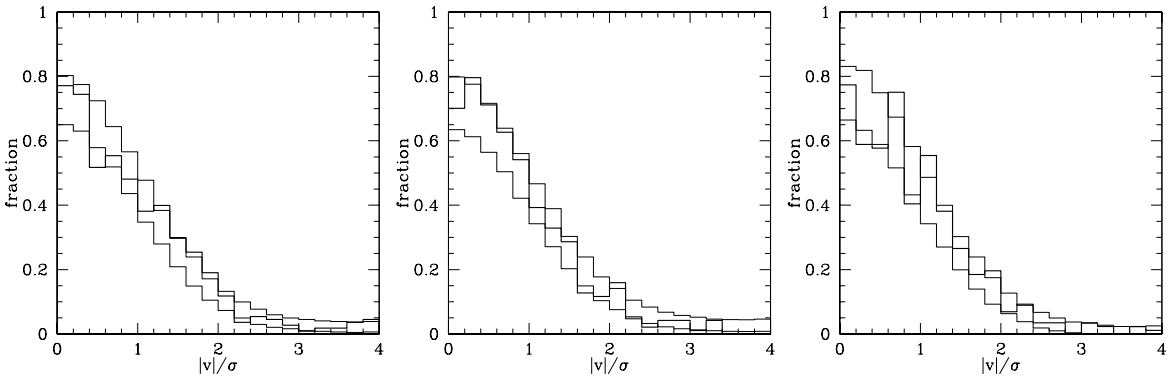

Figure 4.13 Velocity histograms of the RCS+CNOC1 ensembles (thick lines). Monte-Carlo-estimated 1σ uncertainties are shown as thin lines. As for Figure 4.12, the high mass ensemble is at left and ensemble mass decreases from left to right.

the $\sim 1\sigma$ level. As discussed above, the anisotropies we infer are likely somewhat underestimating the true values. So, as we did for the ensemble RCS cluster, we conclude that the true orbits of the galaxies are consistent with zero anisotropy.

4.5.2 Mass-to-Light Ratios of the RCS+CNOC1 Ensembles

We see no significant change in the radial dependence of the mass-to-light ratios for ensemble clusters of different masses. As can be seen in Figure 4.14, the normalized profiles decline slightly with radius, but they are also consistent with a constant M/L (within the 1σ errors). Although there is a small systematic difference between the profiles, it does not form a mass sequence — the intermediate-mass ensemble differs most from a constant M/L. Also, the offset at any radius between the M/L ratios of the three ensembles is much smaller than the uncertainties. Therefore we conclude that there is no significant difference in the M/L profile as a function of cluster mass, and that cluster mass-to-light ratios in general are independent of, or slightly declining with, radius.

4.5.3 Relation between Mass and Concentration

Cosmological simulations predict a dependence of the concentration of the mass density on the total mass of a dark matter halo (NFW; Bullock et al. 2001, hereafter B01). The best-fit concentration parameters (for isotropic NFW models) of our three RCS+CNOC1 ensemble clusters are listed in Table 4.5. We plot the concentrations versus mass, and compare to the B01 prediction in Figure 4.15. Although the B01 simulations did not include dark matter haloes as massive as our clusters, we can extrapolate their relation to compare with our results. We find

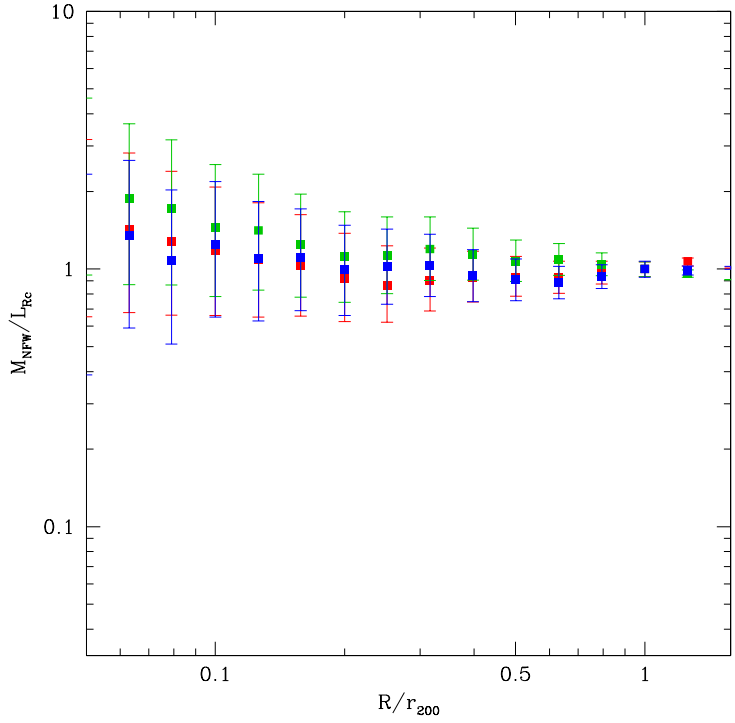

Figure 4.14 Projected M/L profiles for the RCS+CNOC1 ensembles, for the best-fitting NFW models and observed luminosity profiles. As in Figure 4.9, profiles are normalized to the $R = r_{200}$ values.

Table 4.5. Parameters for the high-, medium-, and low-mass RCS+CNOC1 ensembles

	M_{200} $[10^{14} M_\odot]$				Number of	Number of		
Ensemble	min	max	median	$\langle z \rangle$	clusters	members	h_4	concentration[1]
1	15.03	33.12	20.06	0.309	7	596	-0.0066 ± 0.0348	$5.0^{+4.3}_{-2.3}$
2	4.56	15.03	6.72	0.297	14	528	-0.0234 ± 0.0372	$4.1^{+3.5}_{-1.8}$
3	0.21	4.56	2.35	0.363	26	566	-0.0443 ± 0.0368	$4.5^{+3.0}_{-1.7}$

[1]for isotropic NFW model

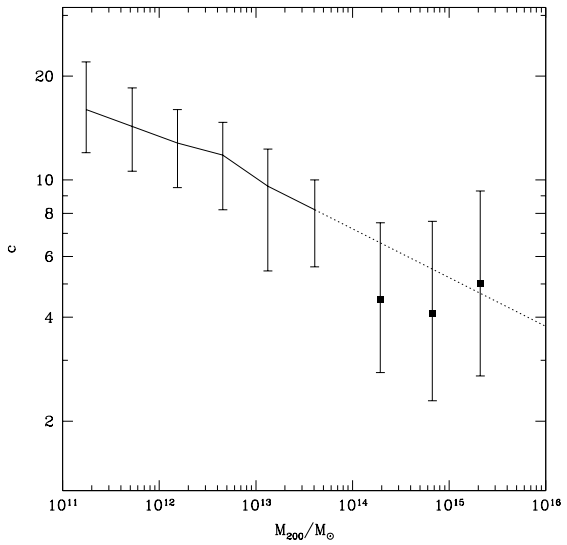

Figure 4.15 Concentration versus mass, for the three ensemble RCS+CNOC1 clusters (solid squares, with 1σ uncertainties). The solid line shows the expectation from simulations (Bullock et al. 2001), with error bars denoting the scatter in the simulated cluster properties. The dotted line is an extrapolation of the B01 result to our mass range.

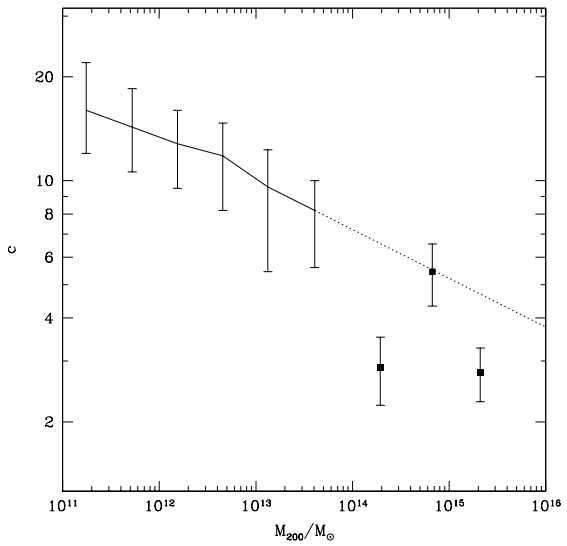

Figure 4.16 Same as Figure 4.15, but for concentrations estimated from the galaxy distribution alone.

Table 4.6. Parameters for the low- and high-redshift RCS+CNOC1 ensembles

Ensemble	redshift min	redshift max	redshift median	$\langle M_{200} \rangle$ $[10^{14} M_\odot]$	Number of clusters	Number of members	h_4	concentration[1]
1	0.282	0.664	0.393	8.9	29	846	-0.0402 ± 0.0272	$1.8^{+1.3}_{-0.8}$
2	0.140	0.282	0.226	11.1	18	844	-0.0021 ± 0.0273	$7.8^{+2.2}_{-3.2}$

[1]for isotropic NFW model

that, though our three ensembles show no trend of concentration with mass within the uncertainties, they do each fall along the extrapolation from B01's simulated haloes. In other words, although the present data alone appear insufficient to constrain the mass-concentration relation, they are certainly consistent with expectation. Similar conclusions were drawn by Łokas et al. (2006) for Abell clusters and by Rines & Diaferio (2006) for clusters in the Sloan Digital Sky Survey. The agreement with Rines & Diaferio (2006) is particularly reassuring, because their mass modelling was performed on individual clusters using the caustic technique (which is nearly independent of orbital shapes); thus their method is complementary to ours.

The concentration parameters calculated by fitting the galaxy distribution to a projected NFW model (Equation 4.4) are somewhat lower than those derived from the dynamical models, and also are more scattered. Figure 4.16 plots these on a mass scale along with the B01 prediction. The galaxy distribution appears to be less concentrated than the mass distribution, and lower than prediction by $\sim 1\sigma$. That is, the concentration parameters inferred from galaxy distributions are biased slightly low. In fact this offset is also expected from simulations: Nagai & Kravtsov (2005) have computed c for dark matter haloes as well as for galaxy-sized subhaloes, and found the same effect.

4.6 Possible Redshift Dependence of Concentration

We have also split the RCS+CNOC1 data into low- and high-redshift ensembles. The parameters of these two ensembles are given in Table 4.6. There is some evidence from the Gauss-Hermite moments that low-redshift clusters have slightly tangential orbits, but the offset from zero anisotropy is still in keeping with the expected measurement bias (Sanchis et al. 2004, LM06). Although the median redshifts of these ensembles are not very different, we do detect some difference between their concentration parameters: higher redshift clusters are less concentrated. Since the ensembles have similar average masses, we can use the B01 prediction for

the evolution of c for a fixed mass: $c \propto 1/(1+z)$. Using this formula and given the c value for the low-redshift ensemble, we predict the concentration for the high-redshift ensemble to be $c = 6.9^{+1.9}_{-2.8}$, which is marginally discrepant ($\sim 1.5\sigma$) with the actual value. However, we do not have much leverage on the redshift axis — only a difference of $\delta z = 0.167$ between the median redshifts of the two ensembles. Also note that the ranges in redshifts within each ensemble are $\delta z = 0.142$ and 0.382 (for the low- and high-mass ensembles respectively): these internal ranges are of order or larger than the redshift difference between the ensembles. In order to better constrain the redshift evolution of the concentration parameter one would require a set of clusters with a larger range in redshift. Nonetheless, it does appear that the concentrations of RCS+CNOC1 ensemble clusters depend somewhat more steeply on redshift than the prediction from simulations. To our knowledge this work represents the first attempt to test this prediction.

4.7 Summary

In this chapter we have performed a dynamical analysis of RCS clusters. In order to boost statistics and diminish asphericity, we stacked the clusters into an ensemble scaled by the velocity dispersions and virial radii determined in chapter 3. We computed a background-corrected projected number density profile and velocity dispersion profile, in a manner similar to C97. We performed Jeans modelling, using the technique of vdM00. Dynamical models using the Jeans equations lead to a degeneracy between mass profile and orbital anisotropy, which can only be lifted by additional information such as the shape of the velocity distribution. We construct the fourth order Gauss-Hermite moment h_4 (which is analogous to kurtosis) and find it to be near zero: in other words, the velocity distribution is consistent with a Gaussian. Thus we conclude that the orbits in RCS clusters are roughly isotropic. In addition to the familiar β–ρ degeneracy, we find that the radial extent of our data are insufficient to separately constrain both the slope and scale radius of the ensemble cluster. However, we do find the mass enclosed within r_{200} to be well-determined, suggesting that global quantities determined in chapter 3 should be independent of the details of the dynamical models. Restricting the parameter range to isotropic models with NFW profiles, we find a scale radius in agreement with the predictions of cosmological simulations by B01. Also, the projected enclosed mass-to-light ratio of the ensemble RCS cluster is nearly independent of radius, in agreement with other observations of both clusters and groups.

We have explored the dependence of the dynamical properties of clusters on mass. In order to do so, we stacked the CNOC1 rich clusters along with our relatively poor RCS clusters into three RCS+CNOC1 ensembles of low, medium, and high mass. All three ensembles have nearly isotropic orbits, and $\sim$constant mass-to-light ratios. The concentration parameters we

derive for isotropic NFW models of these ensembles are in good agreement with the B01 simulation prediction.

We do however, find somewhat different results when we split the RCS+CNOC1 clusters into two ensembles of different redshifts. We find a slightly steeper dependence of concentration on redshift than that expected from the B01 results. This is, as far as we know, the first measurement of the redshift-concentration relation; further work will require more ensemble clusters, and would greatly benefit from more leverage on redshift. In fact, the RCS collaboration is currently observing clusters using the Inamori Magellan Areal Camera and Spectrograph (IMACS), out to $z \simeq 0.85$; these new observations should yield at least two more redshift bins, thus providing useful constraints on the evolution of cluster concentration.

Chapter 5

Conclusions

Clusters of galaxies provide several means of probing theories of cosmology and structure formation. The abundance of clusters as a function of cosmic time can be used to constrain cosmological parameters, such as the mass density of the universe and the dark energy equation of state. In fact, these constraints are roughly orthogonal to those given by other observations such as the luminosities of type Ia supernovae or the fluctuations in the cosmic background radiation, making clusters an extremely valuable tool for the estimation of cosmological parameters.

Detailed studies of galaxy clusters provide useful tests of our scenarios for the formation and evolution of structure in the universe. Cosmological simulations by Navarro et al. (1996, 1997, hereafter NFW) predict a "universal" profile for dark matter haloes, whose scale is set uniquely by halo mass. This prediction can be tested on the scale of galaxy clusters in three ways: the X-ray emitting intracluster gas probes the depth of potential well, the cluster galaxies are dynamical tracers, and gravitational lensing of background objects maps the cluster potential. X-ray observations are confined to the central regions of clusters where the gas density is high, lensing observations are usually restricted to quite massive systems (although *cf.* Parker et al. 2005), while dynamical studies require large numbers of galaxies that have usually not been available for more than a few clusters. Hence, these three classes of observations are complementary; independent constraints on the mass profiles of galaxy clusters using all available techniques are a stringent test of the predictions of cosmological models and simulations.

5.1 The Survey

In this thesis, we undertook a large spectroscopic survey of galaxy clusters in a wide range of masses, drawn from the RCS survey. In chapter 2 we presented the design and observations of the spectroscopic survey. We targeted 36 clusters at moderate redshifts, which were observed

using multi-object spectrographs at the Magellan and CFHT telescopes. Slit masks were designed to maximize the spatial sampling of the cluster regions; for the CFH-MOS observations, we employed a band-limiting filter in order to pack spectra more tightly. We reduced the data and estimated redshifts following the techniques proven by the CNOC1 and CNOC2 surveys. The resulting redshift catalogues contain redshifts for over 3600 galaxies, using existing astrometry and photometry from the RCS survey along with our redshifts, rough spectral classifications, and empirical selection functions. Our spectroscopic survey contains redshifts with an average accuracy of under 100km/s, and samples the luminosity function of clusters well down to $M^* + 2$.

5.2 Results

5.2.1 Global Properties of RCS Clusters

We recovered a total of 33 RCS clusters with sufficient data for our dynamical analysis. Chapter 3 described the global properties of RCS clusters. We computed the cluster locations both in redshift and on the sky, and estimated dynamical properties such as velocity dispersion and mass. We discussed various prescriptions for the removal of interloping field galaxies from the cluster sample, choosing one appropriate to the wide range of cluster richnesses in our sample. We employed four different estimates of cluster centroid, and found the cluster properties to be robust against changes in centroid. The clusters have a wide range of velocity dispersions: $\sigma = 172$–1072km/s, yielding masses from 2.1×10^{13} to $1.6 \times 10^{15} M_{\odot}$. That is, our RCS clusters span the range from groups to rich clusters of galaxies.

Calibrating Clusters for Cosmology

The evolution of the number density of clusters can provide constraints on cosmological parameters, requiring two fundamental properties for each cluster: its redshift and mass. We found that the two-filter photometric redshift estimates provided by the RCS survey are good predictors of spectroscopic redshift, with scatter ~ 0.04 within the redshift range of our clusters ($z \lesssim 0.6$). The optical richness parameter B_{gcR} correlates with cluster mass, although the scatter in the relation is quite large (about 70%). Gladders et al. (2006) have used self-calibration to determine Ω_M and σ_8 from the RCS cluster catalogue; along with the cosmological parameters they performed an unconstrained fit to the mass-richness calibration. Their derived calibration is in good agreement with our relation. In addition, they derive a scatter on the calibration which is completely consistent with what we obtained. (Gladders et al. 2006) have also shown that constraints on cosmology can be greatly improved by including priors on the cluster mass calibration and its scatter. Our result therefore provides a useful

step towards the estimation of cosmological parameters such as the dark energy equation of state.

The Mass-to-Light Ratios of Clusters

We also measured the relation between cluster mass and R_c-band luminosity, which agrees well with results of other authors over a wide range in mass ($\sim 10^{12}$–$10^{15} M_\odot$). Although the scatter is large, the agreement is remarkable since the sample types and sample redshifts are various: groups and clusters found in redshift surveys such as CNOC2, 2dF, and SDSS; X-ray selected CNOC1 clusters; and our RCS clusters found in angular and colour space. Models for the dependence of M/L on mass using the halo occupation distribution formalism (Tinker et al. 2005) agree with the results in a broad sense, but are unable to match the slope of the combined observations. The models reach a plateau value beyond $M \sim 10^{14} M_\odot$; the height of the plateau is set by a choice of σ_8. In contrast, the observations show no obvious plateau at all out to $M > 10^{15}$. The Tinker et al. (2005) models do not match the data at low masses either, since the slopes are too shallow at low M to extend down to the M/L ratios observed for galaxy groups. These discrepancies are equivalent to incorrect estimates of the efficiency of integrated star-formation in groups and clusters , as a function of mass. Of course, tighter observational constraints would also be very helpful in this case — there remains a spread of about an order of magnitude in mass-to-light ratio.

5.2.2 The Distribution of Mass in Clusters

In chapter 4, we proceeded to a more detailed analysis of the structure of galaxy clusters. We stacked the RCS clusters into an ensemble, and constructed the projected velocity dispersion and number density profiles of the ensemble. We reconstructed the mass profile of the ensemble using the Jeans equation, and performed several tests on the robustness of the result to perturbations in the input data. We found a well-known degeneracy between the mass density and the anisotropy of the galaxy orbits, which we lifted using further information from the shape of the velocity distribution. We also found that although the shape of the mass profile is strongly dependent on anisotropy, the mass enclosed within the virial radius is stable. This result, also noted by vdM00 for CNOC1 clusters, indicates that the virial masses and M/L ratios we computed for the "parent" clusters of this ensemble do not depend strongly on the shapes of the galaxy orbits.

The Average Mass Profile of RCS Clusters

We found the velocity distribution of the ensemble RCS cluster to have Gauss-Hermite moment $h_4 = -0.025 \pm 0.028$. This value is consistent with a Gaussian, which suggests that the

orbits of galaxies in RCS clusters are on average isotropic. In fact we estimated the range in anisotropy of the ensemble cluster to be only $0.96 < \sigma_r/\sigma_t < 1.004$.

Because our spectroscopic survey is has very sparse spatial sampling for radii below about $0.1r_{200}$ and only has sufficient radial coverage to measure velocity dispersions for projected radii out to $\sim r_{200}$, we are unable to constrain the inner core slope of the cluster mass profile or test for convergence to the $\rho \propto r^{-3}$ behaviour expected for the NFW profile at large radii. In any case, a simple Jeans analysis such as we have presented here is unlikely to be fruitful in these regions: in the cluster cores it is important to consider the separate contributions of baryonic and dark matter, while the equilibrium conditions necessary for application of the Jeans equation are likely to be invalid at large radii, where field and group galaxies are falling in to the cluster for the first time. However, the RCS clusters are certainly consistent with the NFW density profile within the radial range probed by our data. The best-fitting concentration parameter for this ensemble (using NFW models with isotropic orbits) was found to be $3.4^{+2.5}_{-1.4}$, as expected from cosmological simulations.

The Radial Dependence of the cluster Mass-to-Light Ratio

The radial profile of the cluster mass-to-light ratio is important, because it connects the dense cores of clusters with the surrounding infall region and ultimately the field, as well as connecting the cluster galaxies with the cluster dark matter haloes. In common with results for CNOC1, 2dF, and Abell clusters, we found a slightly decreasing mass-to-light ratio (although it is also consistent with M/L independent of radius). In other words, light appears to trace mass fairly well in clusters, at least within the virial region; but there is some indication of a decline in the mass-to-light ratio as the radius increases (and this should ultimately drop to meet the field value of M/L at very large radii). This result does not appear to depend on the mass of the ensemble.

Testing for Universality: The Relation between Concentration and Mass

We constructed three ensemble clusters of combined RCS and CNOC1 data, of different masses. Using Gauss-Hermite moments, we found them all to have velocity distributions consistent with isotropic orbits. Unfortunately, as found for the single RCS ensemble, the spatial sampling at small radii is poor, and we were unable to constrain the inner core slope of the density. Restricting ourselves to isotropic models with NFW mass density profiles, we compared the resulting concentration parameters with predictions. Cosmological simulations by Bullock et al. (2001) predict a declining trend of concentration as a function of mass. We found no trend among our three mass bins, but all three measurements agree very well with the simulation prediction. Our result is in agreement with other work using 6 low-redshift Abell clusters

(Łokas et al. 2006), and with 72 low-redshift SDSS clusters (Rines & Diaferio 2006).

We noted that the concentrations one would predict using only galaxy number densities are similar to the dynamically derived results, but are somewhat lower. This systematic effect is also predicted by simulations (Nagai & Kravtsov 2005), and suggests that estimating concentration parameters from the galaxy distribution alone will lead to a bias toward lower concentration.

The Relation between Concentration and Redshift

We have attempted to measure the dependence of the concentration parameter on redshift, using two ensembles of different redshifts. We did find some apparent evolution: the concentration drops by about a factor of four (though with substantial uncertainty). This evolution is stronger than the simulation prediction, but only at a significance of $\sim 1.5\sigma$. To our knowledge, this is the first measurement of evolution of the density concentration parameter of clusters. The redshift difference between the medians of the two ensembles is only $\delta z = 0.167$, and is comparable to the redshift range internal to each ensemble. It would be interesting to apply a similar analysis to more ensemble clusters, preferably with more leverage on redshift, to confirm this trend.

5.3 Future Work

Several avenues of further research naturally arise from this thesis. First, it would be of interest to combine our dynamical analysis with galaxy populations. A previous study by Biviano & Katgert (2004) indicates the existence of some "orbital segregation" in rich clusters. They performed an inverted Jeans analysis on Abell clusters, using the best-fit mass profile for elliptical galaxies, to derive the anisotropy profiles for galaxies of different types. They found that elliptical galaxies and early-type spirals follow isotropic orbits, a result consistent with formation in the cluster or entry into the cluster at early times so that these galaxies are on relaxed orbits. Late-type spirals, on the other hand, were found to have radially orbits (with anisotropy increasing with radius), suggesting that they have only recently entered the cluster potential and still retain a memory of infall.

It would be interesting to apply a similar analysis to the RCS ensemble clusters, to see if this segregation also holds for less massive systems. In the present work we have composed ensembles of RCS and CNOC1 clusters using all galaxy types, because of the approximate nature of the spectral types we determined from redshift estimates (see §2.4.2). More precise information about the galaxy spectral (or morphological) types in our surveyed clusters can be obtained, e.g., using principal component analysis (Ellingson et al. 2001). With more precise galaxy types, and a mass profile in hand, Biviano & Katgert (2004) have shown it can be use-

ful to invert the Jeans analysis to obtain the velocity anisotropy profile of various dynamical tracers. This procedure applied to the RCS clusters might reveal if orbital segregation found in nearby Abell clusters is also present in poorer clusters.

Also, note that the present study does not provide any information on possible radial variation of the anisotropy of the galaxy orbits. Simulations of dark matter haloes do predict a mild positive dependence of σ_r/σ_t on radius (e.g., Wojtak et al. 2005; Hansen & Moore 2006). In fact, Hansen & Moore (2006) suggest there may be a universal relation between local density slope and anisotropy, found to hold for cosmological simulations as well as model dark matter collisions. Although it is possible to simply add complexity to our current modelling technique by allowing radial variation of σ_r/σ_t, we feel that given the substantially different σ_r/σ_t behaviour found by Biviano & Katgert (2004) for different galaxy types, it is more appropriate to examine any radial variation of anisotropy in concert with an examination of variation with galaxy type.

The calibration between richness and mass is a very important ingredient of the measurement of cluster abundance and through it the estimation of cosmological parameters. Gladders et al. (2006) have shown that this measurement can be made using the RCS survey data alone, but that cosmological constraints are greatly improved by empirical information on the richness-mass relation as well as its scatter and evolution. We have estimated this relation in the present work, along with its scatter; unfortunately we do not have enough clusters, nor do we have clusters in a wide enough redshift range, to constrain its evolution or the uncertainty of the scatter. A new survey of spectroscopic observations of RCS clusters is currently underway, using the IMACS multi-object spectrograph along with band-limiting filters, in order to address this issue by allowing dynamical analysis of ~ 36 more clusters out to redshift $z = 0.85$. Improved measurements of the richness-mass calibration, combined with the ~ 10000 clusters expected from the ongoing RCS2 survey, should measure the evolution of the cluster abundance to sufficient accuracy to constrain the equation of state of the dark energy.

IMACS observations may also help to test the NFW prediction of a $\rho \propto r^{-3}$ density profile for the outer regions of clusters. The present work does not extend much beyond the virial regions of most of the RCS clusters observed, which prevents us from constraining the outer slope of the mass density. In contrast, the large field of view of IMACS (nearly $30'$) probes well beyond the virial radius, to the infall regions of the clusters. Although the Jeans equation does not apply outside of the virialized region of clusters, the caustic method (Diaferio & Geller 1997; Diaferio 1999) does not require assumptions of equilibrium and can be used to measure mass profiles in the outskirts of clusters. Thus the IMACS observations currently underway by the RCS collaboration will both aid in accurately measuring the richness-mass calibration and testing the prediction of a universal density profile for galaxy clusters.

We have entered an exciting time in the study of galaxy clusters, triggered by break-

throughs in computation and in instrumentation. Massive increases in computing power have brought us great insight into the formation and evolution of cosmological structures such as the massive dark matter haloes which host galaxy clusters. Although much work remains to be done in converting dark-matter sub-haloes to realistic galaxies in these simulations, the basic picture of structure formation has already been outlined. Also, instrumentation technology has leapt forward. Large-format CCDs have made surveys such as RCS1 and RCS2 possible, bringing us much larger samples of galaxy clusters than ever available before. Of course, with these large surveys come a substantial burden of follow-up efforts. New wide-field multi-object spectrographs such as IMACS can probe the outskirts of clusters, where field and group galaxies are falling into clusters for the first time. New infrared instruments such as the Spitzer Space Telescope probe the galaxy stellar masses in the near-infrared and reveal dust-enshrouded star formation in the far-infrared. Sensitive and high-resolution X-ray observatories and upcoming studies of the Sunyaev-Zeldovich effect provide a wealth of information on the physics of hot intracluster gas. The coming years will be very interesting, as all the pieces of evidence from both theoretical and observational fronts are knit together into a more complete understanding of clusters of galaxies.

References

Abraham, R. G., Yee, H. K. C., Ellingson, E., Carlberg, R. G., & Gravel, P. 1998, ApJS, 116, 231

Akritas, M. G. & Bershady, M. A. 1996, ApJ, 470, 706

Allington-Smith, J., Breare, M., Ellis, R., Gellatly, D., Glazebrook, K., Jorden, P., Maclean, J., Oates, P., Shaw, G., Tanvir, N., Taylor, K., Taylor, P., Webster, J., & Worswick, S. 1994, PASP, 106, 983

Bahcall, N. A., Cen, R., Davé, R., Ostriker, J. P., & Yu, Q. 2000, ApJ, 541, 1

Bahcall, N. A. & Comerford, J. M. 2002, ApJ, 565, L5

Barnes, J. 1983, MNRAS, 203, 223

Beers, T. C., Flynn, K., & Gebhardt, K. 1990, AJ, 100, 32

Bennett, C. L., Halpern, M., Hinshaw, G., Jarosik, N., Kogut, A., Limon, M., Meyer, S. S., Page, L., Spergel, D. N., Tucker, G. S., Wollack, E., Wright, E. L., Barnes, C., Greason, M. R., Hill, R. S., Komatsu, E., Nolta, M. R., Odegard, N., Peiris, H. V., Verde, L., & Weiland, J. L. 2003, ApJS, 148, 1

Binney, J. & Tremaine, S. 1987, Galactic dynamics (Princeton, NJ, Princeton University Press, 1987, 747 p.)

Biviano, A. & Girardi, M. 2003, ApJ, 585, 205

Biviano, A. & Katgert, P. 2004, A&A, 424, 779

Biviano, A., Murante, G., Borgani, S., Diaferio, A., Dolag, K., & Girardi, M. 2006, ArXiv Astrophysics e-prints

Bruzual, G. & Charlot, S. 2003, MNRAS, 344, 1000

Bullock, J. S., Kolatt, T. S., Sigad, Y., Somerville, R. S., Kravtsov, A. V., Klypin, A. A., Primack, J. R., & Dekel, A. 2001, MNRAS, 321, 559

Carlberg, R. G., Yee, H. K. C., & Ellingson, E. 1997, ApJ, 478, 462

Carlberg, R. G., Yee, H. K. C., Ellingson, E., Abraham, R., Gravel, P., Morris, S., & Pritchet, C. J. 1996, ApJ, 462, 32

Carlberg, R. G., Yee, H. K. C., Morris, S. L., Lin, H., Hall, P. B., Patton, D. R., Sawicki, M., & Shepherd, C. W. 2001, ApJ, 552, 427

Coleman, G. D., Wu, C.-C., & Weedman, D. W. 1980, ApJS, 43, 393

Danese, L., de Zotti, G., & di Tullio, G. 1980, A&A, 82, 322

Diaferio, A. 1999, MNRAS, 309, 610

Diaferio, A. & Geller, M. J. 1997, ApJ, 481, 633

Diaferio, A., Ramella, M., Geller, M. J., & Ferrari, A. 1993, AJ, 105, 2035

Díaz, E. & Muriel, H. 2005, MNRAS, 364, 1299

Diemand, J., Zemp, M., Moore, B., Stadel, J., & Carollo, M. 2005, MNRAS, 364, 665

Eke, V. R., Baugh, C. M., Cole, S., Frenk, C. S., King, H. M., & Peacock, J. A. 2005, MNRAS, 362, 1233

Eke, V. R., Frenk, C. S., Baugh, C. M., Cole, S., Norberg, P., Peacock, J. A., Baldry, I. K., Bland-Hawthorn, J., Bridges, T., Cannon, R., Colless, M., Collins, C., Couch, W., Dalton, G., de Propris, R., Driver, S. P., Efstathiou, G., Ellis, R. S., Glazebrook, K., Jackson, C. A., Lahav, O., Lewis, I., Lumsden, S., Maddox, S. J., Madgwick, D., Peterson, B. A., Sutherland, W., & Taylor, K. 2004, MNRAS, 355, 769

Ellingson, E., Lin, H., Yee, H. K. C., & Carlberg, R. G. 2001, ApJ, 547, 609

Ellingson, E., Yee, H. K. C., Abraham, R. G., Morris, S. L., & Carlberg, R. G. 1998, ApJS, 116, 247

Ellingson, E., Yee, H. K. C., Abraham, R. G., Morris, S. L., Carlberg, R. G., & Smecker-Hane, T. A. 1997, ApJS, 113, 1

Fadda, D., Girardi, M., Giuricin, G., Mardirossian, F., & Mezzetti, M. 1996, ApJ, 473, 670

Fukugita, M., Shimasaku, K., & Ichikawa, T. 1995, PASP, 107, 945

Gerke, B. F., Newman, J. A., Davis, M., Marinoni, C., Yan, R., Coil, A. L., Conroy, C., Cooper, M. C., Faber, S. M., Finkbeiner, D. P., Guhathakurta, P., Kaiser, N., Koo, D. C., Phillips, A. C., Weiner, B. J., & Willmer, C. N. A. 2005, ApJ, 625, 6

Girardi, M., Biviano, A., Giuricin, G., Mardirossian, F., & Mezzetti, M. 1993, ApJ, 404, 38

Girardi, M., Fadda, D., Giuricin, G., Mardirossian, F., Mezzetti, M., & Biviano, A. 1996, ApJ, 457, 61

Gladders, M. D. 2002, Ph.D. Thesis

Gladders, M. D. & Yee, H. K. C. 2000, AJ, 120, 2148

—. 2005, ApJS, 157, 1

Gladders, M. D., Yee, H. K. C., Majumdar, S., Barrientos, L. F., Hoekstra, H., Hall, P. B., & Infante, L. 2006, ApJ, submitted

Hansen, S. H. & Moore, B. 2006, New Astronomy, 11, 333

Hsieh, B. C., Yee, H. K. C., Lin, H., & Gladders, M. D. 2005, ApJS, 158, 161

Hubble, E. & Humason, M. L. 1931, ApJ, 74, 43

Katgert, P., Biviano, A., & Mazure, A. 2004, ApJ, 600, 657

Kennicutt, R. C. 1992, ApJS, 79, 255

Kent, S. M. & Gunn, J. E. 1982, AJ, 87, 945

Le Fevre, O., Crampton, D., Felenbok, P., & Monnet, G. 1994, A&A, 282, 325

Lin, H., Yee, H. K. C., Carlberg, R. G., Morris, S. L., Sawicki, M., Patton, D. R., Wirth, G., & Shepherd, C. W. 1999, ApJ, 518, 533

Łokas, E. L. & Mamon, G. A. 2001, MNRAS, 321, 155

—. 2003, MNRAS, 343, 401

Łokas, E. L., Wojtak, R., Gottlöber, S., Mamon, G. A., & Prada, F. 2006, MNRAS, 367, 1463

Lu, Y., Mo, H. J., Katz, N., & Weinberg, M. D. 2006, MNRAS, 401

Mahdavi, A. & Geller, M. J. 2004, ApJ, 607, 202

Mahdavi, A., Geller, M. J., Böhringer, H., Kurtz, M. J., & Ramella, M. 1999, ApJ, 518, 69

Majumdar, S. & Mohr, J. J. 2004, ApJ, 613, 41

Marinoni, C. & Hudson, M. J. 2002, ApJ, 569, 101

Merritt, D. & Saha, P. 1993, ApJ, 409, 75

Nagai, D. & Kravtsov, A. V. 2005, ApJ, 618, 557

Navarro, J. F., Frenk, C. S., & White, S. D. M. 1996, ApJ, 462, 563

—. 1997, ApJ, 490, 493

Parker, L. C., Hudson, M. J., Carlberg, R. G., & Hoekstra, H. 2005, ApJ, 634, 806

Poggianti, B. 2004, in Baryons in Dark Matter Halos, 35–+

Rines, K. & Diaferio, A. 2006, ArXiv Astrophysics e-prints

Rines, K., Geller, M. J., Diaferio, A., Kurtz, M. J., & Jarrett, T. H. 2004, AJ, 128, 1078

Rines, K., Geller, M. J., Kurtz, M. J., & Diaferio, A. 2003, AJ, 126, 2152

Rood, H. J. & Dickel, J. R. 1979, ApJ, 233, 418

Sanchis, T., Łokas, E. L., & Mamon, G. A. 2004, MNRAS, 347, 1198

Sand, D. J., Treu, T., Ellis, R. S., & Smith, G. P. 2005, ApJ, 627, 32

Smith, S. 1936, ApJ, 83, 23

Tinker, J. L., Weinberg, D. H., Zheng, Z., & Zehavi, I. 2005, ApJ, 631, 41

Tonry, J. & Davis, M. 1979, AJ, 84, 1511

van der Marel, R. P. & Franx, M. 1993, ApJ, 407, 525

van der Marel, R. P., Magorrian, J., Carlberg, R. G., Yee, H. K. C., & Ellingson, E. 2000, AJ, 119, 2038

White, S. D. M. & Frenk, C. S. 1991, ApJ, 379, 52

Wojtak, R., Łokas, E. L., Gottlöber, S., & Mamon, G. A. 2005, MNRAS, 361, L1

Yee, H. K. C. & Ellingson, E. 2003, ApJ, 585, 215

Yee, H. K. C., Ellingson, E., Abraham, R. G., Gravel, P., Carlberg, R. G., Smecker-Hane, T. A., Schade, D., & Rigler, M. 1996a, ApJS, 102, 289

Yee, H. K. C., Ellingson, E., & Carlberg, R. G. 1996b, ApJS, 102, 269

Yee, H. K. C., Ellingson, E., Morris, S. L., Abraham, R. G., & Carlberg, R. G. 1998, ApJS, 116, 211

Yee, H. K. C. & López-Cruz, O. 1999, AJ, 117, 1985

Yee, H. K. C., Morris, S. L., Lin, H., Carlberg, R. G., Hall, P. B., Sawicki, M., Patton, D. R., Wirth, G. D., Ellingson, E., & Shepherd, C. W. 2000, ApJS, 129, 475

Zabludoff, A. I., Huchra, J. P., & Geller, M. J. 1990, ApJS, 74, 1

Zwicky, F. 1933, Helvetica Physica Acta, 6, 110

—. 1937, ApJ, 86, 217